**This document is downloaded from DR-NTU (https://dr.ntu.edu.sg)
Nanyang Technological University, Singapore.**

# A semi-empirical modelling of selective laser melting

Yap, Chor Yen

2016

Yap, C. Y. (2016). A semi-empirical modelling of selective laser melting. Doctoral thesis, Nanyang Technological University, Singapore.

http://hdl.handle.net/10356/69292

https://doi.org/10.32657/10356/69292

*Downloaded on 09 Apr 2024 16:47:53 SGT*

NANYANG
TECHNOLOGICAL
UNIVERSITY

# A SEMI-EMPIRICAL MODELLING OF SELECTIVE LASER MELTING

**YAP CHOR YEN**

**INTERDISCIPLINARY GRADUATE SCHOOL**
**ENERGY RESEARCH INSTITUTE @ NTU (ERI@N)**

**2016**

# A SEMI-EMPIRICAL MODELLING OF SELECTIVE LASER MELTING

YAP CHOR YEN

Interdisciplinary Graduate School
Energy Research Institute @ NTU (ERI@N)

A thesis submitted to the Nanyang Technological University in
partial fulfilment of the requirement for the degree of
Doctor of Philosophy

**2016**

# Statement of Originality

I hereby certify that the work embodied in this thesis is the result of original research and has not been submitted for a higher degree to any other University or Institution.

29 July 2016
. . . . . . . . . . . . . . . . .
Date

. . . . . . . . . . . . . . . . . . . . . . . . . . . .
Yap Chor Yen

# Abstract

Selective Laser Melting is a particular powder bed based Additive Manufacturing technology capable of producing metallic components from powders. There has been increasing research and industrial interests in this technology as it can achieve near-full density fabrication. Research has also shown that Selective Laser Melting is capable of producing components that are higher in strength and hardness compared to their cast counter parts due to the localised and rapid solidification that occurs during the process. As interests in Selective Laser Melting grows, more research has been focused on finding the optimal process parameters for different materials. However, current parameter optimization studies are usually carried out by trial-and-error, which is time consuming.

This Ph.D. project aims to develop a semi-empirical model of the Selective Laser Melting process. This model will enable parameter optimization studies to be shortened by a providing a close estimation of the energy requirement of the process, by considering the thermal properties of the materials, the laser-material interaction and morphology of the melt tracks. The scope of this project is limited to metals and alloys as they are the most common materials used in industrial applications and some of the relevant information is available in scientific articles.

A model of the process was developed and the energy requirement of the process was found to vary with the thermal conductivity values of the materials, in addition to their thermal capacities and melting temperatures. Applications and limitations of this semi-empirical model are also discussed. Through this work, optimized process parameters were also established for pure nickel and pure tin. These metals had not been successfully processed by Selective Laser Melting previously. The resultant microstructures of these materials have also been examined via various characterization techniques.

## Acknowledgements

I would like to express my sincere gratitude to my supervisor Professor Chua Chee Kai, for the continuous support of my Ph.D. study and related research, for his patience, motivation, and generosity. His guidance helped me in all the time of research and writing of this thesis.

I would also like to thank my co-supervisor Associate Professor Dong Zhili for his support and guidance in my study and research. He is always ready to provide valuable council and provide additional support on the project.

Besides my advisors, I would like to thank the rest of my thesis committee: Assistant Professor Moon Seung Ki, and Dr. May Win Naing, for their insightful comments and encouragement, which helped to refine my research from various perspectives.

I thank my fellow labmates for the discussions that provided different perspectives, for working together in the face of deadlines, and for all the fun we have had in the last four years. Also, I thank my friends in the Singapore Centre for 3D Printing. In particular, I am grateful to Dr. Liu Zhonghong and Dr. Zhang Danqing for enlightening me the first glance of research.

In addition, I would like to extend my gratitude to the staff of the School of Mechanical and Aerospace Engineering, namely Mr. Chia Yak Khoon, Mr. Soh Beng Choon, Mr. Wong Cher Kong, Mr. Wee Tiew Teck, Ms. Tan How Jee, and Mr. Koh Wing Leong for their technical support, making my research experience a smooth and enjoyable one.

Last but not the least, I would like to thank my parents for their love and support throughout the writing of this thesis and in my life.

# Table of Contents

**Abstract** ........................................................................................................ i

**Acknowledgements** ...................................................................................... iii

**Table of Contents** ........................................................................................... v

**Table Captions** ............................................................................................. ix

**Figure Captions** ............................................................................................ xi

**Abbreviations** .............................................................................................. xv

**Chapter 1 Introduction** …........................................................................ 1

1.1 Problem Statement …………………………………………………..... 3

1.2 Objective and Scope ………………………………………………….. 5

1.3 Dissertation Overview ……………………………………………….... 5

1.4 Resulting Outcomes ………………………………………………….. 6

References …………………………………………………………………… 7

**Chapter 2 Literature Review** ……………………………………….... 9

2.1 Overview of the Selective Laser Melting Process …………………... 11

2.1.1 Physical Phenomena and Process Parameters of SLM ……………… 13

2.1.2 SLM of Metals and Alloys …………………………………………... 21

2.1.3 Modelling of the SLM Process ……………………………………... 28

2.2 Ph.D. in Context of Literature ……………………………………… 31

References ………………………………………………………………….... 32

**Chapter 3 Experimental Methodology and Modelling ………………. 43**
3.1 Rationale for Selection of Methods ……………………….……... 45
3.2 Data Collection …………………………………………...…… 45
3.2.1 Data Collection via Literature ……………..…………………….. 46
3.2.2 Experimental Data Collection …..…………………………….... 47
3.3 Modelling ……………………………………………………….... 47
3.3.1 Development of Model ………………………………………….... 48
3.3.2 Assumptions in the Semi-Empirical Model ……………………….... 50
3.4 Synthesis …………………………………………………………. 54
3.4.1 Parameter Optimization – Principles ……………………………….. 55
3.4.2 Density Measurements – Principles ………………………………… 56
3.5 Characterization ……………………………………………………….. 57
3.5.1 X-Ray Diffraction – Principles ……………………………………… 57
3.5.2 Light Optical Microscopy – Principles ……………………………… 58
3.5.3 Scanning Electron Microscopy – Principles ………………………… 59
3.6 Overview of Methodologies ………………………………………… 60
References ……………………………………………………………….. 62

**Chapter 4 Selective Laser Melting of AlSi10Mg ……………….……. 63**
4.1 Introduction …………………………………………………………. 65
4.2 Experimental Methods ……………………………………………… 66
4.2.1 Synthesis ……………………………………………………………. 67
4.2.2 X-Ray Diffraction ……………………………………………….... 67
4.2.3 Light Optical Microscopy ………………………………………….... 68
4.2.4 Scanning Electron Microscopy …………………………………….... 70
4.2.5 Energy-Dispersive X-ray Spectroscopy …………………………….. 71
4.3 Principal Outcomes …………………………………………………. 73
References ……………………………………………………………….... 77

**Chapter 5 Selective Laser Melting of Nickel ……………………….……… 79**
5.1 Introduction ……………………………………………………… 81
5.2 Experimental Methods ………………………………………… 82
5.2.1 Synthesis ……………………………………………………… 82
5.2.2 X-Ray Diffraction ……………………………………………... 83
5.2.3 Light Optical Microscopy ……………………………………... 84
5.2.4 Scanning Electron Microscopy ………………………………... 87
5.2.5 Electron Backscatter Diffraction ……...…………………………….. 89
5.3 Principal Outcomes ……………………………………………… 91
References ………………………………………………………………... 93

**Chapter 6 Selective Laser Melting of Tin ……….…………...……… 95**
6.1 Introduction ……………………………………………………… 97
6.2 Experimental Methods ………………………………………… 98
6.2.1 Synthesis ……………………………………………………… 98
6.2.2 X-Ray Diffraction ……………………………………………... 99
6.2.3 Light Optical Microscopy …………………………………… 100
6.2.4 Scanning Electron Microscopy …………………………......... 104
6.2.5 Electron Backscatter Diffraction ……...…………………………… 104
6.3 Principal Outcomes ……………………………………………... 106
References …………………………………………………………… 108

**Chapter 7 Discussion ……………………….……….……...……… 109**
7.1 General Discussion ……………………………………………... 110
7.1.1 Compensation Factor β and Thermal Conductivity ……………….. 111
7.1.2 Applications ………………………………………………….. 113
7.1.3 Limitations of the Model ……………………………………... 113
7.2 Reconnaissance work not included in main chapters ……………… 114
References …………………………………………………………… 119

**Chapter 8 Conclusion and Future Work** ..……….………..….…….. **121**

8.1 Findings and Conclusion …………………………………………... 122

8.2 Recommendations for Future Work ……………………………….. 123

References ………………………………………………………………. 125

**Appendix A List of Publications** …………...……….………..….…….. **127**

# Table Captions

**Table 2.1** Types of metals and alloys researched for the SLM process.

**Table 2.2** List of materials studied for SLM and the highest relative densities reported.

**Table 3.1** Selected SLM process parameters published in scientific literature.

**Table 3.2** Results from process optimization studies carried out in SC3DP.

**Table 3.3** Description of parameters and the corresponding units in Equation (4).

**Table 4.1** Elemental composition comparison of aluminium alloys: AlSi10Mg and 360.0.

**Table 4.2** Most energy efficient SLM process parameters for achieving relative densities higher than 98 %, as measured by volumetric energy density (VED).

**Table 4.3** EDX analysis on α and β regions of SLM AlSi10Mg.

**Table 7.1** SLM process parameters with the lowest energy density required to achieve 98% relative density for AlSi10Mg, nickel, and tin.

**Table 7.2** Relative densities of SLM of copper powder, CU1332.

# Figure Captions

**Figure 1.1** Complex geometries and minute structures by SLM.

**Figure 2.1** Processing of STL file with Magics, orientation with a 45° rotation from (a) to (b) and generation of support structures (c).

**Figure 2.2** Layer-by-layer manufacturing of the SLM process. i) The high-power laser melts selective areas of the powder bed. ii) The process is repeated for successive layers. iii) Loose powder is removed and finished part is revealed.

**Figure 2.3** Primary dissipation of the multiphase energy dissipation, showing internal reflections of the laser irradiation in the powder bed.

**Figure 2.1** Severe balling over several layers in SLM.

**Figure 2.5** Temperature Gradient Mechanism (top) leading to crack formation and delamination of manufactured parts.

**Figure 2.6** Illustration of common SLM parameters: laser power, scanning speed, hatch spacing and layer thickness.

**Figure 2.7** Illustration of numerical analysis of the SLM process in 2D (a) and a screenshot of 3D simulation (b). The temperature profile gives the boundary of the melt pool and shows the possibility of vaporization.

**Figure 2.8** Simulation of SLM by factoring in the powder bed nature of the process.

**Figure 3.1** Simplification of melt tracks as overlapping semi-circular stripes (left) and melt profile of SLM M2 steel on XZ plane through light microscopy and electron backscatter diffraction (right).

**Figure 3.2** Illustration of hatch spacing and layer thickness. Melt pools are modelled to have semi-circular cross sections with radius (r) and overlapping height ($\tau$) between two neighbouring melt tracks.

**Figure 3.3** Plot of compensation factor against thermal conductivity of the respective material. The data is compiled via literature survey and experiments conducted in other research projects in SC3DP.

**Figure 3.4** Illustration of the relationship between variables in Bragg's law: $n\lambda=2d \sin \theta$.

**Figure 4.1** XRD analysis of SLM AlSi10Mg showing peaks that match those of Al9Si and Al$_{3.2}$1Si$_{0.47}$.

**Figure 4.2** Optical microscopy of SLM AlSi10Mg samples in the x-y plane (a) and x-z plane (b).

**Figure 4.3** SEM micrograph of SLM AlSi10Mg sample in the x-y plane at different magnifications, after etching with Flick's reagent.

**Figure 4.4** Relative densities of SLM AlSi10Mg samples obtained at various scanning speeds, from 500 mm/s to 3,500 mm/s.

**Figure 4.5** Relative densities of SLM AlSi10Mg samples (mean, minimum and maximum) obtained at different hatch spacings, from 0.07 mm to 0.2 mm.

**Figure 4.6** Variation of the relative density (mean, minimum and maximum) of SLM AlSi10Mg samples against input volumetric energy density, $\frac{P}{vht}$.

**Figure 5.1** Spherical nickel powders used in the investigation with SLM.

**Figure 5.2** X-ray Diffraction analysis of nickel powder and SLM processed nickel sample.

**Figure 5.3** Optical microscopy images of SLM processed nickel at a lower magnification, showing XY planes (a) and XZ planes (b).

**Figure 5.4** LOM images of SLM nickel at a higher magnification. These areas observed corresponds to the areas indicated by the red boxes in Figure 5.3.

**Figure 5.5** Scanning electron microscopy of SLM nickel samples in the (a) XY plane and (b) XZ plane.

**Figure 5.6** EBSD analysis of SLM processed nickel, displaying the different crystal orientations: <0 0 1> in red, <1 0 1> in green and <1 1 1> in blue.

**Figure 5.7** Relative density of SLM Nickel samples plotted against input volumetric energy density at different hatch spacings.

**Figure 6.1** SEM micrograph of spherical Sn powders used for SLM.

**Figure 6.2** X-ray Diffraction analysis of tin powder and SLM processed tin powder. The analysis shows different relative peaks for the two materials.

**Figure 6.3** Optical microscopy images of SLM processed tin at a lower magnification, showing XY planes (a) and XZ planes (b), with pores circled in red.

**Figure 6.4** Optical microscopy: cross section (XZ plane) image of SLM processed tin near the edge, showing the zig-zag structure of the columnar crystal and twinned grains and recrystallized grains within original grain boundaries that result from working during polishing.

**Figure 6.5** Scanning electron microscopy of a cross-section (XZ plane) SLM processed tin sample, showing the contrast in texture due to different crystal grain orientations.

**Figure 6.6** EBSD analysis of SLM processed tin, displaying the different crystal orientations: <0 0 1> in red, <0 1 0> in green and <1 1 0> in blue.

**Figure 6.7** Relative density of SLM Tin samples plotted against input volumetric energy density at different hatch spacings.

**Figure 7.1** A “Black Box approach” summary of the semi-empirical modelling process.

**Figure 7.2** Updated plot of compensation factor against thermal conductivity with results from the experiments on tin, nickel and AlSi10Mg.

**Figure 7.3** Single melt track test for copper CU1332.

**Figure 7.4** Microscopy images of single melt tracks created at a laser power of 360 W, with enlarged images and tracing of the tracks at scanning speeds of 50 mm/s, 100mm/s and 150mm/s.

**Figure 7.5** Experiment on selective laser melting of copper powder CU1332.

**Figure 7.6** Plot of compensation factor against thermal conductivity with data from the experiments on copper powder CU1332.

# Abbreviations

| | |
|---|---|
| 3D | Three-Dimensional |
| AM | Additive Manufacturing |
| AMF | Additive Manufacturing File |
| CADCAM | Computer-Aided Design Computer-Aided-Manufacturing |
| CNC | Computer Numerical Control |
| DMLS | Direct Metal Laser Sintering |
| EBSD | Electron BackScatter Diffraction |
| EDX/EDXS | Energy Dispersive X-ray Spectroscopy |
| FCC | Face Centred Cubic |
| FDM | Fused Deposition Modelling |
| FESEM | Field Emission Scanning Electron Microscopy |
| HAGB | High Angle Grain Boundary |
| LAGB | Low Angle Grain Boundary |
| LOM | Light Optical Microscopy |
| MMC | Metal Matrix Composite |
| OEM | Original Equipment Manufacturer |
| PH | Precipitation Hardening |
| RP | Rapid Prototyping |
| SC3DP | Singapore Centre for 3D Printing |
| SEM | Scanning Electron Microscopy |
| SLM | Selective Laser Melting |
| SMA | Shape Memory Alloy |
| STL | Standard Tessellation Language |
| VED | Volumetric Energy Density |
| XML | eXtensible Mark-up Language |
| XRD | X-Ray Diffraction |

# Chapter 1

## Introduction

*In recent years, advances in additive manufacturing (AM), also known as three-dimensional (3D) printing, has been spurred by interests from governments and industries. Selective Laser Melting (SLM) is one of the most popular AM technologies as it can directly manufacture 3D metallic components from computer-aided design computer-aided-manufacturing (CADCAM) data [1-3].*

*Studies on SLM processing of materials and product characteristics have been carried out by researchers to enable the application of SLM to industries. The wide range of materials includes various grades of steel, titanium and titanium alloys, nickel-based superalloys, aluminium alloys, copper alloys and even precious metals such as gold. There is also observable increase in research interest in the SLM processing of metal matrix composites and ceramics. Process parameter optimization studies have to be carried out for each material to ensure the quality of the product. However, these optimization studies are often a lengthy process that involves selection of laser power-scanning speed combination through trial and error, selection of suitable layer thickness and sieving through a multitude of combinations of laser power, scanning speed, hatch spacing, and other parameters.*

*In order to shorten the process of parameter optimization, this Ph.D. project examines the development of a novel semi-empirical analytical model for the SLM process. The model will enable researchers to narrow down the range of possible parameters quickly based on material properties and machine characteristics, thereby increasing the success rate of material optimization studies and accelerating the advancement of 3D printing in SLM.*

## 1.1 Problem statement

AM, previously known as Rapid Prototyping (RP), is often to create prototypes for product development, learning, experimentation or presentation purposes. With the recent advancement in AM technology, functional components can also be fabricated for applications in the aerospace, automotive and medical industries. Compared to conventional subtractive manufacturing processes for metallic products, SLM has the following benefits:

1. There is less material wastage in SLM. For computer numerical control (CNC) processes such as drilling, grinding, milling and turning, the raw materials come in the form of cuboidal blocks, rods or sheets. The waste materials that are removed during the process cannot be reused, leading to wastage of materials. In SLM, powders left in the process can be recovered and reused for subsequent jobs.

2. AM offers flexibility in designs that subtractive manufacturing processes cannot. It can fabricate complex features, minute details and lattice structures that are not possible with traditional manufacturing technologies. Figure 1.1 shows some of the products fabricated by SLM, displaying complex structures with high-resolution details.

3. Tooling can be removed or reduced for manufacturing as SLM will be able to fabricate products in a single piece, thus reducing the inventory and associated costs significantly. Moreover, structural weakness related to joints and connecting parts can also be eliminated.

4. Product development time can be shortened and streamlined as prototypes can be immediately fabricated once the CAD data has been changed. Investments in moulds, tooling, and craftsmanship can be drastically reduced.

5. Individualized products and bespoke components can be fabricated in small scales and dissimilar products of the same material can be manufactured together. Whereas for many manufacturers, a single product, of one exact design, must reach a certain volume before being accepted for production to achieve economy of scale.

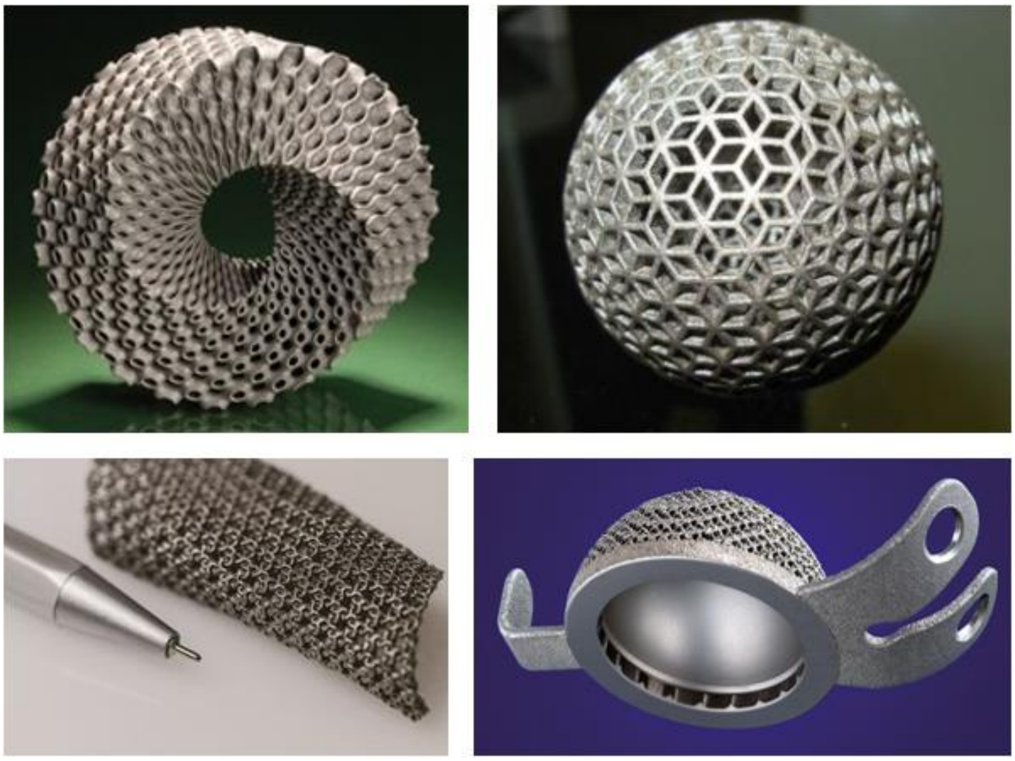

Figure 1.1 Complex geometries and minute structures by SLM [1].

With these advantages, SLM has been marked as one of the key additive manufacturing technologies for direct part manufacturing with metallic materials. Global revenue for AM products and services increased by four folds in the past five years. AM metals increased by 50 % in 2014 to USD 48.7 million and takes of 42.6 % of the total products and services revenues from AM [3]. Growth in this industry will continue to spur further innovations and research for SLM processing of different materials, such as metals, alloys, metallic glass and metal matrix composites (MMCs).

Process parameter optimization is important for SLM to produce high-density parts. However, parameter optimization studies have been a tedious process that involves many rounds of trial and error as careful process control is required [4] and different parameters are required for each and every material. This wastes valuable time, material, manpower, and money.

A novel model is required to facilitate these optimization studies, allowing researchers to narrow down the range of plausible parameters. Due to the dynamism of the SLM process, where rapid heating, melting, rapid cooling, volume shrinkage and solidification is involved, a simple analytical model is not possible. Hence, a semi-empirical approach is adopted.

## 1.2 Objective and Scope

The objective of this Ph.D. project is to develop a new semi-empirical model for the SLM process to facilitate process optimization studies. The model will be based on material properties and machine characteristics.

Although there are research and industrial interests in the SLM processing of composite material and ceramics, the scope of this project is limited to metals and alloys.

## 1.3 Dissertation Overview

This thesis addresses the development of a model for the SLM process.

Chapter 1 provides a rationale for the research and outlines the objectives and scope.

Chapter 2 reviews scientific literature concerning the SLM process with a focus on the SLM of metals and alloys. Previous attempts at modeling of the SLM process are also discussed. This provides the context for the Ph.D. work.

Chapter 3 discusses the principle and development of the semi-analytical model, which is based on the conservation of energy and thermal properties of the materials. It also covers the data from published literature concerning parameters of SLM process.

Chapter 4 elaborates the first major set of results from experiments carried out on AlSi10Mg and examines the resultant density against various input parameters.

Chapter 5 and Chapter 6 elaborates the experiments carried out on pure nickel and pure tin respectively.

Chapter 7 threads together the semi-empirical model and the data gathered from literature and the three sets of experiments. Applications and limitations of the model are also discussed.

Chapter 8 concludes the thesis.

## 1.4 Resulting Outcomes

This research led to several novel outcomes by:

1. Establishing a semi-empirical relationship between the SLM process parameters with the thermal properties of the materials.
2. Correlating the input energy density in the SLM process and the resultant relative density for various materials.
3. Optimizing the process parameters for the SLM of materials such as nickel and tin.

**References:**

[1] Chua, C.K. and K.F. Leong, *3D printing and additive manufacturing: principles and applications*. 4 ed. 2014, Singapore: World Scientific.

[2] Yap, C.Y., et al., *Review of selective laser melting: Materials and applications.* Applied Physics Reviews, 2015. **2**(4): p. 041101.

[3] Wohlers, T., *Wohlers report 2015*. 2015: Wohlers Associates.

[4] Kruth, J.P., et al., *Consolidation phenomena in laser and powder-bed based layered manufacturing.* CIRP Annals - Manufacturing Technology, 2007. **56**(2): p. 730-759.

# Chapter 2

# Literature Review

*Selective Laser Melting (SLM) is an Additive Manufacturing (AM) technique designed to process metallic powders using high power laser as energy source based on 3D CAD data as digital information. The part is fabricated by selectively melting and fusing powders in a layer, upon a preceding layer [1, 2]. Other methods are known as LaserCusing and Direct Metal Laser Sintering (DMLS) are the same in principle. For DMLS, "sintering" is recognized as a misnomer as the metallic powders are known to have completely melted and quickly solidified thereafter in the process [3]. Hence, for the purpose of this literature review, publications on SLM, LaserCusing and DMLS are included.*

*Since the patent for SLM was filed in 1998 [4], researchers have been exploring the processing of different materials with SLM. From various grades of steel [5, 6] to biocompatible alloys [7]; from precious metals [8] to metallic glass [9]; from metal matrix composites (MMCs) [10] to ceramic materials [11, 12], the pool of materials available to the SLM process is rapidly expanding. In this review, the emphasis is given metals and alloys as they make up the majority of the materials processed by SLM while the literature on SLM of MMCs and ceramics will be briefly covered.*

*There have also been many attempts to model the SLM process to study and understand the dynamics of SLM and to predict the resultant microstructure and properties of the fabricated parts. Most of these studies are through numerical analysis using various software, such as ANSYS [13] and COMSOL [14]. These works reveal important aspects of the process and integral factors to consider when developing a semi-empirical model for the SLM process.*

## 2.1 Overview of the Selective Laser Melting Process

SLM involves a series of operations from the conversion of CAD file in the Standard Tessellation Language (STL) format to a “build file” that contains the information required by the SLM machine to process, and the subsequent line-by-line and layer-by-layer automated fabrication of the desired object.

STL is a file format created by 3D Systems to contain surface geometrical information of a 3D object. An STL file describes a 3D object by a combination of the unit normal and vertices of triangles in the Cartesian coordinate system. It may also contain information on the colour of the surfaces although this is an add-on in the later stages of development. In order to overcome the limitations of the STL format, Additive Manufacturing File (AMF) format has been adopted by ASTM International in recent years to contain additional information describing shape and composition such as colour, texture, material, substructure and other properties of 3D objects to be processed by any AM systems [15]. It is based on extensible markup language (XML) and its ability to be compressed significantly allow for a more efficient transfer of data. However, STL file format is still the current *de facto* standard for transferring information between CAD programmes and manufacturing systems due to its widespread use over three decades.

In 3D printing, components with overhanging features usually require a support structure during the manufacturing process. For instance, in Fused Deposition Modelling (FDM) and Polyjet, support materials are available to provide support structures. These support structures can then be removed either manually or by dissolving in a solution [1]. In SLM, support structures have to be built with the same material as the component as the SLM systems can deposit only one type of powder for each layer. Magics, a software by Materialise NV, is capable of processing STL files, orientating the 3D model for fabrication and generating support structures for overhanging features

(Figure 2.1). After generating support structures, the data for every slice/layer that is required for the machines to process is generated. For SLM, this manufacturing data can be produced by the Build Processor modules in Magics.

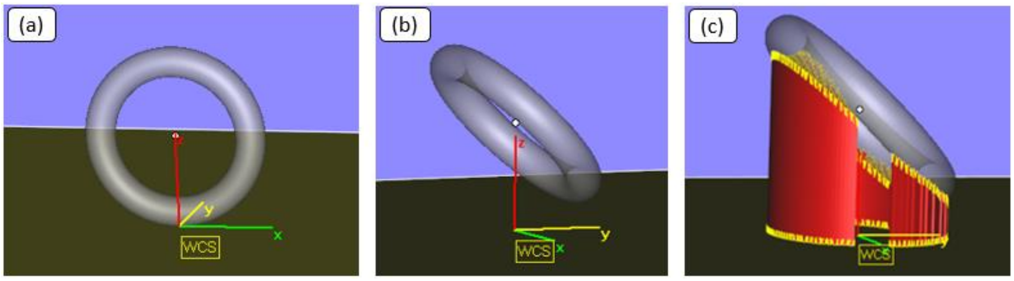

Figure 2.1 Processing of STL file with Magics, orientation with a 45° rotation from (a) to (b) and generation of support structures (c).

After the manufacturing data is fed to the SLM machine, the process starts by flushing the chamber with nitrogen or argon gas until the chamber has less than 2 % oxygen to minimize oxidation during the SLM process. Some of the SLM machines have the capability of providing platform heating up to 200 °C. That is followed by coating a thin layer of metallic powder on the substrate plate and laser scanning of the first layer of powders according to the manufacturing data. Once scanning of the first layer is completed, the platform is lowered in the *z*-axis by one layer thickness and a new layer of powder is deposited and spread evenly across the preceding layer. This process repeats itself until the required component is completely fabricated. After the fabrication process, loose powders are removed and the component is revealed. Powders that are not used in the process can be reused for the next job, minimizing wastage of materials. Figure 2.2 illustrates the concept of the SLM process with a relatively simple component.

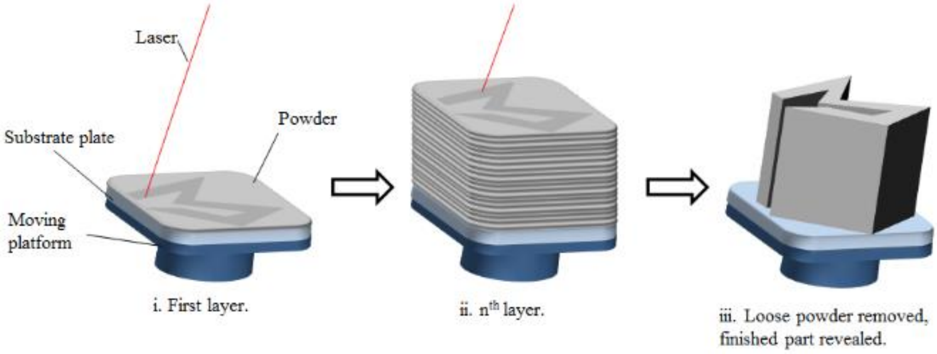

Figure 2.2 Layer-by-layer manufacturing of the SLM process. i) The high-power laser melts selective areas of the powder bed. ii) The process is repeated for successive layers. iii) Loose powder is removed and finished part is revealed [2].

### 2.1.1 Physical Phenomena and Process Parameters of SLM

The SLM process involves the rapid heating and melting of powder material with a laser beam and rapid solidification of the melted material. There are several important physical phenomena such as the absorptivity of the powder material to laser irradiation, the balling phenomenon that disrupts the formation of continuous melt vectors and the residual thermal stress caused by rapid fluctuation of temperature during the process. Residual thermal stresses can lead to crack formation and component failure. This section reviews the literature concerning these aspects of SLM to enhance the understanding of this dynamic manufacturing process.

In the earlier stages of development, the laser systems for SLM were a $CO_2$ laser ($\lambda \approx 10.6$ µm), adapted from the Selective Laser Sintering process. Later Nd:YAG fibre laser ($\lambda \approx 1.06$ µm) was adopted and currently most of the new machines are using Yb: YAG fibre laser. This is because metallic powders have higher absorptance to wavelengths of 1.06 µm, making Nd:YAG fibre laser a much more efficient energy source than its $CO_2$ counterpart. Furthermore, Yb:YAG crystal has a larger absorption bandwidth to reduce thermal management requirements for diode lasers, a longer upper-state lifetime and a lower thermal loading per unit pump power than Nd:YAG crystal. Advancements in laser technology are believed to continue bringing about higher energy efficiency to the SLM process.

The absorptance of material to laser irradiation can be defined as the ratio of the energy flux absorbed by the material to the energy flux incident upon the material. It affects the energy efficiency of the SLM process and even determines the feasibility of processing materials with a specific laser. However, there is little research done on the absorptance of powder materials to laser irradiation. During the SLM process, the laser is irradiated onto a thin powder bed and the absorptivity of powder materials to laser irradiation can be drastically different from their corresponding bulk materials. Tolochko et al. investigated the absorptance of powder materials to infrared irradiation of $CO_2$ laser (wavelength, $\lambda = 10.6\ \mu m$) and Nd:YAG laser ($\lambda = 1.06\ \mu m$) [16]. From their study, powder materials have significantly higher absorptance regardless of the wavelength of irradiation compared to their counterpart bulk materials. For example, at $\lambda = 1.06\ \mu m$, the absorptance of titanium powder is 77 % [16] while that of titanium bulk material is only 30 % [17].

Higher absorptance of the powder has been the subject of study for various research groups. In the research group led by Professor Jean-Pierre Kruth, Wang et al. studied the energy absorption and penetration with a 2D optical ray tracing model, taking into account the geometry and structure of the powder, and found that the maximum energy absorption in powders occurs below the surface [18]. Gusarov compared the effective absorptance of powder bed with the absorptance of bulk material. He also matched experimental data with both the isotropic specular reflection model and diffuse reflection model [19]. These models provide means to calculate the ratio of the total absorption with respect to the material absorption and to predict the optimal laser parameters with which to process a particular material. A similar explanation was given by Streek et al in their multiphase energy dissipation model [20]. In their model, the multiple internal reflections occur in the powder bed, increasing the number of incident irradiations on the powder material during the primary phase of energy dissipation (Figure 2.3). The model drastically increases the absorptance of powder material to irradiation.

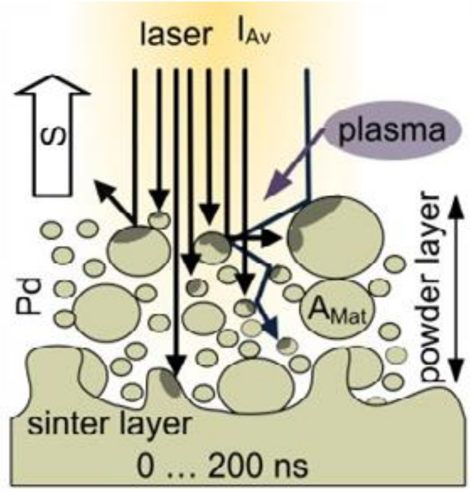

Figure 2.3 Primary dissipation of the multiphase energy dissipation, showing internal reflections of the laser irradiation in the powder bed [20].

In addition to the studies on laser irradiation and powder absorptance of energy, recent research works also examined the effects of the energy distribution profile of lasers and the difference between pulsed and continuous lasers. Loh et al. examined the different effects of Gaussian beam profile and uniform beam profile in SLM. Their investigation found that a uniform beam laser was able to achieve a larger melt width for a similar amount of melt penetration [21]. A high power uniform beam laser could thus be used to increase the rate of production in SLM.

In comparison to the commonly used continuous-wave laser, a pulsed laser can add another dimension of control to the SLM process as the laser pulse can be adjusted for different pulse durations, frequencies and pulse shapes. Mumtaz and Hopkinson reported a study on SLM of Inconel 625 with a pulsed laser and showed that a ramp-down pulse shape lowered the surface roughness of the top surface but was detrimental to that of the side surfaces [22]. However, the effects of pulse shape on other properties were yet to be tested and the scanning speed of this system was limited to 400 mm/s.

Powder size and powder distribution also have effects on the absorptance of the powder bed. A study suggests that for 316L stainless steel, powders with $D_{50}$ of 15 µm and 28 µm require lower energy densities to achieve near full density than the powder with $D_{50}$ of 38 µm [23]. Another study by Liu et al confirmed this finding and added that smaller powders result in better surface finish [24]. Moreover, powders with a narrow range of particle size flow better and generate parts with higher strength and hardness. These studies only showed some of the possible effects of powder size and size distribution on the required SLM processing parameters.

The second physical phenomenon in the discussion is that of “balling”. It happens when molten metal forms spheroidal beads due to surface tension and insufficient wetting of the preceding layer [25]. “Balling” results in rough, bead-shaped surfaces and obstructs the formation of continuous melt vectors. In more severe cases, balling may aggravate over several layers and jam the powder coating mechanism with large metallic beads that extends above the powder bed as illustrated in Figure 2.4 [26]. Kruth et al. explained that an oxide film on the preceding layer impedes interlayer bonding and leads to balling as liquid metals generally do not wet oxide films in the absence of a chemical reaction [27]. Hence, “balling” can be reduced by keeping oxygen level at 0.1 %, applying a combination of high laser power and low scanning speed or applying re-scanning of the laser.

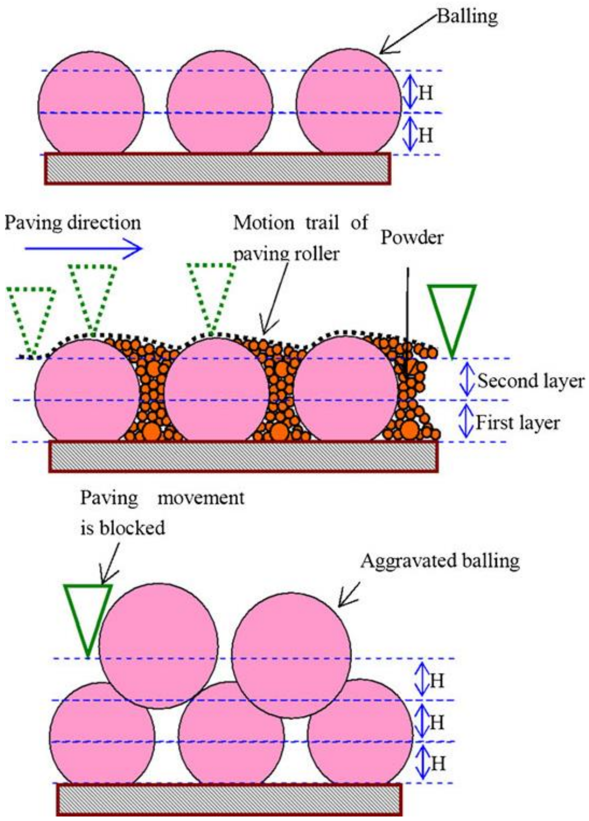
Balling
H
H
Paving direction
Motion trail of paving roller
Powder
Second layer
First layer
Paving movement is blocked
Aggravated balling
H
H
H

Figure 2.4 Severe balling over several layers in SLM [26].

Besides powder absorption of laser irradiation and "balling", residual thermal stress is another important physical aspect of the SLM process. During the manufacturing process, the materials experience varying degrees of thermal fluctuation. This causes residual stress on the components built, as explained by Kruth et al. with the Temperature Gradient Mechanism (Figure 2.5) [28]. Even when cracks or delamination do not occur, there is residual stress in the fabricated component. Shiomi et al. examined methods of reducing residual in SLM components [29]. It was found that post-process heat treatment at 600 °C to 700 °C for 1 hour reduced residual stress by 70 %; re-scanning of the laser with the same parameters as the SLM forming process reduced residual stress by 55%; and heating of powder bed to 160 °C resulted in a 40 % reduction.

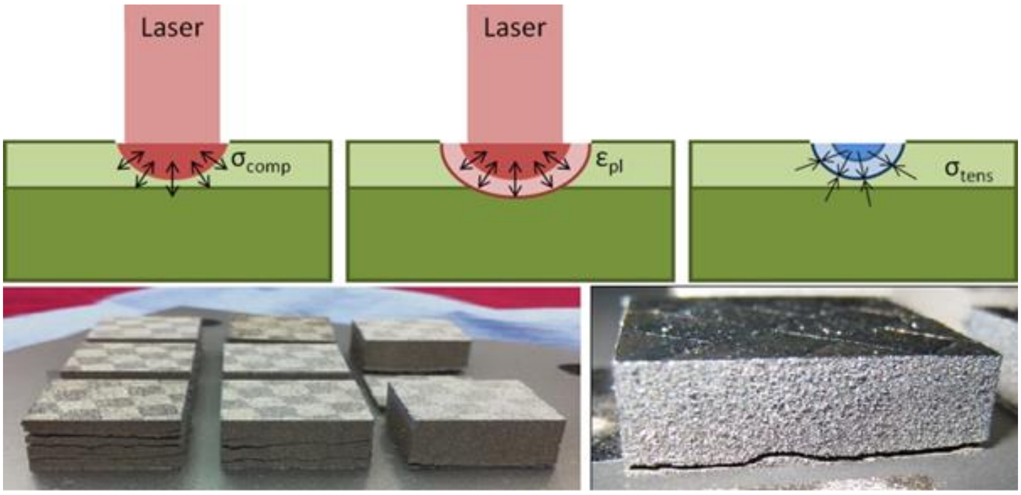

Figure 2.5 Temperature Gradient Mechanism (top) leading to crack formation and delamination of manufactured parts [28].

Yasa et al. introduced “sectorial scanning” as a scanning strategy in SLM. This strategy divides a layer into small square grids akin to a chessboard and the neighbouring grids are scanned perpendicular to one another [30]. “Sectorial scanning” reduced the residual stress significantly, it is now available in SLM Build Processor software and is known as chessboard strategy.

Laser power, scanning speed, hatch spacing, and layer thickness are the process parameters commonly examined to optimize the SLM process (Figure 2.6). These parameters affect the input volumetric energy density (VED) that is available to heat up and melt the powders. Insufficient energy often results in balling due to lack of wetting of molten pool with the preceding layer [26]. Balling is usually caused by a combination of low laser power, high scanning speed, and large layer thickness. However, high laser and low scanning speed may result in extensive material evaporation and the keyhole effect [31]. Hence, understanding and carefully selecting laser power, scanning speed, hatch spacing, and layer thickness is integral for SLM to produce near full-density parts.

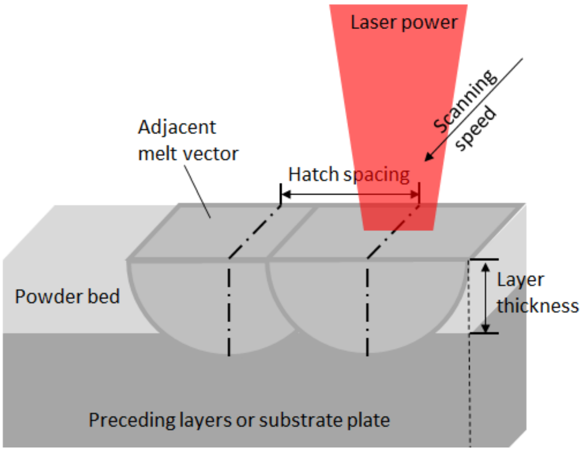

Figure 2.6 Illustration of common SLM parameters: laser power, scanning speed, hatch spacing and layer thickness [2].

The laser power determines the energy that the system delivers to the powder bed through one laser at any moment, usually measured in Watts for the SLM process. Most systems are equipped with continuous-wave laser modules capable of delivering up to 400 W. In more advanced systems developed by EOS and SLM Solutions GmbH, laser modules capable of delivering up to 1,000 W are also adopted. However, a higher laser power may not indicate a higher energy flux density as the focus spot diameter may differ for different laser modules and individual systems. For instance, in the SLM 280 HL developed by SLM Solutions GmbH, there are two laser modules. The first module has a maximum power of 400 W and a focus spot diameter of 80 µm. Its second module has a maximum power of 1,000 W and a much larger focus spot diameter of 730 µm. Moreover, the energy profiles of these two modules are also different. Module 1 has a Gaussian distribution profile while module 2 has a flat-top distribution profile. In larger systems such as SLM 500 HL, two lasers may operate simultaneously, covering different areas and improving the building rate.

Scanning speed is another important process parameter, alongside laser power, as it affects the formation of melt lines [32] and determines the porosity, hardness and mechanical properties of the fabricated material [33]. At low scanning speeds, distortions and irregularities occur in the melt pool and cause instabilities during the SLM process. On the other hand, high speed gives rise to the balling effect as there was insufficient wetting of the previous layer. The range of the optimal scanning speed is affected by the laser power deployed and the thermal conductivity of the material [32]. Among the publications surveyed, the scanning speeds used are between 50 mm/s and 1000 mm/s. It is uncommon to have scanning speeds higher than 2000 mm/s.

The hatch spacing can be defined as the distance between the centreline of adjacent melt vectors as shown in Figure 2.6. The hatch spacing for the SLM process must be carefully selected based on the melt width and the cross section of the melt. If the hatch spacing is too large, there will be insufficient bonding between adjacent melt tracks and result in regular porosity in the fabricated component. These pores will weaken the structure as they are sites of stress concentration and points of crack initiation. Overly small hatch spacing will cause excessive re-melting of neighbouring melt tracks, resulting in a waste of energy. Hence, hatch spacing must also be carefully selected to minimize both porosity and energy wastage. In most literature, the hatch spacing deployed for the SLM process is between 50 µm to 200 µm.

For the SLM process, the layer thickness of each layer is commonly kept between 20 to 100 µm. Layer thickness is chosen as a compromise between high vertical resolution and having good powder flowability [34]. Powders with large particulate sizes result in poor resolution and build tolerance. For instance, as powders at the edges of the component geometry may be partially melted or embedded in the melt pool, surface roughness will increase with larger particle size. However, smaller powders have higher tendency to agglomerate together, due to van der Waals forces, resulting in poor powder flowability and hence poor powder deposition. In a study, researchers have attempted to improve the flowability of light-weight ceramic powders for use in the SLM process by subjecting the powders to spray-drying. The resultant powder showed improved flowability and was able to form a thin evenly distributed layer on the substrate plate [35].

### 2.1.2 SLM of Metals and Alloys

The SLM process has been proven capable of direct fabrication with various metals and alloys. Over three decades, materials such as 316L stainless steel, M2 tool steel, titanium, Ti6Al4V, AlSi10Mg, CoCr alloy and Inconel superalloys have become some of the most popular materials. These materials have applications in medicine, dentistry, automobile and aerospace industries. Table 2.1 summarizes the metals and alloys that have been tested and published in scientific literature.

Table 2.1 Types of metals and alloys researched for the SLM process.

| **Material** | **References** |
|---|---|
| *Iron, ferrous alloys, and steels* | |
| Iron | [36, 37] |
| Fe alloy: Cr 15 %, B 1.5 %, Fe bal. | [38] |
| Fe alloy: Ni 12.4 %, 4.4 Cr %, 1.3 % P, Cu 0.4 %, Fe bal. | [39, 40] |
| Fe alloy: Ni 29 %, Cu 8-10 %, P 1-2 %, Fe bal. | [39, 41-43] |
| FeAl intermetallics | [44] |
| Iron aluminide alloy | [45] |
| 304 stainless steel | [46, 47] |
| 314S stainless steel | [48] |
| 316L stainless steel | [49-53] |
| 904L stainless steel | [54] |
| M2 tool steel | [5, 48, 55] |
| H13 tool steel | [48, 56] |
| H20 tool steel | [57] |
| Tool steel X110CrMoVAl 8-2 | [58] |
| Ultra-high carbon steel (C 2.2 %) | [59] |
| SCM440 chrome molybdenum steel | [29] |
| Precipitation Hardening steel | [60-62] |
| Maraging Steel Grade 300 | [63, 64] |
| *Titanium and titanium based alloys* | |
| Titanium | [65-68] |
| Ti-6Al-4V | [62, 69-71] |
| Ti-6Al-7Nb | [72-75] |

| | |
|---|---|
| Ti-13Nb-13Zr | [76] |
| Ti-24Nb-4Zr-8Sn | [77, 78] |
| Ti-13Zr-Nb | [79] |
| *Nickel based alloys* | |
| Ni alloy: Cr 9.4%, B 1.8 %, Si 2.8 %, Fe 2 %, C 0.4 %, Ni bal. | [65, 80] |
| Inconel 625 | [22, 54, 81, 82] |
| Inconel 718 | [83-85] |
| Inconel 738LC | [86] |
| Hastelloy X | [87-89] |
| Nimonic 263 | [90] |
| Mar M-247 | [91] |
| CM247LC | [92] |
| Ni-Ti Shape Memory Alloy | [34, 93-95] |
| *Aluminium and aluminium based alloys* | |
| Aluminium | [96-98] |
| AA6061 | [52, 98, 99] |
| Al-6Mg | [96] |
| Al-12Si | [96, 99] |
| AlSi10Mg | [100-103] |
| *Copper and copper-based alloys* | |
| Copper | [104, 105] |
| Cu alloy: Ni 15.2%, Sn 6.4 %, P 1.6 %, Fe 0.05 %, Cr 0.05 %, Cu bal. | [39] |
| C18400 | [106] |
| K220 | [107] |
| Cu-Al-Ni-Mn Shape Memory Alloy | [108] |
| *Other metals and alloys* | |
| Magnesium | [109, 110] |
| Mg-Al alloy | [111] |
| CoCr alloy | [112-114] |
| Tungsten | [115, 116] |
| W-Ni-Fe alloy | [117, 118] |
| W-Ni-Cu alloy | [119] |
| Gold | [8, 120, 121] |
| Silver | [122, 123] |
| Tantalum | [124] |
| Metallic glass | [9, 125] |

Most of the research publications on SLM of ferrous metals are based on 316L stainless steel. Jandin et al. published the first paper reporting successful SLM of 316L stainless steel [49] and Tolosa et al. achieved 99.9% relative for SLM 316L stainless steel [53]. Jerrard et al. investigated the SLM of 316L austenitic stainless steel and 17-4 precipitation hardening (PH) martensitic stainless steel powder mixture [126]. Their work showed that hardness and magnetic adherence of the SLM component can be adjusted by varying the compositional ratio of the contents. Hence, new grades of steel can be produced by exploiting the flexibility of the SLM process to tailor materials with specific properties as required by function and need.

Commercially pure titanium and Ti-6Al-4V alloy are also popular materials with the SLM research community. As titanium is highly susceptible to oxidation in the molten state, the inert gas is used in the SLM process. The inert gas, argon or nitrogen, flushes out atmospheric air and bring the oxygen level below 0.5 %. Other titanium based alloys such as Ti6Al7Nb has been examined to replace the Ti6Al4V due to its controversial vanadium composition. Ti24Nb4Zr8Sn and Ti13Nb13Zr have also been studied to provide low moduli titanium alloys. These alloys can reduce the moduli mismatch with bone tissues and produce an implant with lower possibilities of bone resorption.

For nickel based alloys, Inconel 625 is the most popular material. Research on other nickel based alloys such as Inconel 718, Chromel, Hastelloy X, Nimonic 263, IN738LC and MAR-M 247 mainly focus on the process parameters for formation of stable melt track since these works are mostly in their infancy. An interesting nickel-based material studied for the SLM process is shape memory alloy (SMA) NiTi. Research has successfully produced two-way trained NiTi with a relatively gradual phase transition [34].

Aluminium, copper, magnesium, cobalt-chrome, tungsten, gold, silver, and tantalum have also been studied for the SLM process. However, publications on each of these metals are significantly fewer than those of steel, titanium and nickel-based alloys. Most of the works on SLM of aluminium alloys are based on AlSi10Mg, a common casting alloy.

There is a high degree of difficulty in processing copper with SLM. This difficulty is due to copper’s high reflectivity and high thermal conductivity.

Copper powders display a relatively low absorptivity to both Nd:YAG laser (63 %) and $CO_2$ laser (32 %) irradiation [16] and cause the energy consumption to increase when fabricating copper parts. Moreover, copper is also high reactivity to atmospheric oxygen, leading to storage problems for copper and copper-based powders. Compared to pure copper, SLM of copper alloys such as K220 and C18400 have also seen greater success where relative densities higher than 95 % have been achieved [106, 107].

Magnesium poses a new challenge for the SLM process due to its high reactivity to oxygen and flammability. SLM of magnesium has thus far met with limited success. However, the material is of interest due to its potential application in medicine as biocompatible implants.

Tungsten has also been studied for the SLM process. Its high melting point of 3420 °C and low wettability make it difficult to machine into complex shapes or to apply powder metallurgy. SLM provides a feasible alternative to the processing of tungsten and widens its potential for applications. Research has also been done for other metals such as cobalt-chromium alloy, gold, silver, and tantalum. In more recent developments, SLM has also been studied as a feasible processing technique for the production of bulk metallic glass. Metallic glass has many desirable characteristics such as near-theoretical strength, low Young’s modulus, and high elasticity. Conventional methods have limited the shape of the metallic glass to rods or ribbons whereas SLM will be able to produce bulk metallic glass and widen its field of applications.

In assessing the success of processing various materials with SLM, the relative density is one common yardstick. It gives an indication of the ability of SLM to produce near full density components with a particular material. Table 2.2 lists the materials with their highest relative density reported. Studies have shown that some materials such as 316L stainless steel, maraging steel (grade 300), Ti-6Al-4V, Ti-6Al-7Nb, Inconel 718, K220 and CoCr alloys can be processed to near full density by SLM. Common methods for measuring the relative density or porosity include applying Archimedes principle and image analysis of the samples' cross sections.

Table 2.2 List of materials studied for SLM and the highest relative densities reported.

| **Material** | **References** | **Relative density** |
|---|---|---|
| *Iron, ferrous alloys and steels* | | |
| Iron | [37] | 99.0 % |
| Fe alloy: Ni 12.4 %, 4.4 Cr %, 1.3 % P, Cu 0.4 %, Fe bal. | [39] | 99.5 % |
| Fe alloy: Ni 29 %, Cu 8-10 %, P 1-2 %, Fe bal. | [43] | 97.5 % |
| FeAl intermetallics | [44] | 98.0 % |
| Iron aluminide alloy | [45] | 99.5 % |
| 304 stainless steel | [47] | 92.0 % |
| 316L stainless steel | [53] | 99.9 % |
| M2 tool steel | [5] | 97.0 % |
| H13 tool steel | [56] | 90.0 % |
| H20 tool steel | [57] | 99.5 % |
| Ultra-high carbon steel | [59] | 92.0 % |
| Maraging Steel Grade 300 | [64] | 99.9 % |
| *Titanium and titanium based alloys* | | |
| Titanium | [68] | 99.5 % |
| Ti-6Al-4V | [71] | 99.9 % |
| Ti-6Al-7Nb | [75] | 99.9 % |
| Ti-24Nb-4Zr-8Sn | [78] | 99.5 % |
| *Nickel based alloys* | | |
| Ni alloy: Cr 9.4%, B 1.8 %, Si 2.8 %, Fe 2 %, C 0.4 %, Ni bal. | [65] | 88.0 % |
| Inconel 625 | [82] | 95.0 % |
| Inconel 718 | [114] | 99.9 % |
| Hastelloy X | [88] | 99.8 % |
| Nimonic 263 | [90] | 99.7 % |
| *Aluminium and aluminium based alloys* | | |
| AA6061 | [98] | 96.5 % |
| AlSi10Mg | [103] | 99.5 % |
| *Copper and copper-based alloys* | | |
| C18400 | [106] | 96.7 % |
| K220 | [107] | 99.9 % |
| Cu-Al-Ni-Mn Shape Memory Alloy | [108] | 92.4 % |
| *Other metals and alloys* | | |
| Mg-Al alloy | [111] | 82.0 % |
| CoCr alloy | [114] | 99.9 % |
| Tungsten | [116] | 89.9 % |
| Gold | [120] | 89.6 % |

Besides relative density, microhardness, tensile strength and surface roughness are three properties commonly examined in studies of SLM processed materials [2]. Most studies have shown that SLM produced parts have higher microhardness and tensile strength compared to their cast counterparts. However, they have lower ductility. Rapid localised solidification results in a more uniform chemical composition throughout the parts. Microstructure observations of SLM components have also shown crystal grains and dendritic features on the micro scale. These factors have led to higher strength and hardness. Moreover, the possibility of processing metallic glass has also allowed SLM to produce parts with near theoretical strength and hardness, paving the way for manufacturing of high strength and high hardness products.

Surface roughness for SLM is mostly unsatisfactory for industrial standards. It is common to see the roughness of 10 µm to 25 µm ($R_a$) for raw products. Surfaces at the top can be improved by applying a re-melting process [127]. Post process surface treatments such as sandblasting or shot peening can bring the surface roughness down to 5 µm or lower ($R_a$) [2].

In addition, there is also research in the area of multi-material printing for SLM. Researchers exploit the flexibility of the SLM process to fabricate components with dissimilar materials [128]. For example, it is usually difficult to weld steel and copper alloys together. However, these materials can be used together in SLM due to the rapid and localised solidification nature of the process [129]. Joining of dissimilar metals can open up possibilities for various applications.

Besides metals and alloys, SLM has also been studied for the processing of metal matrix composites (MMCs) and ceramic materials. These materials provide unique challenges to the SLM process and opportunities for new applications.

SLM of MMCs involves a mixture of two or more types of powders, usually with the metallic powder acting as the matrix material. Ceramic powders and carbon nanotubes are popular as reinforcement materials. For example, Gu used nano-sized TiC powders to reinforce titanium and processed them with SLM [10]. Reinforcement particles can also be formed in-situ during the SLM process. SLM of a powder mixture containing titanium powder and silicon nitride ($Si_3N_4$) with a molar ratio of 9:1 causes a reaction: $9Ti + Si_3N_4 = 4TiN + Ti_5Si_3$. The $Ti_5Si_3$ matrix was reinforced by granular TiN [130]. The relative density achieved for SLM MMCs range between 82 % and 99.7 %. Significant improvements can be seen in the microhardness and wear rate of the composites over their metal counterparts [2]. SLM process parameters of MMCs are often not far off from the parameters for the metal matrix material. Hence, development of MMCs is a short step away once the parameters for the respective metallic material are optimized.

However, SLM of ceramics has achieved limited success in comparison. Ceramic materials have high melting point and relatively low absorptivity to Nd:YAG laser. Combined with its inherently low ductility, ceramics are prone to contain cracks when processed with SLM due to the constant thermal fluctuation. Hence, processing of ceramics with SLM is extremely difficult. Even when successful, the products have a very high surface roughness ($R_a$ = 150 µm) and the process is energy consuming [11]. Moreover, ceramics are less dense than metals and ceramic powders have poor flowability. This impedes ceramic powders from forming a thin and evenly distributed layer on the substrate plate and previous layers. Only a few research groups have successfully produced ceramic parts with SLM and only alumina-zirconia ($Al_2O_3$-$ZrO_2$) mixture has been shown to achieve near full density [11]. Nonetheless, SLM of ceramics could be made feasible by using a $CO_2$ laser, for a more efficient absorption of laser energy, multiple laser systems, for providing localised preheating and melting of the desired spot, and a powder delivery system capable of coating thin layers of ceramic powders.

### 2.1.3 Modelling of the SLM Process

SLM is a dynamic process that involves rapid heating, melting, rapid cooling and solidification of small localised areas. Often, these areas experience partial re-melting as bonding to adjacent melt lines and neighbouring layers are required. In addition to the process parameters, thermal history of the components also matters. Hence, factors such as scanning strategy also affect the properties of the SLM component. There have been many attempts at understanding the dynamism of the SLM process via modelling and simulation.

A theoretical study on the SLM process would be difficult because of its complex and dynamic nature. The process would involve a change of phase, change of volume, loss of heat energy, loss of mass and many other factors. Thus far, theoretical studies on SLM have been limited to the heat transfer phenomenon. A theoretical solution was proposed by Woo et al. to predict the temperature distribution in the laser hardening process [131]. The surface laser hardening process is similar to the SLM process as it uses a laser as an energy source to process a thin layer of powder on a substrate. However, the laser used in surface hardening process has a much larger laser spot (14 mm × 14 mm). Later analytical studies and models have also been proposed and these models considered a homogeneous medium for the process [132, 133].

Some earlier works sought to understand the effects of very specific phenomena. For instance, the absorptance of irradiation of different wavelengths has been well studied for bulk materials but not for powder materials. Hence, Tolochko et al examined some commonly used powders and tested their absorptivity to two particular wavelengths, 10.6 µm ($CO_2$ laser) and 1.06 µm (Nd:YAG laser) [16]. The topic of effective powder bed thermal conductivity was explored by Gusarov et al to estimate the temperature field of the powder bed during the process. It was found that the effective conductivity of the powder bed is affected by the relative density of the powder bed, the mean coordination number and the contact size ratio, i.e. the ratio of the contact spot radius to the spherical radius of the powder [134]. On the same topic of thermal conductivity, later studies by Alkahari et al also confirmed that thermal conductivity increases with powder bulk density and powder particle diameter [135].

The first paper on numerical simulation of the SLM process was published by Matsumoto et al, on the distribution of temperature and stress on a single solidified layer [136]. Much of the later works involved 3D simulations of the SLM process and many factors were examined: phase change [14, 137], volume shrinkage [14, 138], material loss through vaporization [14], heat loss through radiation [19], laser beam geometry [139] and surface tension [140]. Others focused on simulation parameters such as the type of simulated heat source [141], the boundary conditions [142] and the use of dynamic meshing over static meshing [143]. Figure 2.7 illustrates a typical 2D simulation and 3D simulation of the SLM process. Most of these simulation work involves the assumption that the powder bed acts as a homogenous continuous medium. A simulation study was made by taking into account the particle nature of the powder bed. This model was able to recreate the process of balling and melt track formation in SLM to yield a better understanding of this technology [144] as shown in Figure 2.8.

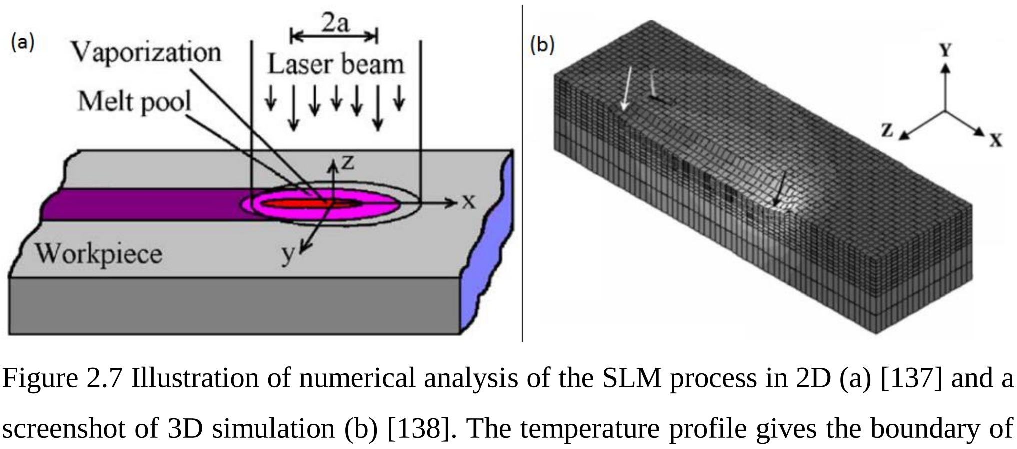

Figure 2.7 Illustration of numerical analysis of the SLM process in 2D (a) [137] and a screenshot of 3D simulation (b) [138]. The temperature profile gives the boundary of the melt pool and shows the possibility of vaporization.

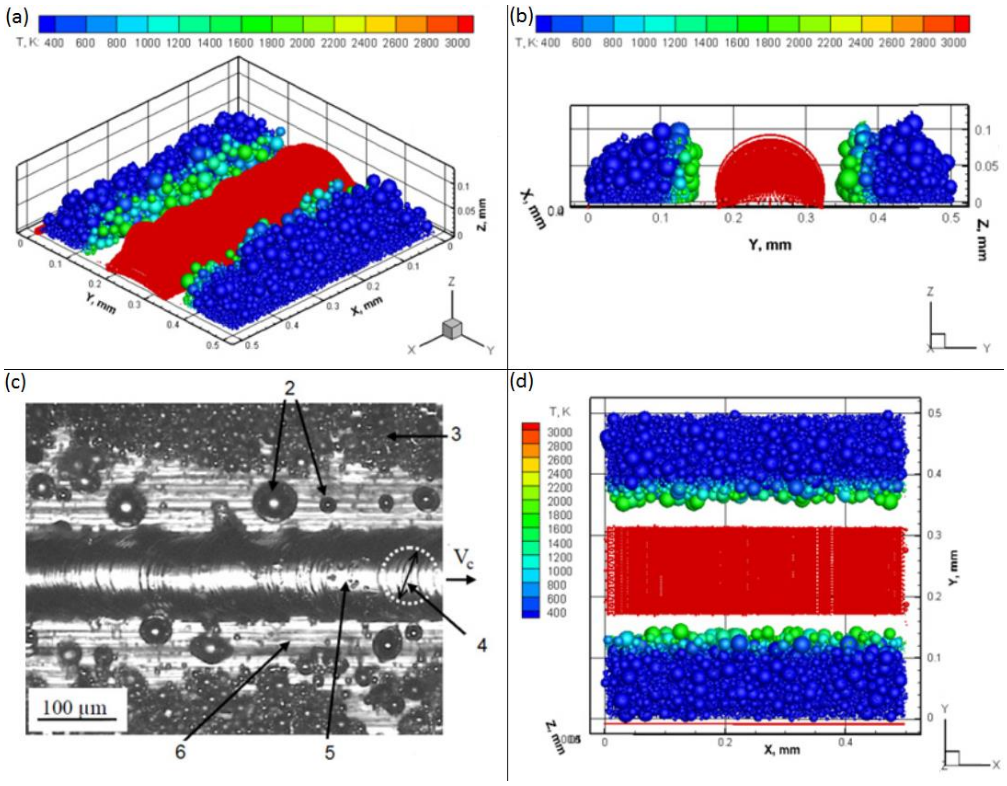
(a)
T, K 400 600 800 1000 1200 1400 1600 1800 2000 2200 2400 2600 2800 3000
Y, mm
X, mm
Z, mm
(b)
T, K 400 600 800 1000 1200 1400 1600 1800 2000 2200 2400 2600 2800 3000
Y, mm
X, mm
Z, mm
(c)
2
3
4
5
6
$V_c$
100 μm
(d)
T, K
3000
2800
2600
2400
2200
2000
1800
1600
1400
1200
1000
800
600
400
X, mm
Y, mm
Z, mm

Figure 2.8 Simulation of SLM by factoring in the powder bed nature of the process [144].

From this literature, it can be observed that some factors are consistently considered and factored into numerical analyses. These factors include thermal properties of the material, the absorptance of the material to laser irradiation, the density of the material and relative density of the respective powder bed. The output of these simulation work often gives the thermal profile of the powder bed or material, where a boundary, usually according to the melting temperature, gives an indication of the melt pool and size of the melt track. Additional information from these simulations may also include the instantaneous thermal stress and residual stress in the components.

## 2.2 Ph.D. in Context of Literature

Research on SLM processing of a new material often involves an iterative process of finding the optimal combination of laser power, scanning speed, hatch spacing and, sometimes, layer thickness. The laborious and time-consuming process can be shortened by carrying out a numerical simulation of the process with new material parameters. However, accurate simulations also require computing time and simulation methods have to be verified against experimental results. Hence, in this Ph.D. work, an analytical model of the SLM process is developed with an empirical approach. The model will allow researchers to narrow down the energy requirement quickly and deduce the range of process parameters for new material.

**References:**

[1] Chua, C.K. and K.F. Leong, *3D printing and additive manufacturing: principles and applications*. 4 ed. 2014, Singapore: World Scientific.

[2] Yap, C.Y., et al., *Review of selective laser melting: Materials and applications.* Applied Physics Reviews, 2015. **2**(4): p. 041101.

[3] Novak-Marcincin, J., *Design of Manufacturing Systems by Rapid Prototyping Technology Application.* Annals of the University of Petroşani, Mechanical Engineering, 2012. **14**: p. 104-111.

[4] Meiners, W., K. Wissenbach, and A. Gasser, *Shaped body especially prototype or replacement part production*. 1998.

[5] Liu, Z.H., et al., *Crystal structure analysis of M2 high speed steel parts produced by selective laser melting.* Materials Characterization, 2013. **84**: p. 72-80.

[6] Niendorf, T., et al., *Highly Anisotropic Steel Processed by Selective Laser Melting.* Metallurgical and Materials Transactions B, 2013. **44**(4): p. 794-796.

[7] Sun, J., Y. Yang, and D. Wang, *Mechanical properties of a Ti6Al4V porous structure produced by selective laser melting.* Materials & Design, 2013. **49**: p. 545-552.

[8] Khan, M. and P. Dickens, *Selective laser melting (SLM) of gold (Au).* Rapid Prototyping Journal, 2012. **18**(1): p. 81-94.

[9] Pauly, S., et al., *Processing metallic glasses by selective laser melting.* Materials Today, 2013. **16**(1-2): p. 37-41.

[10] Gu, D., et al., *Selective laser melting of TiC/Ti bulk nanocomposites: Influence of nanoscale reinforcement.* Scripta Materialia, 2012. **67**(2): p. 185-188.

[11] Hagedorn, Y.-C., et al., *Net shaped high performance oxide ceramic parts by selective laser melting.* Physics Procedia, 2010. **5**: p. 587-594.

[12] Yap, C.Y., et al. *Single track and single layer melting of silica by Seletive Laser Melting*. in *6th International Conference on Advanced Research in Virtual and Rapid Prototyping*. 2013. Leiria, Portugal: CRC Press.

[13] Hussein, A., et al., *Finite element simulation of the temperature and stress fields in single layers built without-support in selective laser melting.* Materials & Design, 2013. **52**: p. 638-647.

[14] Loh, L.-E., et al., *Numerical investigation and an effective modelling on the Selective Laser Melting (SLM) process with aluminium alloy 6061.* International Journal of Heat and Mass Transfer, 2015. **80**: p. 288-300.

[15] International, A., *ISO/ASTM 52915:2013(E)*, in *Standard Specification for Additive Manufacturing File Format (AMF) Version 1.1*. 2013, ASTM International.

[16] Tolochko, N.K., et al., *Absorptance of powder materials suitable for laser sintering.* Rapid Prototyping Journal, 2000. **6**(3): p. 155-161.

[17] Fischer, P., et al., *Sintering of commercially pure titanium powder with a Nd:YAG laser source.* Acta Materialia, 2003. **51**(6): p. 1651-1662.

[18] Wang, X., et al., *Direct selective laser sintering of hard metal powders: experimental study and simulation.* The International Journal of Advanced Manufacturing Technology, 2002. **19**(5): p. 351-357.

[19] Gusarov, A.V. and J.P. Kruth, *Modelling of radiation transfer in metallic powders at laser treatment.* International Journal of Heat and Mass Transfer, 2005. **48**(16): p. 3423-3434.

[20] Streek, A., P. Regenfuss, and H. Exner, *Fundamentals of Energy Conversion and Dissipation in Powder Layers during Laser Micro Sintering.* Physics Procedia, 2013. **41**: p. 858-869.

[21] Loh, L.E., et al., *Selective Laser Melting of aluminium alloy using a uniform beam profile.* Virtual and Physical Prototyping, 2014. **9**(1): p. 11-16.

[22] Mumtaz, K. and N. Hopkinson, *Selective laser melting of Inconel 625 using pulse shaping.* Rapid Prototyping Journal, 2010. **16**(4): p. 248-257.

[23] Spierings, A.B., N. Herres, and G. Levy, *Influence of the particle size distribution on surface quality and mechanical properties in AM steel parts.* Rapid Prototyping Journal, 2011. **17**(3): p. 195-202.

[24] Liu, B., et al. *Investigation the effect of particle size distribution on processing parameters optimisation in Selective Laser Melting process*. in *International solid freeform fabrication symposium: an additive manufacturing conference. University of Texas at Austin, Austin*. 2011.

[25] Tolochko, N.K., et al., *Balling processes during selective laser treatment of powders.* Rapid Prototyping Journal, 2004. **10**(2): p. 78-87.

[26] Li, R., et al., *Balling behavior of stainless steel and nickel powder during selective laser melting process.* The International Journal of Advanced Manufacturing Technology, 2011. **59**(9-12): p. 1025-1035.

[27] Kruth, J.P., et al., *Selective laser melting of iron-based powder.* Journal of Materials Processing Technology, 2004. **149**(1-3): p. 616-622.

[28] Kempen, K., et al. *Lowering thermal gradients in Selective Laser melting by pre-heating the baseplate*. in *Solid Freeform Fabrication Symposium Proceedings*. 2013. Austin, Texas, USA: The University of Texas at Austin.

[29] Shiomi, M., et al., *Residual Stress within Metallic Model Made by Selective Laser Melting Process.* CIRP Annals - Manufacturing Technology, 2004. **53**(1): p. 195-198.

[30] Yasa, E., et al. *Investigation of sectoral scanning in selective laser melting*. in *ASME 2010 10th Biennial Conference on Engineering Systems Design and Analysis*. 2010. American Society of Mechanical Engineers.

[31] Krakhmalev, P. and I. Yadroitsev, *Microstructure and properties of intermetallic composite coatings fabricated by selective laser melting of Ti–SiC powder mixtures.* Intermetallics, 2014. **46**: p. 147-155.

[32] Yadroitsev, I., et al., *Single track formation in selective laser melting of metal powders.* Journal of Materials Processing Technology, 2010. **210**(12): p. 1624-1631.

[33] Yadroitsev, I., P. Bertrand, and I. Smurov, *Parametric analysis of the selective laser melting process.* Applied Surface Science, 2007. **253**(19): p. 8064-8069.

[34] Clare, A.T., et al., *Selective laser melting of high aspect ratio 3D nickel–titanium structures two way trained for MEMS applications.* International Journal of Mechanics and Materials in Design, 2007. **4**(2): p. 181-187.

[35] Mapar, M., et al. *Preparation and flowability characterization of ceramic powders for Selective Laser Melting*. in *6th International Conference on Advanced Research in Virtual and Rapid Prototyping*. 2013. Leiria, Portugal: CRC Press.

[36] Rombouts, M., et al., *Fundamentals of Selective Laser Melting of alloyed steel powders.* CIRP Annals - Manufacturing Technology, 2006. **55**(1): p. 187-192.

[37] Song, B., et al., *Microstructure and tensile properties of iron parts fabricated by selective laser melting.* Optics & Laser Technology, 2014. **56**: p. 451-460.

[38] Sun, M., L. Lu, and J.Y. Fuh. *Microstructure and properties of Fe-base alloy fabricated using selective laser melting*. in *Second International Symposium on Laser Precision Micromachining*. 2002. International Society for Optics and Photonics.

[39] Sustarsic, B., et al., *Microstructure and Mechanical Characteristics of DMLS Tool-Inserts.* Materials and Manufacturing Processes, 2009. **24**(7-8): p. 837-841.

[40] Amanov, A., et al., *An investigation of the tribological and nano-scratch behaviors of Fe–Ni–Cr alloy sintered by direct metal laser sintering.* Materials & Design, 2013. **47**: p. 386-394.

[41] Rossi, S., F. Deflorian, and F. Venturini, *Improvement of surface finishing and corrosion resistance of prototypes produced by direct metal laser sintering.* Journal of Materials Processing Technology, 2004. **148**(3): p. 301-309.

[42] Yu, W. and J. Bergström, *Fatigue and microstructure of iron based sintered alloys.* Journal of Iron and Steel Research, International, 2007. **14**(5): p. 137-141.

[43] Wang, Y., J. Bergström, and C. Burman, *Thermal fatigue behavior of an iron-based laser sintered material.* Materials Science and Engineering: A, 2009. **513-514**: p. 64-71.

[44] Song, B., et al., *Fabrication and microstructure characterization of selective laser-melted FeAl intermetallic parts.* Surface and Coatings Technology, 2012. **206**(22): p. 4704-4709.

[45] Rolink, G., et al., *Laser metal deposition and selective laser melting of Fe–28 at.% Al.* Journal of Materials Research, 2014. **29**(17): p. 2036-2043.

[46] Guan, K., et al., *Effects of processing parameters on tensile properties of selective laser melted 304 stainless steel.* Materials & Design, 2013. **50**: p. 581-586.

[47] Abd-Elghany, K. and D.L. Bourell, *Property evaluation of 304L stainless steel fabricated by selective laser melting.* Rapid Prototyping Journal, 2012. **18**(5): p. 420-428.

[48] Childs, T.H.C., C. Hauser, and M. Badrossamay, *Selective laser sintering (melting) of stainless and tool steel powders: experiments and modelling.* Proceedings of the Institution of Mechanical Engineers, Part B: Journal of Engineering Manufacture, 2005. **219**(4): p. 339-357.

[49] Jandin, G., et al. *Manufacture of stainless steel parts by selective laser melting process*. in *2nd International Conference on Advanced Research in Virtual and Rapid Prototyping*. 2005. CRC Press.

[50] Wehmöller, M., et al., *Implant design and production - a new approach by selective laser melting*, in *International Congress Series*. 2005. p. 690-695.

[51] Brandner, J.J., et al. *Microstructure devices generation by selective laser melting*. in *SPIE LASE*. 2007. International Society for Optics and Photonics.

[52] Wong, M., et al., *Selective laser melting of heat transfer devices.* Rapid Prototyping Journal, 2007. **13**(5): p. 291-297.

[53] Tolosa, I., et al., *Study of mechanical properties of AISI 316 stainless steel processed by "selective laser melting", following different manufacturing strategies.* The International Journal of Advanced Manufacturing Technology, 2010. **51**(5-8): p. 639-647.

[54] Bertrand, P. and I. Smurov. *Laser assisted direct manufacturing*. in *International Conference on Lasers, Applications, and Technologies' 07*. 2007. International Society for Optics and Photonics.

[55] Simchi, A. and H. Asgharzadeh, *Densification and microstructural evaluation during laser sintering of M2 high speed steel powder.* Materials Science and Technology, 2004. **20**(11): p. 1462-1468.

[56] Wright, C.S., et al. *Selective laser melting of prealloyed high alloy steel powder beds*. in *Materials science forum*. 2006. Trans Tech Publications.

[57] Milovanovic, J., M. Stojkovic, and M. Trajanovic, *Rapid tooling of tyre tread ring mould using direct metal laser sintering.* Journal of Scientific & Industrial Research, 2009. **68**(12): p. 1038-1042.

[58] Feuerhahn, F., et al., *Microstructure and Properties of Selective Laser Melted High Hardness Tool Steel.* Physics Procedia, 2013. **41**: p. 843-848.

[59] Taha, M.A., et al., *On selective laser melting of ultra high carbon steel: Effect of scan speed and post heat treatment.* Materialwissenschaft und Werkstofftechnik, 2012. **43**(11): p. 913-923.

[60] Averyanova, M. and P. Bertrand, *Direct Manufacturing of dense parts from martensitic precipitation hardening steel gas atomized powder by Selective Laser Melting (SLM) technology*. Innovative Developments in Design and Manufacturing: Advanced Research in Virtual and Rapid Prototyping, ed. P.J.D. Bartolo, et al. 2010. 343-348.

[61] Facchini, L., et al., *Ductility of a Ti-6Al-4V alloy produced by selective laser melting of prealloyed powders.* Rapid Prototyping Journal, 2010. **16**(6): p. 450-459.

[62] Rafi, H.K., T.L. Starr, and B.E. Stucker, *A comparison of the tensile, fatigue, and fracture behavior of Ti–6Al–4V and 15-5 PH stainless steel parts made by selective laser melting.* The International Journal of Advanced Manufacturing Technology, 2013. **69**(5-8): p. 1299-1309.

[63] Stanford, M., et al. *An investigation into fully melting a maraging steel using direct laser sintering*. in *Metal forming conference*. 2008.

[64] Casavola, C., S.L. Campanelli, and C. Pappalettere, *Preliminary investigation on distribution of residual stress generated by the selective laser melting process.* The Journal of Strain Analysis for Engineering Design, 2009. **44**(1): p. 93-104.

[65] Osakada, K. and M. Shiomi, *Flexible manufacturing of metallic products by selective laser melting of powder.* International Journal of Machine Tools and Manufacture, 2006. **46**(11): p. 1188-1193.

[66] Kim, T.B., et al., *Additive manufactured porous titanium structures: Through-process quantification of pore and strut networks.* Journal of Materials Processing Technology, 2014. **214**(11): p. 2706-2715.

[67] Zhang, Z., et al., *Hierarchical tailoring of strut architecture to control permeability of additive manufactured titanium implants.* Mater Sci Eng C Mater Biol Appl, 2013. **33**(7): p. 4055-62.

[68] Gu, D., et al., *Densification behavior, microstructure evolution, and wear performance of selective laser melting processed commercially pure titanium.* Acta Materialia, 2012. **60**(9): p. 3849-3860.

[69] Zhang, S., et al., *Effects of scan line spacing on pore characteristics and mechanical properties of porous Ti6Al4V implants fabricated by selective laser melting.* Materials & Design, 2014. **63**: p. 185-193.

[70] Challis, V.J., et al., *High specific strength and stiffness structures produced using selective laser melting.* Materials & Design, 2014. **63**: p. 783-788.

[71] Vandenbroucke, B. and J.P. Kruth, *Selective laser melting of biocompatible metals for rapid manufacturing of medical parts.* Rapid Prototyping Journal, 2007. **13**(4): p. 196-203.

[72] Szymczyk, P., et al., *The ability of S.aureus to form biofilm on the Ti-6Al-7Nb scaffolds produced by Selective Laser Melting and subjected to the different types of surface modifications.* Acta of Bioengineering and Biomechanics, 2013. **15**(1): p. 69-76.

[73] Marcu, T., et al., *Selective laser melting of Ti6Al7Nb with hydroxyapatite addition.* Rapid Prototyping Journal, 2014. **20**(4): p. 301-310.

[74] Dybala, B., E. Chlebus, and Asme, *TITANIUM SCAFFOLDS FOR CUSTOM CMF RESTORATIONS*. Proceedings of the Asme/Iscie International Symposium on Flexible Automation, Isfa 2012. 2013, New York: Amer Soc Mechanical Engineers. 517-520.

[75] Chlebus, E., et al., *Microstructure and mechanical behaviour of Ti—6Al—7Nb alloy produced by selective laser melting.* Materials Characterization, 2011. **62**(5): p. 488-495.

[76] Speirs, M., et al., *The Effect of Pore Geometry on the Mechanical Properties of Selective Laser Melted Ti-13Nb-13Zr Scaffolds.* Procedia CIRP, 2013. **5**: p. 79-82.

[77] Zhang, L.C. and T.B. Sercombe. *Selective Laser Melting of Low-Modulus Biomedical Ti-24Nb-4Zr-8Sn Alloy: Effect of Laser Point Distance*. in *Key Engineering Materials*. 2012. Trans Tech Publications.

[78] Zhang, L.C., et al., *Manufacture by selective laser melting and mechanical behavior of a biomedical Ti–24Nb–4Zr–8Sn alloy.* Scripta Materialia, 2011. **65**(1): p. 21-24.

[79] Zieliński, A., et al. *Materials design for the titanium scaffold based implant*. in *Solid State Phenomena*. 2012. Trans Tech Publications.

[80] Abe, F., et al., *The manufacturing of hard tools from metallic powders by selective laser melting.* Journal of materials processing technology, 2001. **111**(1): p. 210-213.

[81] Yadroitsev, I. and I. Smurov, *Selective laser melting technology: From the single laser melted track stability to 3D parts of complex shape.* Physics Procedia, 2010. **5**: p. 551-560.

[82] Das, S., et al., *Direct laser freeform fabrication of high performance metal components.* Rapid Prototyping Journal, 1998. **4**(3): p. 112-117.

[83] Wang, Z., et al., *The microstructure and mechanical properties of deposited-IN718 by selective laser melting.* Journal of Alloys and Compounds, 2012. **513**: p. 518-523.

[84] Amato, K.N., et al., *Microstructures and mechanical behavior of Inconel 718 fabricated by selective laser melting.* Acta Materialia, 2012. **60**(5): p. 2229-2239.

[85] Kelbassa, I., et al. *Manufacture and repair of aero engine components using laser technology*. in *Proceedings of the 3rd Pacific International Conference on Application of Lasers and Optics*. 2008. Beijing, China: Laser Insitute of America.

[86] Rickenbacher, L., et al., *High temperature material properties of IN738LC processed by selective laser melting (SLM) technology.* Rapid Prototyping Journal, 2013. **19**(4): p. 282-290.

[87] Tomus, D., et al., *Controlling the Microstructure of Hastelloy-X Components Manufactured by Selective Laser Melting.* Physics Procedia, 2013. **41**: p. 823-827.

[88] Wang, F., *Mechanical property study on rapid additive layer manufacture Hastelloy® X alloy by selective laser melting technology.* The International Journal of Advanced Manufacturing Technology, 2011. **58**(5-8): p. 545-551.

[89] Wang, F., X.H. Wu, and D. Clark, *On direct laser deposited Hastelloy X: dimension, surface finish, microstructure and mechanical properties.* Materials Science and Technology, 2011. **27**(1): p. 344-356.

[90] Vilaro, T., et al., *Microstructural and mechanical approaches of the selective laser melting process applied to a nickel-base superalloy.* Materials Science and Engineering: A, 2012. **534**: p. 446-451.

[91] Hagedorn, Y.C., et al., *Processing of nickel based superalloy MAR M-247 by means of High Temperature - Selective Laser Melting (HT - SLM).* High Value Manufacturing: Advanced Research in Virtual and Rapid Prototyping, 2014: p. 291-295.

[92] Carter, L.N., et al., *The influence of the laser scan strategy on grain structure and cracking behaviour in SLM powder-bed fabricated nickel superalloy.* Journal of Alloys and Compounds, 2014. **615**: p. 338-347.

[93] Speirs, M., et al., *The effect of SLM parameters on geometrical characteristics of open porous NiTi scaffolds.* High Value Manufacturing: Advanced Research in Virtual and Rapid Prototyping, 2014: p. 309-314.

[94] Dadbakhsh, S., et al., *Effect of SLM Parameters on Transformation Temperatures of Shape Memory Nickel Titanium Parts.* Advanced Engineering Materials, 2014. **16**(9): p. 1140-1146.

[95] Habijan, T., et al., *The biocompatibility of dense and porous Nickel-Titanium produced by selective laser melting.* Mater Sci Eng C Mater Biol Appl, 2013. **33**(1): p. 419-26.

[96] Olakanmi, E.O., *Selective laser sintering/melting (SLS/SLM) of pure Al, Al–Mg, and Al–Si powders: Effect of processing conditions and powder properties.* Journal of Materials Processing Technology, 2013. **213**(8): p. 1387-1405.

[97] Savalani, M.M., et al. *Selective Laser Melting of Aluminium and its Alloys*. in *NZ RAPID PRODUCT DEVELOPMENT CONFERENCE*. 2011. AUCKLAND UNIVERSITY OF TECHNOLOGY, AUCKLAND, NEW ZEALAND.

[98] Jerrard, P.G.E., et al. *Consolidation behaviour and microstructure characteristics of pure aluminium and alloy powders following Selective Laser Melting processing*. in *36th International MATADOR Conference*. 2010. Manchester, Lancashire, United Kingdom: Springer.

[99] Louvis, E., P. Fox, and C.J. Sutcliffe, *Selective laser melting of aluminium components.* Journal of Materials Processing Technology, 2011. **211**(2): p. 275-284.

[100] Li, Y. and D. Gu, *Parametric analysis of thermal behavior during selective laser melting additive manufacturing of aluminum alloy powder.* Materials & Design, 2014. **63**: p. 856-867.

[101] Thijs, L., et al., *Fine-structured aluminium products with controllable texture by selective laser melting of pre-alloyed AlSi10Mg powder.* Acta Materialia, 2013. **61**(5): p. 1809-1819.

[102] Manfredi, D., et al., *From Powders to Dense Metal Parts: Characterization of a Commercial AlSiMg Alloy Processed through Direct Metal Laser Sintering.* Materials, 2013. **6**(3): p. 856-869.

[103] Buchbinder, D., et al., *High Power Selective Laser Melting (HP SLM) of Aluminum Parts.* Physics Procedia, 2011. **12**: p. 271-278.

[104] Pogson, S., P. Fox, and W. O'Neill. *The effect of varying laser scanning speed on DMLR processed metal parts*. in *Fourth National Conference on Rapid and Virtual Prototyping and Applications*. 2003. Lancaster, United Kingdom: Professional Engineering Publications.

[105] Pogson, S.R., et al., *The production of copper parts using DMLR.* Rapid Prototyping Journal, 2003. **9**(5): p. 334-343.

[106] Zhang, D.Q., Z.H. Liu, and C.K. Chua. *Investigation on forming process of copper alloys via Selective Laser Melting*. in *6th International Conference on Advanced Research in Virtual and Rapid Prototyping*. 2013. Leiria, Portugal: CRC Press.

[107] Zhang, D.Q., et al. *Selective Laser Melting: On the Study of Microstructure of K220*. in *1st International Conference on Progress in Additive Manufacturing*. 2014. Singapore: Research Publishing.

[108] Gargarella, P., et al., *Phase Formation, Thermal Stability and Mechanical Properties of a Cu-Al-Ni-Mn Shape Memory Alloy Prepared by Selective Laser Melting.* Materials Research, 2015. **18**: p. 35-38.

[109] Savalani, M., C. Ng, and H. Man. *Selective Laser Melting of Magnesium for Future Applications in Medicine*. in *Manufacturing Automation (ICMA), 2010 International Conference on*. 2010. IEEE.

[110] Ng, C.C., et al., *Microstructure and mechanical properties of selective laser melted magnesium.* Applied Surface Science, 2011. **257**(17): p. 7447-7454.

[111] Zhang, B., H. Liao, and C. Coddet, *Effects of processing parameters on properties of selective laser melting Mg–9%Al powder mixture.* Materials & Design, 2012. **34**: p. 753-758.

[112] Ayyildiz, S., et al., *Annealing of Co-Cr dental alloy: effects on nanostructure and Rockwell hardness.* J Adv Prosthodont, 2013. **5**(4): p. 471-8.

[113] Kim, K.B., et al., *An evaluation of marginal fit of three-unit fixed dental prostheses fabricated by direct metal laser sintering system.* Dent Mater, 2013. **29**(7): p. e91-6.

[114] Sanz, C. and V. García Navas, *Structural integrity of direct metal laser sintered parts subjected to thermal and finishing treatments.* Journal of Materials Processing Technology, 2013. **213**(12): p. 2126-2136.

[115] Zhang, D., Q. Cai, and J. Liu, *Formation of Nanocrystalline Tungsten by Selective Laser Melting of Tungsten Powder*. Materials and Manufacturing Processes, 2012. **27**(12): p. 1267-1270.

[116] Deprez, K., et al., *Rapid additive manufacturing of MR compatible multipinhole collimators with selective laser melting of tungsten powder.* Med Phys, 2013. **40**(1): p. 012501.

[117] Zhang, D., et al., *Research on Process and Microstructure Formation of W-Ni-Fe Alloy Fabricated by Selective Laser Melting.* Journal of Materials Engineering and Performance, 2010. **20**(6): p. 1049-1054.

[118] Zhang, D.Q., et al., *Select laser melting of W–Ni–Fe powders: simulation and experimental study.* The International Journal of Advanced Manufacturing Technology, 2010. **51**(5-8): p. 649-658.

[119] Zhang, D., et al., *Microstructural evolvement and formation of selective laser melting W–Ni–Cu composite powder.* The International Journal of Advanced Manufacturing Technology, 2012. **67**(9-12): p. 2233-2242.

[120] Khan, M. and P. Dickens, *Selective Laser Melting (SLM) of pure gold.* Gold Bulletin, 2010. **43**(2): p. 114-121.

[121] Jhabvala, J., E. Boillat, and R. Glardon, *On the use of EBSD analysis to investigate the microstructure of gold samples built by selective laser melting.* Gold Bulletin, 2011. **44**(2): p. 113-118.

[122] Gebhardt, A., et al. *Numerical and Experimental Investigation of Selective Laser Melting of Silver*. in *Fraunhofer Direct Digital Manufacturing Conference (DDMC), Berlin*. 2012.

[123] Fateri, M., J.-S. Hötter, and A. Gebhardt, *Experimental and Theoretical Investigation of Buckling Deformation of Fabricated Objects by Selective Laser Melting.* Physics Procedia, 2012. **39**: p. 464-470.

[124] Thijs, L., et al., *Strong morphological and crystallographic texture and resulting yield strength anisotropy in selective laser melted tantalum.* Acta Materialia, 2013. **61**(12): p. 4657-4668.

[125] Li, X.P., et al., *The role of a low-energy–density re-scan in fabricating crack-free Al85Ni5Y6Co2Fe2 bulk metallic glass composites via selective laser melting.* Materials & Design, 2014. **63**: p. 407-411.

[126] Jerrard, P.G.E., L. Hao, and K.E. Evans, *Experimental investigation into selective laser melting of austenitic and martensitic stainless steel powder mixtures.* Proceedings of the Institution of Mechanical Engineers, Part B: Journal of Engineering Manufacture, 2009. **223**(11): p. 1409-1416.

[127] Yasa, E., J. Deckers, and J.-P. Kruth, *The investigation of the influence of laser re-melting on density, surface quality and microstructure of selective laser melting parts.* Rapid Prototyping Journal, 2011. **17**(5): p. 312-327.

[128] Sing, S.L., et al., *Interfacial characterization of SLM parts in multi-material processing: Intermetallic phase formation between AlSi10Mg and C18400 copper alloy.* Materials Characterization, 2015. **107**: p. 220-227.

[129] Liu, Z.H., et al., *Interfacial characterization of SLM parts in multi-material processing: Metallurgical diffusion between 316L stainless steel and C18400 copper alloy.* Materials Characterization, 2014. **94**: p. 116-125.

[130] Gu, D., Y. Shen, and Z. Lu, *Preparation of TiN–Ti5Si3 in-situ composites by Selective Laser Melting.* Materials Letters, 2009. **63**(18-19): p. 1577-1579.

[131] Woo, H. and H. Cho, *Three-dimensional temperature distribution in laser surface hardening processes.* Proceedings of the Institution of

Mechanical Engineers, Part B: Journal of Engineering Manufacture, 1999. **213**(7): p. 695-712.

[132] Araya, G. and G. Gutierrez, *Analytical solution for a transient, three-dimensional temperature distribution due to a moving laser beam.* International Journal of Heat and Mass Transfer, 2006. **49**(21-22): p. 4124-4131.

[133] Majumdar, P. and H. Xia, *A Green's function model for the analysis of laser heating of materials.* Applied Mathematical Modelling, 2007. **31**(6): p. 1186-1200.

[134] Gusarov, A., et al., *Contact thermal conductivity of a powder bed in selective laser sintering.* International Journal of Heat and Mass Transfer, 2003. **46**(6): p. 1103-1109.

[135] Alkahari, M.R., et al. *Thermal conductivity of metal powder and consolidated material fabricated via selective laser melting*. in *Key Engineering Materials*. 2012. Trans Tech Publ.

[136] Matsumoto, M., et al., *Finite element analysis of single layer forming on metallic powder bed in rapid prototyping by selective laser processing.* International Journal of Machine Tools and Manufacture, 2002. **42**(1): p. 61-67.

[137] Li, J.F., L. Li, and F.H. Stott, *A three-dimensional numerical model for a convection–diffusion phase change process during laser melting of ceramic materials.* International Journal of Heat and Mass Transfer, 2004. **47**(25): p. 5523-5539.

[138] Dai, K. and L. Shaw, *Finite element analysis of the effect of volume shrinkage during laser densification.* Acta Materialia, 2005. **53**(18): p. 4743-4754.

[139] Safdar, S., L. Li, and M.A. Sheikh, *Numerical analysis of the effects of non-conventional laser beam geometries during laser melting of metallic materials.* Journal of Physics D: Applied Physics, 2007. **40**(2): p. 593-603.

[140] Dai, D. and D. Gu, *Tailoring surface quality through mass and momentum transfer modeling using a volume of fluid method in selective laser melting of TiC/AlSi10Mg powder.* International Journal of Machine Tools and Manufacture, 2015. **88**: p. 95-107.

[141] Li, J.F., L. Li, and F.H. Stott, *Comparison of volumetric and surface heating sources in the modeling of laser melting of ceramic materials.* International Journal of Heat and Mass Transfer, 2004. **47**(6-7): p. 1159-1174.

[142] Kovaleva, I.O., S.N. Grigoriev, and A.V. Gusarov, *Non-disturbing Boundary Conditions for Modeling of Laser Material Processing.* Physics Procedia, 2014. **56**: p. 421-428.

[143] Zeng, K., et al., *Comparison of 3DSIM thermal modelling of selective laser melting using new dynamic meshing method to ANSYS.* Materials Science and Technology, 2015. **31**(8): p. 945-956.

[144] Kovaleva, I., O. Kovalev, and I. Smurov, *Model of Heat and Mass Transfer in Random Packing Layer of Powder Particles in Selective Laser Melting*. Physics Procedia, 2014. **56**: p. 400-410.

# Chapter 3

# Experimental Methodology and Modelling

*From the previous chapter, reviewing publications on the research of SLM has provided some information on the process parameters of SLM for different materials. However, the links between optimized process parameters to material properties have not been established despite attempts at numerical modelling and computer simulation. In this chapter, information on process parameters is collected from both literature and earlier experiments conducted by the Singapore Centre for 3D Printing (SC3DP), which increases the amount and data and allow for a trend to be established.*

*This chapter also shows the development of a novel model which displays the relationship between optimized process parameters for near-full density parts and material properties. Assumptions made in the model and their implications are also discussed in this chapter. By inserting the data into our model, the energy requirement of the SLM process is observed to vary with the thermal conductivity of the processed material. However, more information is required to obtain an indicative trend for this empirical relationship. Hence, parameter optimization studies were required for materials with thermal conductivities ranging between 50 W/m·K to 100 W/m·K.*

*In the parameter optimization studies, laser power, scanning speed, hatch spacing and layer thickness were the parameters examined. The density of SLM samples was determined through the application of Archimedes' principle. Near full density SLM samples were then examined by X-ray diffraction and microscopy to determine the crystallographic phases and microstructure respectively. Some fundamentals of these techniques will be introduced.*

This section published substantially as:
C.Y. Yap, C.K. Chua, and Z.L. Dong, *An effective analytical model of selective laser melting*. **Virtual and Physical Prototyping**, 2016: p. 1-6.

## 3.1 Rationale for Selection of Methods

In developing a semi-empirical model for SLM, data has to be collected on the process parameters, the wavelength of the laser used in the process, thermal properties of the materials and their densities. Data is collected from literature concerning the parameter optimization studies for different materials for the SLM process and through conducting such experiments and synthesizing near full density samples.

Samples synthesized via the SLM process had to be tested for their density and determined how the SLM sample measures up to the theoretical density of the material. Moreover, the samples have to be characterized via X-Ray Diffraction (XRD) and microscopy techniques to help determine the presence of impurities, microstructure, phases and crystal orientation. The study of microstructure will aid in the understanding of material properties for SLM fabricated components.

## 3.2 Data Collection

First literature concerning the SLM process dated back to the ’90s. As industrial interest picked up in recent years [1], the number of journal publications has increased significantly [2]. The data required from the literature will include the relative density achieved for the SLM samples and the corresponding process parameters such as laseAl 4046r wavelength, laser power, scanning speed, hatch spacing, and layer thickness. Continuous wave laser is considered in this Ph.D. work over pulsed lasers as it is the prevalent laser system deployed in the state-of-the-art SLM machines.

Moreover, the samples have to achieve relative densities higher than 98 % to be considered near full density. Density and thermal properties of materials such as elements and common alloys were referred from ASM Handbooks Online™ unless stated otherwise. The benchmark of 98 % was chosen due to the compound uncertainty in the calculation of density. The following formula was used:

$$density\ of\ object = density\ of\ fluid\ * (\frac{weight}{weight\ - immersed\ weight})$$

There is a 0.5 % uncertainty in the density of fluid due to fluctuations in the ambient temperature and a ± 0.01 g uncertainty in the measurements of the weight (in air) and immersed weight (in fluid) of the samples. These factors contribute to a compound uncertainty of 2 % in the calculation of density. Hence, an object with a calculated relative density of 98 % can be considered near-full density.

Data can also be collected via experiments carried out at Singapore Centre for 3D Printing (SC3DP). Data from these experiments will serve to overwrite data from existing literature for the same material if the energy required to achieve the same relative density is found to be lower. This ensures that the most energy efficient process parameters are selected in the data.

### 3.2.1 Data Collection via Literature

Most published papers do not reveal the full set of process parameters that were used in their studies. However, some share these details. The parameters detailed in these publications are tallied in Table 3.1. Some materials such as AlSi10Mg were reported in different publications by different research groups [3, 4]. In such cases, the parameters that have a lower volumetric energy density (VED) are selected. VED is given by $\frac{P}{v \cdot h \cdot t}$ and has a unit of J/mm$^3$ and it is a useful indication of the amount of energy invested for the fabrication of a particular material with SLM.

Table 3.1 Selected SLM process parameters published in scientific literature.

| Material | Process parameters | | | | Relative Density (%) | Reference |
|---|---|---|---|---|---|---|
| | P (W) | v (mm/s) | h (mm) | t (mm) | | |
| 316L stainless steel | 104 | 550 | 0.13 | 0.03 | 98.0 | [5] |
| CP Ti | 90 | 300 | 0.05 | 0.05 | 99.5 | [6] |
| Ti6Al4V | 42 | 200 | 0.1 | 0.03 | 98.5 | [7] |
| Hastelloy X | 195 | 1000 | 0.09 | 0.02 | 99.75 | [8] |
| AlSi10Mg | 190 | 1600 | 0.105 | 0.03 | 98.9 | [4] |
| K220 | 350 | 530 | 0.09 | 0.03 | 99.9 | [9] |

### 3.2.2 Experimental Data Collection

There is also some studies done in SC3DP on the parameter optimization of SLM for different materials. Results from these experiments supersede the information collected from literature survey for SLM of the same material.

Table 3.2 Results from process optimization studies carried out in SC3DP.

| Material | Process parameters | | | | Relative Density (%) |
|---|---|---|---|---|---|
| | P (W) | v (mm/s) | h (mm) | t (mm) | |
| 316L stainless steel | 360 | 1635 | 0.05 | 0.05 | 98.1 |
| AlSi10Mg | 350 | 1170 | 0.17 | 0.05 | 99.1 |
| CoCr | 360 | 500 | 0.25 | 0.05 | 98.1 |
| Ti6Al4V | 63 | 300 | 0.075 | 0.05 | 98.4 |
| CP Ti | 240 | 1200 | 0.125 | 0.05 | 98.7 |
| Inconel 718 | 300 | 900 | 0.15 | 0.05 | 98.5 |

## 3.3 Modelling

In addition to experimenting with SLM of different materials, researchers have also tried to better our understanding of this AM process by modelling and carrying out numerical analysis. However, the simulation of powder-liquid-solid transition and the dynamics involved has remained a challenge.

Moreover, there is also a lack of an analytical or empirical model for the SLM process. As a result, whenever new materials are explored for fabrication via

SLM, the optimal process parameters are often achieved only after multiple rounds of trial and error. The common steps involve (1) single track melting, to find the combination of laser power and scanning speed, or the linear energy density, for a stable melt track [10], (2) selection of appropriate layer thickness [11] and finally (3) selection of optimal parameters by adjusting laser power, scanning speed and hatch spacing in a multitude of combinations. Hence, a new semi-empirical model of SLM has been proposed by investigating the energy requirement of the process.

### 3.3.1 Development of Model

The semi-empirical model is based on the conservation of energy and the energy required to melt the material. For powders to be fully melted by the laser:

$$\iiint dxdydz \cdot \rho_{powder} \cdot \left(\int c_s dT + L\right) \leq E_{abs} \qquad (1)$$

where $\rho_{powder}$ accounts for the density of the material and apparent density of powders during the SLM process, $c_s$ is the temperature dependent specific heat capacity of the solid, $\int c_s dT$ accounts for the heat capacity from the starting temperature of the material to its melting temperature, $L$ represents the latent heat of fusion and $E_{abs}$ is energy absorbed from the laser.

Powders commonly used in SLM have exhibited an apparent density of 50 % [12], hence $\rho_{powder}$ can be substituted by half of the density of the bulk material. Cross-sectional area of single melt tracks can be the basis for consideration when defining the volume in the equation. Studies have shown that single melt tracks produced during SLM have near semi-circular cross-sections [13]. Therefore, the process can be simplified as the joining of overlapping stripes with semi-circular cross-sections as illustrated in Figure 3.1.

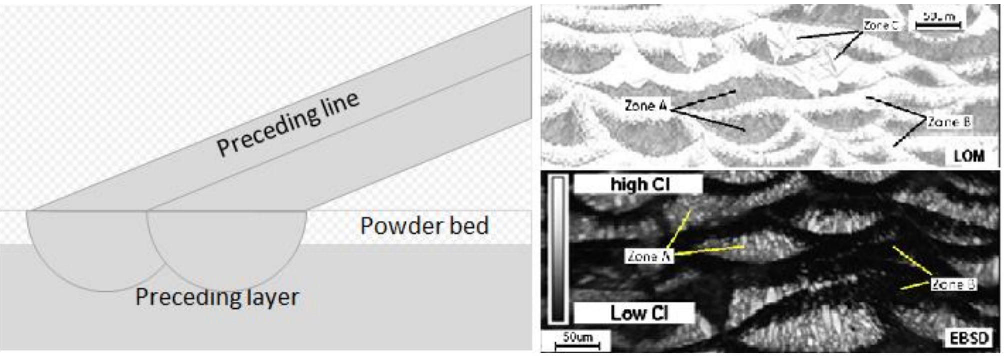
Preceding line
Powder bed
Preceding layer
Zone C
50um
Zone A
Zone B
LOM
high CI
Zone A
Zone B
Low CI
50um
EBSD

Figure 3.1 Simplification of melt tracks as overlapping semi-circular stripes (left) and melt profile of SLM M2 steel on XZ plane through light microscopy and electron backscatter diffraction (right) [13].

In the SLM process, laser power (*P*), scanning speed (*v*), hatch spacing (*h*) and layer thickness (*t*) are the parameters commonly adjusted to optimize the process for a particular material. Laser power refers to the power of a continuous wave laser. Currently, continuous wave fibre lasers are the most commonly used laser systems, adapted by major machine providers. Laser power and scanning speed determine the instantaneous power input into the powder bed. Hatch spacing, also known as scan spacing in some literature, is the distance between the centre lines of two neighbouring melt vectors. Hatch spacing and layer thickness are illustrated in Figure 3.2.

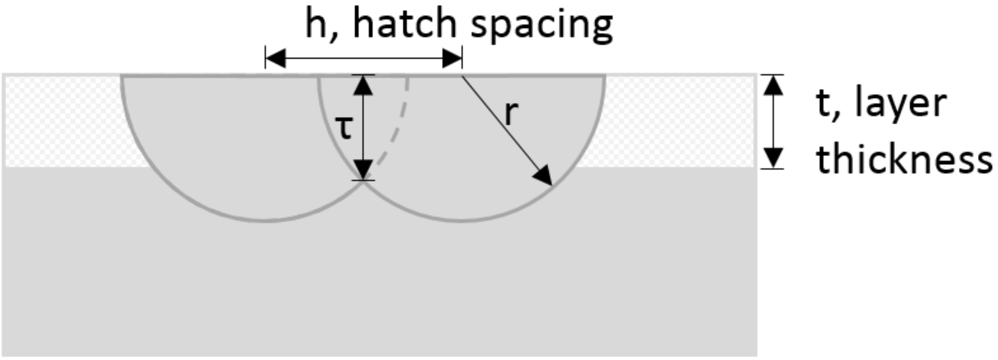
h, hatch spacing
τ
r
t, layer thickness

Figure 3.2 Illustration of hatch spacing and layer thickness. Melt pools are modelled to have semi-circular cross sections with radius (r) and overlapping height (τ) between two neighbouring melt tracks [14].

For parts to have full density, the layer thickness must be equal to or smaller than the overlapping height, τ. Thus, the characteristic radius of the cross section can be expressed in *t* and *h*:

$$r^2 = t^2 + \frac{h^2}{4} \qquad (2)$$

Laser power (*P*) and scanning speed (*v*) can then be incorporated into the energy equation to account for the volume and the energy absorbed during the process:

$$v \cdot \frac{1}{2}\pi(t^2 + \frac{h^2}{4}) \cdot \frac{1}{2}\rho_{material} \cdot (\int c_s dT + L) \;=\; \alpha_\lambda \cdot P \qquad (3)$$

where $\alpha_\lambda$ is the absorptance of the material to the laser irradiation of wavelength, λ. Absorptance is defined as the fraction of radiant flux absorbed by the material over the radiant flux the material received at a wavelength. The product of scanning velocity, area and density gives the mass build-up rate of the process, and multiplying this by the specific thermal energy gives the energy requirement to bring the mass from solid at room temperature to liquid at melting point. This equation relates the SLM process parameters and material properties.

For the calculation of heat capacity, $\int c_s dT$ can be simplified to $c_{r.t.}\Delta T$ where $c_{r.t.}$ is the specific heat capacity of the material at room temperature and $\Delta T$ is the temperature change from the resting temperature of the process to the melting point or liquidus temperature of the material. Latent heat of fusion, $L$, will only be considered for pure metals and eutectic alloys.

### 3.3.2 Assumptions in the Semi-Empirical Model

The development of this semi-empirical model is based on several important assumptions and they are listed as such:

(1) Heat loss to the surrounding was neglected in the calculation. Some of the heat supplied to create a melt track by the laser are lost to neighbouring powders, preceding melt tracks, previous layers and the substrate plates by conduction. Badrossamay and Childs postulated that the conduction mode accounts for the majority of the heat loss and this heat loss is more significant at low processing speeds [15]. Heat could also be lost in the chamber by convection of the flowing air above the melt pool and radiation.

(2) The cross-sections of the melt tracks are semi-circular and uniform throughout. However, the shape of the melt tracks is determined mainly by the energy profile of the processing laser as shown from the work of Loh et al.. Lasers with Gaussian beam profile often create deep melt penetration and a narrow melt width while lasers with uniform beam profile create a more shallow penetration and a broad melt width. The Gaussian beam laser gave a width to depth ratio between 3 to 5 and uniform beam laser gave a width to depth ratio between 10 to 20 [13]. Moreover, the melted volume at the beginning and end of each melt tracks are not accounted for in the model. This leads to inaccuracy and underestimation of the energy required for the melting of powder materials.

(3) The specific heat capacity values of the materials were taken at room temperature in the calculation and this material property was taken to be constant and temperature-independent. Specific heats of materials generally increase with temperature. This leads to lower calculated values for the energy required especially for materials with very high melting temperatures.

(4) The absorptance of the powder to laser irradiation was taken to be the same as the corresponding bulk material. However, studies have shown that absorptance of powder material to irradiation can be significantly higher than that of the corresponding bulk material, and the difference is greater for reflective materials such as aluminium. For instance, at a wavelength of 1.06

μm, the absorptance of titanium bulk material is 30 % [16], while that of titanium powder is 77 % [17], resulting in a 156 % increase in energy absorbed from the laser. This effect is more significant for reflective materials such as copper alloys and aluminium alloys.

(5) During the SLM process, the powder may be laid in an uneven manner for some of the materials. Obtaining an even and thin layer of powder for each layer can be a challenge for the SLM process and this is affected by the flowability of the powder. Uneven coating of powder causes variation in the apparent density of the powder and the mass of material processed by the laser at every layer.

(6) Small hatch spacing values could lead to under-evaluation of the energy requirement as a small h will result in a small characteristic radius in the new semi-empirical model, giving an under-evaluation of the melt pool volume and consequent energy requirement. In reality, small hatch spacing would result in high degree of overlapping in the melt pools and between layers. This results in high degree of re-melting and energy wastage in the process.

(7) For each material, there exists an envelope of process parameters within which near-full density parts can be achieved. However, not all of these combinations provide the most energy-efficient route for the SLM process. For instance, the relative density of 98 % for SLM of nickel can be achieved by VED from 120 J/mm$^3$ to 200 J/mm$^3$. It is possible that the reported optimized parameters in literature may not be the lowest volumetric energy density to achieve near full density parts.

Given the numerous assumption of the semi-empirical model, there are discrepancies between the calculated energy required for difference materials and the energy supplied by the optimized parameters derived from experiments.

In order to account for the discrepancy, a compensation factor $\beta$ is included in the equation to account for the empirical relationship:

$$\beta\left[v \cdot \frac{1}{2}\pi(t^2 + \frac{h^2}{4}) \cdot \frac{1}{2}\rho_{material} \cdot (\int c_s dT + L)\right] = \alpha_\lambda \cdot P \qquad (4)$$

$\beta$ is a dimensionless number that gives the ratio of the actual power supplied to the powder over the calculated power requirement to achieve near full density parts via melting of the powder material with laser. A breakdown of the parameters and their corresponding units are given in Table 3.3.

Table 3.3 Description of parameters and the corresponding units in Equation (4).

| Parameter | Description | Unit |
|---|---|---|
| $P$ | Laser power | W |
| $v$ | Scanning speed | mm/s |
| $h$ | Hatch spacing | mm |
| $t$ | Laser thickness | mm |
| $\rho_{material}$ | Density of material | g/mm$^3$ |
| $c_s$ | Specific heat capacity | J/g·K |
| $T$ | Temperature | K |
| $L$ | Specific latent heat | J/g |
| $\alpha_\lambda$ | Material absorptance to wavelength λ | - |
| $\beta$ | Compensation factor | - |

By factoring in the process parameters according to Table 3.1 and Table 3.2, and eliminating the parameters with higher energy usage for the same material, a plot of $\beta$ against thermal conductivity of the material, at room temperature, is created (Figure 3.3).

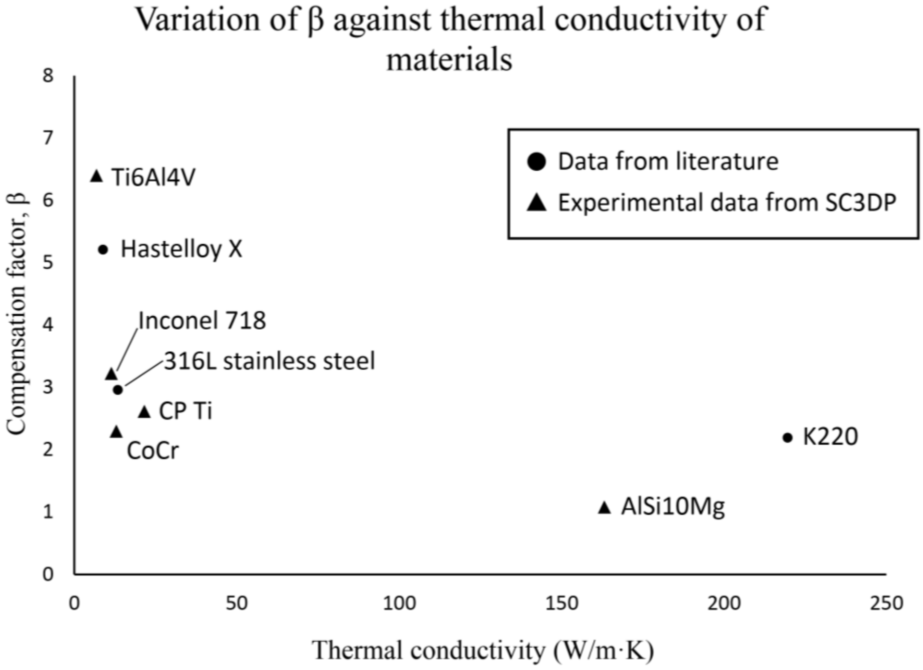

Figure 3.3 Plot of compensation factor against thermal conductivity of the respective material. The data is compiled via literature survey and experiments conducted in other research projects in SC3DP.

From 5 W/m·K to 25 W/m·K, the compensation factor decreased sharply with increase in thermal conductivity. At the other side of the spectrum, an increase in thermal conductivity resulted in a relatively gradual increase in the compensation factor. For the data to be more complete, information for materials with thermal conductivities ranging between 50 W/m·K and 100 W/m·K is required. Hence, parameter optimization studies were carried out for nickel (80 W/m·K) and tin (67 W/m·K) to fill in the gap.

## 3.4 Synthesis

In order to verify the optimized parameters for achieving relative densities of 98 % or higher, parameter optimization studies have to be carried out. This section details the principles behind the parameter optimization studies and the method of density measurement.

### 3.4.1 Parameter Optimization – Principles

Parameter optimization studies for the SLM process would involve varying process parameters such as laser power, scanning speed, hatch spacing and layer thickness. These parameters were elaborated in Section 3.3.1.

Laser power, $P$, refers to the energy flux delivered to the surface plane of the powder bed. Conventional off-the-shelf laser modules have an electrical-to-optical conversion efficiency of about 50 %. The rest is usually lost as heat. Studies on the effects of laser power on the SLM process have often coupled with the variation in scanning speed, $v$. Yadroitsev et al showed that the linear energy density, $P/v$, is a determining factor in achieving a stable melt track [10]. Stable melt tracks tend to fall into a particular range of $P/v$ values although the range can be larger for higher laser power.

Hatch spacing, $h$, is defined as the distance between two adjacent melting tracks on the same plane, measured from their centrelines. Careful selection of hatch spacing is essential for achieving good bonding between adjacent melt tracks. Most of the hatch spacing shown in literature correspond to 2 to 5 times that of layer thickness. This coincides with the observation of a width to depth ratio between 3 and 5 for melt tracks formed by Gaussian beam laser [13].

Layer thickness in the SLM process can range from 20 µm to 100 µm. The layer thickness is chosen as a compromise between achieving high resolution in the z-axis, good bonding between layers, good spread of powder during the coating process and the fabrication time. For instance, a smaller layer thickness allows for better resolution and better bonding between layers while powders with poorer flowability will not be able to spread evenly across the powder bed. Fabrication time will also be longer for a smaller layer thickness as there will be more layers to be coated and processed. Layer thicknesses of 30 µm and 50 µm are commonly seen in publications. In the syntheses described in this thesis, a layer thickness of 50 µm is used for all the materials studied. It provides a good balance of processing time and vertical resolution. Moreover, good interlayer bonding can be achieved at this thickness.

For the syntheses carried out in this study, a high laser power of 350 W is used for higher processing efficiency, unless low linear energy density is required. The maximum scanning speed of the SLM process is capped at 3,000 mm/s as recommended by the original equipment manufacturer (OEM). A default layer thickness of 50 µm is used and hatch spacing is ranged between 100 µm to 200 µm, unless otherwise required.

### 3.4.2 Density Measurement – Principles

Density measurement of samples fabricated by SLM is done according to the Archimedes' principle, which describes that in a fluid, an upward buoyant force is exerted on an immersed body and this force is equal to the weight of the fluid that the body displaces. Hence, by taking the difference of the weight of the object in air and in a fluid, the density of the object can be derived if the density of the fluid is known. In the study, each sample is first weighed in air and then weighed again in distilled water. The density of the sample is then calculated as follows:

$$\rho_{sample} = \rho_{fluid} * \left(\frac{m_{air}}{m_{air} - m_{fluid}}\right) \qquad (5)$$

where $\rho_{sample}$ is the density of the SLM sample, $\rho_{fluid}$ is the density of the fluid in which the sample is submerged in for the second weighing, $m_{air}$ refers to the mass of the sample when weighed in air and $m_{fluid}$ refers to the apparent mass of the sample when submerged in fluid. In this simplified formulation, the density of atmospheric air is neglected as it is insignificant as compared to the density of distilled water.

The equipment used in the weighing of the samples is the Mettler Toledo XS204, which has an uncertainty of ± 0.1 mg. Samples were cleaned with ultrasound in ethanol solution for 5 minutes and rinsed in deionized water for 2 minutes. The samples were then placed in dry cabinets for at least 48 hrs. 2-3 drops of Pervitro 75 % were added to the distilled water before measurement. The wetting agent minimizes bubble formation when the sample is submerged in the fluid, increasing the reliability and certainty of measurement.

## 3.5 Characterization

For each material studied, selected samples were characterized by X-ray diffraction (XRD) and microscopy. This section gives a brief introduction to the principles of these characterization techniques and the machines used in this study. Specific analysis of each material will be detailed in the following chapters.

### 3.5.1 X-Ray Diffraction – Principles

XRD is a technique commonly deployed for phase identification of crystalline materials and it can provide information on the dimensions of unit cells. The analysed material can be in powder form or polished surface of a solid. X-ray diffraction is based on constructive interference of monochromatic X-rays through a crystalline sample. X-rays are used because their wavelengths are comparable to inter-atomic spacing. Calculations can be made according to Bragg's Law, $\lambda = 2d \sin \theta$, where $\lambda$ refers to the wavelength of the X-ray, $d$ is the atomic spacing between planes and $\theta$ is the incident angle of the X-ray on to the sample. Figure 3.4 helps to illustrate the variables in Bragg’s Law.

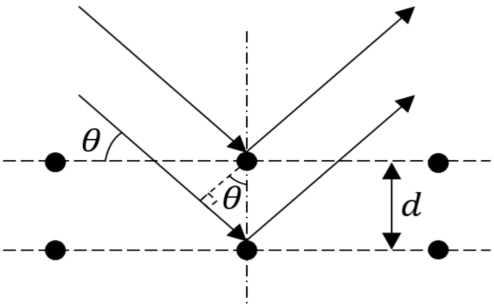

Figure 3.4 Illustration of the relationship between variables in Bragg's law: $n\lambda = 2d\,sin\,\theta$.

This law relates the wavelength of X-ray to the diffraction angle and the lattice spacing in a crystalline sample. The diffracted X-rays are then detected and processed. By scanning the sample through θ/2θ mode, all possible diffraction directions of the lattice should be attained due to the random orientation of the powdered material and the crystalline structures in SLM processed samples. For constructive interference to occur, the path difference between rays must be an integer multiplier of the X-ray's wavelength. A diffraction peak to $2\theta$ plot allows identification of the phases and crystal structure of the material as each material has a set of unique diffraction peaks. This is achieved by comparison with standard reference patterns.

The machine used for this study is PANalytical's Empyrean. Powder samples were compacted and flattened before characterisation. Solid SLM samples were cleaned with ultrasound in ethanol solution and rinsed with deionized water to remove any contaminants. The samples were then polished with diamond abrasives down to 3 µm gradation and placed in dry cabinets for at least 48 hrs before examination with XRD.

### 3.5.2 Light Optical Microscopy – Principles

In light optical microscopy (LOM), visible light is transmitted through or reflected from the sample. This light then passes through a series of lenses that allows a magnified view of the sample. The images can be viewed directly by human eyes or captured digitally with a mounted camera.

LOM has a limited depth of view as the light from points outside the focal plane has much-reduced clarity. The resolution of the LOM is limited by the wavelengths of visible light and the numerical aperture of the optical system. This limitation in resolution is given by $d = \frac{\lambda}{2A_N}$, where $d$ is the scale of the resolution in length, $\lambda$ refers to the wavelength of light and $A_N$ is the numerical aperture of the system.

In the examination of SLM samples with LOM, different phases may be distinguished due to their differences in reflectivity. Etchants may be deployed to separate crystals of different orientations as they are etched at different rates. Etchants also attack grain boundaries preferentially, hence, grains can also be delineated easily. Some etchants could also stain surfaces differently such that grains of different orientations or different phases take on distinctive colours.

The equipment used in this study is the Axioskop 2 MAT, mounted with JVC Digital Colour Video Camera TK-C751EG. The digital imaging software is Image-Pro Plus 6.3.

### 3.5.3 Scanning Electron Microscopy – Principles

Scanning electron microscopy (SEM) uses electron beams instead of visible light. As electron beam has a lower wavelength, $\lambda$, given by the de Broglie relationship of $\lambda = \frac{h}{p}$, where $h$ is the Planck’s constant and $p$ is the momentum of the moving electron. When the electron microscope is operated at 100 kV, the relativistic de Broglie wavelength of the electron would be 3.70 pm. In SEM, the operating acceleration voltage is usually less than 30 kV, giving the system a resolution between 1 nm and 20 nm. Hence, much higher resolution can be achieved with electron beams than with visible light. However, electron beam has to be operated in a vacuum environment.

SEM enables the visualization of the details of the surfaces of particles to give a 3D view. In this aspect, SEM is suitable for examining the surface structures of the samples. Samples with different phrases can contain surface relieves after being etched with suitable etchants. These differences in surface levels enable the observation of different grains and grain boundaries through SEM.

SEM can be further classified by the type of emitter deployed. The common SEM uses a thermionic emitter that uses electrical current to heat up a filament, usually made of tungsten or lanthanum hexaboride. Once the heat overcomes the work function of the material, electrons escape from the filament. Field emission SEM (FESEM) produces electron by placing the filament in a huge electrical potential gradient. This type of emitter gives better brightness, minimizes the evaporation of cathode material and prevents thermal drift during operation. Moreover, FESEM enables a higher resolution compared to SEM with the thermionic emitter.

The equipment used in this study is the JOEL JSM 7600 FESEM microscope. It has additional probes for energy dispersive X-ray spectroscopy (EDXS) for elemental composition analysis and electron backscatter diffraction (EBSD) for examination of crystallographic orientation.

## 3.6 Overview of Methodologies

The increasing number of publication on the research of SLM in recent years has provided a large pool of material for reference. Some of these publications provided useful information in the form of process parameters and attained relative density. Data was also collected from previous experiments conducted in SC3DP.

This chapter has also shown the development of a novel model which links the relationship between process parameters and material properties. The model has shown that there is a relationship between the compensation factor β and the thermal conductivity of their respective materials. However, more information is required to obtain an indicative trend for this empirical relationship. Hence, parameter optimization studies were required for materials with thermal conductivities ranging between 50 W/m·K to 100 W/m·K.

In the parameter optimization studies, a default layer thickness of 0.05 mm was used. The laser power, scanning speed, and hatch spacing were varied. SLM samples were weighed to deduce their densities via Archimedes' principle. Near full density SLM samples were then examined by X-ray diffraction, light optical microscopy and/or scanning electron microscopy. The basics of these methods have been introduced.

**References:**

[1] Wohlers, T., *Wohlers report 2015*. 2015: Wohlers Associates.

[2] Yap, C.Y., et al., *Review of selective laser melting: Materials and applications.* Applied Physics Reviews, 2015. **2**(4): p. 041101.

[3] Buchbinder, D., et al., *High Power Selective Laser Melting (HP SLM) of Aluminum Parts.* Physics Procedia, 2011. **12**: p. 271-278.

[4] Kempen, K., et al., *Process optimization and microstructural analysis for selective laser melting of AlSi10Mg*, in *Solid Freeform Fabrication Symposium*. 2011, University of Texas at Austin: Austin, Texas, USA. p. 484-495.

[5] Spierings, A.B., N. Herres, and G. Levy, *Influence of the particle size distribution on surface quality and mechanical properties in AM steel parts.* Rapid Prototyping Journal, 2011. **17**(3): p. 195-202.

[6] Gu, D., et al., *Densification behavior, microstructure evolution, and wear performance of selective laser melting processed commercially pure titanium.* Acta Materialia, 2012. **60**(9): p. 3849-3860.

[7] Thijs, L., et al., *A study of the microstructural evolution during selective laser melting of Ti–6Al–4V.* Acta Materialia, 2010. **58**(9): p. 3303-3312.

[8] Wang, F., *Mechanical property study on rapid additive layer manufacture Hastelloy® X alloy by selective laser melting technology.* The International Journal of Advanced Manufacturing Technology, 2011. **58**(5-8): p. 545-551.

[9] Zhang, D.Q., et al. *Selective Laser Melting: On the Study of Microstructure of K220*. in *1st International Conference on Progress in Additive Manufacturing*. 2014. Singapore: Research Publishing.

[10] Yadroitsev, I., P. Bertrand, and I. Smurov, *Parametric analysis of the selective laser melting process.* Applied Surface Science, 2007. **253**(19): p. 8064-8069.

[11] Yap, C.Y., et al. *Single track and single layer melting of silica by Seletive Laser Melting*. in *6th International Conference on Advanced Research in Virtual and Rapid Prototyping*. 2013. Leiria, Portugal: CRC Press.

[12] Yadroitsev, I., et al., *Single track formation in selective laser melting of metal powders.* Journal of Materials Processing Technology, 2010. **210**(12): p. 1624-1631.

[13] Loh, L.E., et al., *Selective Laser Melting of aluminium alloy using a uniform beam profile.* Virtual and Physical Prototyping, 2014. **9**(1): p. 11-16.

[14] Yap, C.Y., C.K. Chua, and Z.L. Dong, *An effective analytical model of selective laser melting.* Virtual and Physical Prototyping, 2016: p. 1-6.

[15] Badrossamay, M. and T.H.C. Childs, *Further studies in selective laser melting of stainless and tool steel powders.* International Journal of Machine Tools and Manufacture, 2007. **47**(5): p. 779-784.

[16] Fischer, P., et al., *Sintering of commercially pure titanium powder with a Nd:YAG laser source.* Acta Materialia, 2003. **51**(6): p. 1651-1662.

[17] Tolochko, N.K., et al., *Absorptance of powder materials suitable for laser sintering.* Rapid Prototyping Journal, 2000. **6**(3): p. 155-161.

# Chapter 4

## Selective Laser Melting of AlSi10Mg

*Selective Laser Melting of AlSi10Mg, an aluminium alloy with excellent casting properties, was examined. There had been published literature on the SLM of AlSi10Mg where near full density parts were fabricated. However, the literature provided different combinations of process parameters and the process envelope has never been examined. This study aims to explore the processing envelope for the SLM of AlSi10Mg and to find the most energy efficient combination of process parameters for achieving relative densities higher than 98 %.*

*In addition, X-ray diffraction was carried out to determine the phases in SLM AlSi10Mg components and it was found that the phases contained are similar to those found in Al9Si. Light microscopy and scanning electron microscopy were deployed to study the microstructure of these samples. EDXS was also used to confirm the elemental compositions of SLM samples for this aluminium alloy. 2 regions were identified in the microstructure which contained different atomic percentages of aluminium and silicon. The percentage of magnesium were found to be slightly higher at the melt boundaries.*

*This study also examines the variation of relative density against laser scanning speed, process hatch spacings and the input volumetric energy density. Analysis with volumetric energy density yielded a clear trend and showed the relationship between energy input of the SLM process and the resultant relative density of the components. This also helps to establish the method of analysis for future studies on SLM of nickel and SLM of tin.*

## 4.1 Introduction

AlSi10Mg is an aluminium alloy with good casting properties and has a composition similar to cast aluminium alloy 360.0 as shown in Table 4.1. Its high silicon content gives the alloy low contraction during solidification and thus ensures good castability. In contrast with cast alloy 360.0, AlSi10Mg has a lower tolerance for iron and copper content. Lower iron content improves ductility and lower copper content gives better corrosion resistance to AlSi10Mg.

Table 4.1 Elemental composition comparison of aluminium alloys: AlSi10Mg and 360.0.

| Alloy | EOS AlSi10Mg [1] | UNS 360.0 [2] |
|---|---|---|
| Element | Elemental composition (%) | |
| Al | Bal. | Bal. |
| Si | 9-11 | 9-10 |
| Mg | 0.2-0.45 | 0.4-0.6 |
| Fe | ≤0.55 | ≤2 |
| Cu | ≤0.05 | ≤0.6 |
| Mn | ≤0.45 | - |
| Ni | ≤0.05 | ≤0.5 |
| Zn | ≤0.1 | ≤0.5 |
| Pb | ≤0.05 | - |
| Sn | ≤0.05 | ≤0.15 |
| Ti | ≤0.15 | - |
| Others | - | ≤0.25 |

SLM of AlSi10Mg was first published in 2008 for automotive applications [3]. The application of SLM enabled the building of the water pump in hours instead of days, shortening the development process for a race car engine. Three research groups have shown that near full density parts can be achieved with SLM of AlSi10Mg and shared their optimized parameters in the publications [4-6]. There were also earlier studies done in SC3DP on the SLM of AlSi10Mg where relative density of 99.13 % was achieved. In this study, the required relative density is 98 % and the volumetric energy density (VED), given by laser power over the product of laser scanning speed, hatch spacing and layer thickness ($\frac{P}{vht}$) , of the process is an indicator of its energy efficiency. Hence, the parameters with the lowest VED values that yield relative densities of 98 % or higher were selected for this study. Table 4.2 gives a clear comparison of the parameters shared by these publications.

Table 4.2 Most energy efficient SLM process parameters for achieving relative densities higher than 98 %, as measured by volumetric energy density (VED).

| Sources | SLM parameters | | | | |
|---|---|---|---|---|---|
| | $P$ (W) | $v$ (mm/s) | $h$ (mm) | $t$ (mm) | $VED$ (J/mm$^3$) |
| Buchbinder at al. [4] | 500 | 1700 | 0.15 | 0.05 | 39.2 |
| Kempen et al. [5] | 190 | 1600 | 0.105 | 0.03 | 37.7 |
| Manfredi et al. [6] | 195 | 800 | 0.17 | 0.03 | 47.8 |
| Loh, L. E. [7] | 350 | 1170 | 0.17 | 0.05 | 35.2 |

Information from these earlier studies provides the basis for the examination of SLM process envelope of AlSi10Mg. The aim of this study is to find the most energy efficient process parameters for fabricating parts with a relative density of 98 % or higher via exploration of the SLM process envelope of AlSi10Mg and investigate the difference in VED in comparison with results from literature. Microstructural analyses were also carried out to better understand the SLM fabricated AlSi10Mg components regarding elemental distribution and microstructural features attributed by SLM.

## 4.2 Experimental Methods

AlSi10Mg samples were fabricated. Phases of the samples were studied via XRD. In addition, samples were prepared for microscopy by polishing with diamond paste to 3 μm gradation and cleaning with active oxide polishing suspension. The samples were then etched with Flick’s reagent for 12 s before they were examined by optical microscopy, SEM and EDXS.

### 4.2.1 Synthesis

Synthesis of AlSi10Mg samples was done with the SLM 250 HL machine with a 400 W continuous wave Gaussian beam laser. The wavelength of the laser is 1.06 µm. The laser power and layer thickness were fixed at 360 W and 0.05 mm respectively. The hatch spacing was varied from 0.07 mm to 0.2 mm. The scanning speed of the laser was varied from 500 mm/s to 3,500 mm/s.

### 4.2.2 X-ray Diffraction

XRD was carried out with Empyrean, PANalytical to analyse the crystal structure and phases in the SLM part. The phases identified are similar to those found in Al9Si. The 4 main peaks at 38.50 °, 44.76 °, 65.16 ° and 78.30 ° corresponds to the face centred cubic (FCC) structure crystallographic planes of {1 1 1}, {2 0 0}, {2 2 0} and {3 1 1} respectively. There are also some small observable peaks that correspond to those in intermetallic compound $Al_{3.21}Si_{0.47}$.

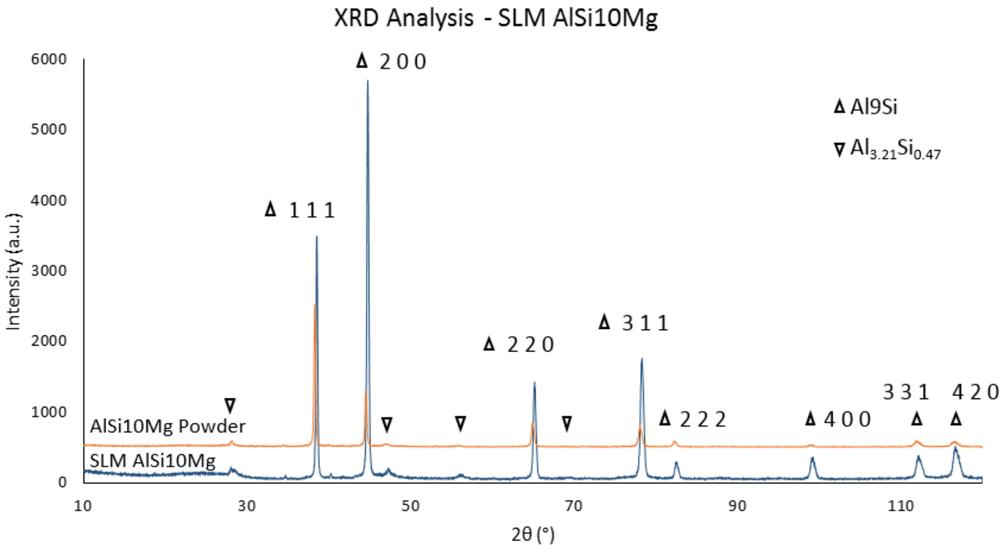

Figure 4.1 XRD analysis of SLM AlSi10Mg showing peaks that match those of Al9Si and $Al_{3.21}Si_{0.47}$.

XRD analysis of the powder shows similar relative heights to that found in the database. However, the AlSi10Mg alloy processed by SLM shows a different trend. The peak that corresponds to the {2 0 0} plane is much higher, indicating relative abundance of the plane. This demonstrates that the SLM process favours the formation of the {2 0 0} plane in AlSi10Mg. A small amount of $Al_{3.21}Si_{0.47}$ is found in the XRD analysis and it is more evident in the SLM processed alloy. $Al_{3.21}Si_{0.47}$ is an intermetallic compound easily formed as a by-product in various manufacturing processes such as laser cladding [8], accumulative roll bonding [9] and sintering [10], as long as aluminium and silicon are involved. The XRD analysis also shows that there is little or no impurities and no other new compound is formed during the SLM process.

### 4.2.3 Light Optical Microscopy

Optical microscopy allows observation of the microstructural features at lower magnifications using visible light, giving a better overview of the microstructure at hundreds of micrometres. Figure 4.2 shows the microstructure under 50× magnification in the XY plane (a) and XZ plane (b). The melt boundaries and the core of the melt pools were etched differently, resulting in different colours and the melt pools can be easily differentiated from one another. The overlapping between neighbouring melting tracks and between successive layer shows that good bonding is achieved in both the x-y plane and z-axis. The near full density sample was also observed to be crack-free, although pores can be observed. The lack of cracks can be attributed to the high silicon content which reduces contraction of the components during the solidification process, minimising the chances of crack formation. In the x-y plane, pores with diameters of about 10 µm, circled in red, can be observed near the melt boundaries. Pores of similar sizes can also be observed in the x-z plane although they are not necessarily found near the melt boundaries.

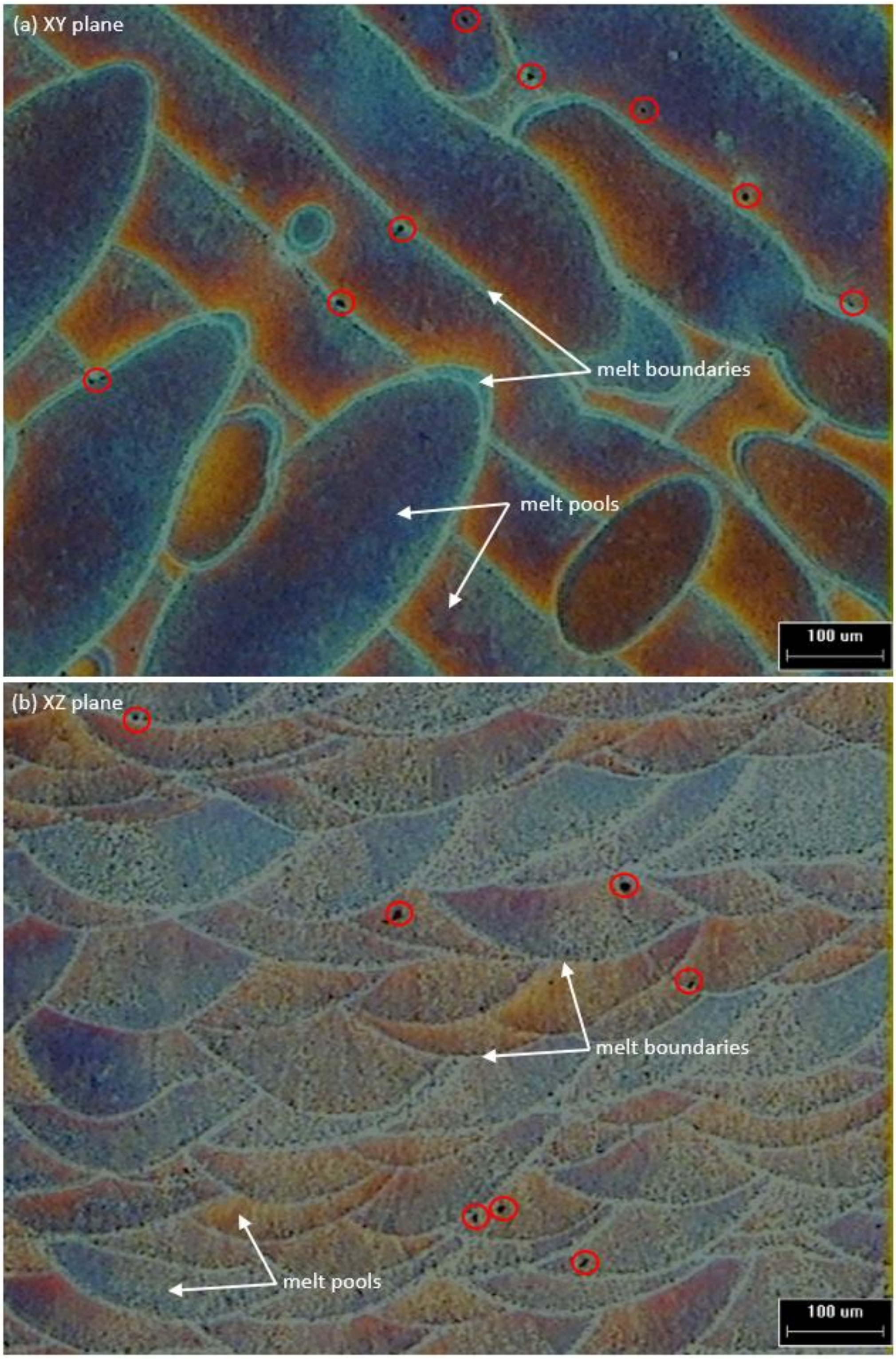
(a) XY plane
melt boundaries
melt pools
100 um
(b) XZ plane
melt boundaries
melt pools
100 um

Figure 4.2 Optical microscopy of SLM AlSi10Mg samples in the x-y plane (a) and x-z plane (b).

### 4.2.4 Scanning Electron Microscopy

SEM analysis allows observation of minute details at much higher magnification than that of the optical microscope. The JOEL JSM 7600 FESEM microscope was operated at an acceleration voltage of 15 kV, which corresponds to a resolution of 3.0 nm. Figure 4.3 shows the micrographs at magnifications of 1,000× and 10,000×. As observed in optical microscopy, the melt boundaries were etched differently by Flick's reagent compared to the core of the melt pool. The melt boundaries seem to have different microstructure compared to the rest of the melt pool.

At a magnification of 10,000×, there are 2 regions observed in the microstructure as shown in Figure 4.3 (bottom right): α region (dark) and β region (light). The α region appears mostly as a rounded structure surrounded by the β region. At the core of the melt pool, α regions have diameters of about 0.5 µm and the structures are mostly round. Whereas at the melt boundaries, α region structures are more irregular and larger, with widths up to 2 µm and lengths up to 5 µm.

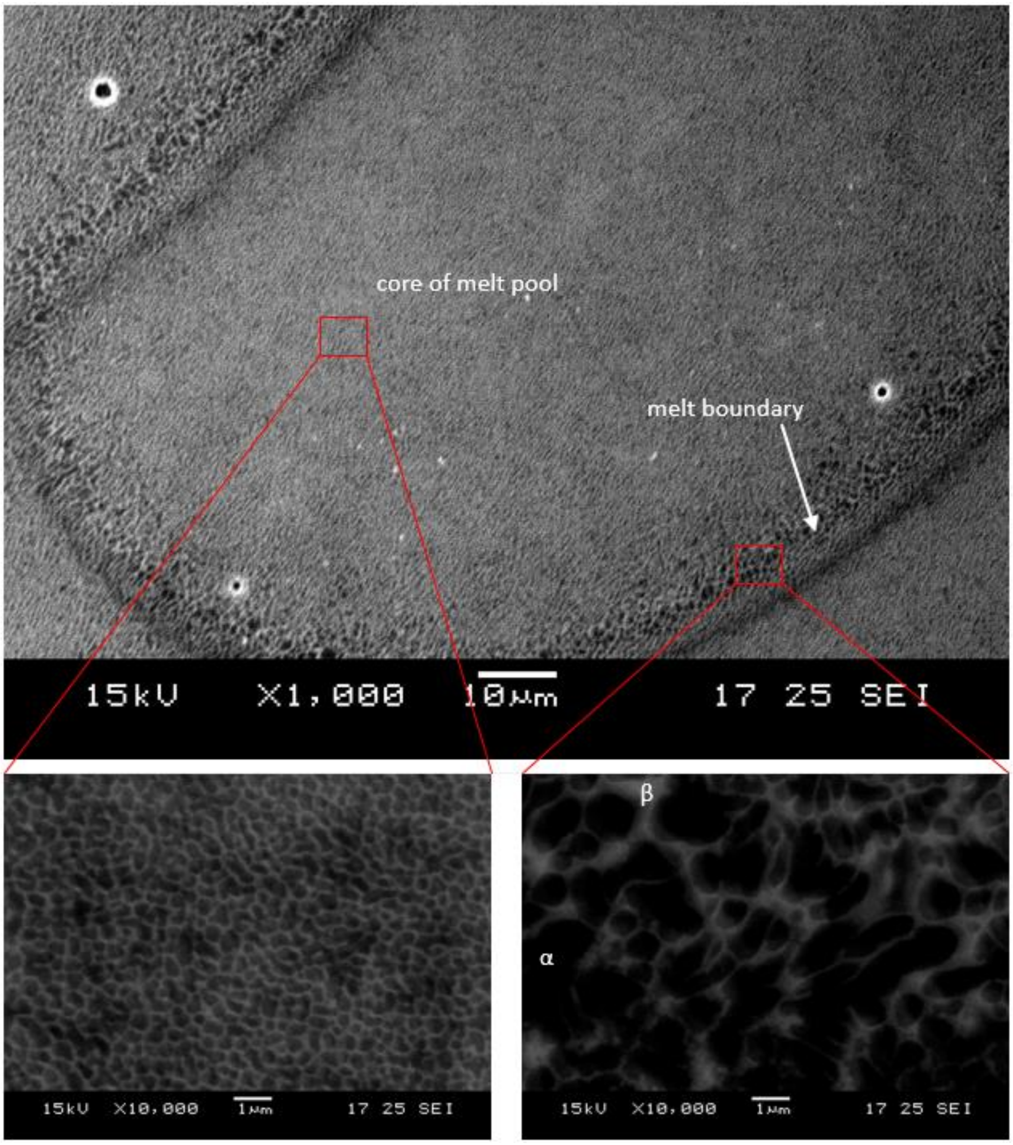
core of melt pool
melt boundary
15kV X1,000 10μm 17 25 SEI
15kV X10,000 1μm 17 25 SEI
β
α
15kV X10,000 1μm 17 25 SEI

Figure 4.3 SEM micrograph of SLM AlSi10Mg sample in the x-y plane at different magnifications, after etching with Flick's reagent.

### 4.2.5 Energy-Dispersive X-ray Spectroscopy

In order to determine the differences between α region and β region, energy-dispersive X-ray spectroscopy (EDX or EDXS) was deployed to study the elemental compositions of each region. EDX allows for measurement of the relative amount of each element and mapping of the elemental distribution. During SEM, high energy electrons impinge on the sample. Some of these electrons collide with low-energy electrons in the atoms, causing the low-energy electrons to leave the atoms. As a result, a vacancy at the low-energy orbit is created and it can be filled by an electron from a higher energy orbit. When an electron transits from a high-energy orbit to low-energy orbit, energy is released in the form of X-rays. As these electronic transitions are specific to each element, the energy levels of the X-rays are unique for each element.

The X-ray detection device is a probe attached to the JOEL JSM 7600 FESEM microscope. An atomic fraction tendency rather than accurate content was provided by EDX analysis. Table 4.3 tabulates the analysis results and compares the elemental composition of the different coloured regions in different areas. At the core of the melt pool, there seems to be no significant difference between the two regions. However, at the melt boundary, the elemental composition of the α region (dark) is similar to that in the melt pool core at about 11.8 at.% to 12 at.% silicon and β region (light) has a significantly higher percentage, at about 16.6 at.% silicon. There is also an observable difference in the atomic percentage of magnesium, which is slightly higher at the melt boundary than at the core of the melt pool.

Table 4.3 EDX analysis on α and β regions of SLM AlSi10Mg.

| | Atomic % | | | |
|---|---|---|---|---|
| Area | Melt core | | Melt boundary | |
| Region | α | β | α | β |
| Element | | | | |
| Aluminium | 87.7 ± 0.2 | 87.8 ± 1.0 | 87.7 ± 1.0 | 82.9 ± 2.5 |
| Silicon | 11.9 ± 0.2 | 11.8 ± 0.8 | 11.9 ± 1.1 | 16.6 ± 2.6 |
| Magnesium | 0.4 ± 0.1 | 0.3 ± 0.2 | 0.5 ± 0.1 | 0.5 ± 0.2 |

The silicon percentage of 11.8 % to 12 % is close to the eutectic composition of 12.2 % [11]. The β region structures at the core of the melt pool are very thin, only about 0.1 µm in width. Hence, EDX analysis of β region at the core could have included the surrounding volume of α region structures, giving similar results to that of α region structures. Therefore, it can be deduced that the β region structures contain a higher amount of silicon at about 16.6 at.% due to segregation during the rapid solidification in SLM, which is also observed in casting [12]. Moreover, the difference observed between the melt boundary and the core of the melt pool is caused by the difference in the sizes of the α region structures. The sizes of the α region can be attributed to the high rate of solidification in the SLM process where rapid heating, melting and cooling occurs. Rapid solidification also leads to a relatively homogeneous elemental distribution in the entire alloy as there was little time for the elements to segregate during solidification.

## 4.3 Principal Outcomes

In this study, the relative densities of the SLM samples are the observable outcome of the experiments. The SLM samples were cleaned via ultrasound and placed in dry cabinets for at least 48 hours before they were weighed with the Mettler Toledo XS204. The densities were derived according to Archimedes' principle. The full density of bulk AlSi10Mg was taken to be 2.68 g/cm$^3$ [5]. Near full density samples have been achieved for SLM of AlSi10Mg. In this section, the results are analysed against a few process parameters to find observable trends. The analysis helps to find a meaningful relationship between the process parameters and establish the means of analysis for SLM of different materials in further studies.

The relative densities of SLM samples were first analysed against the scanning speeds of the laser. The plot (Figure 4.4) shows the spread of the data for laser scanning speeds ranging from 500 mm/s to 3,500 mm/s. Although there seems to be a trend of achieving high relative densities of 99.5 % or higher at speeds between 700 mm/s to 1,500 mm/s, low densities were also obtained at the same given speeds. The spread of densities achieved at particular scanning speeds indicates that there is little or no direct links between relative density and laser scanning speed of the SLM process.

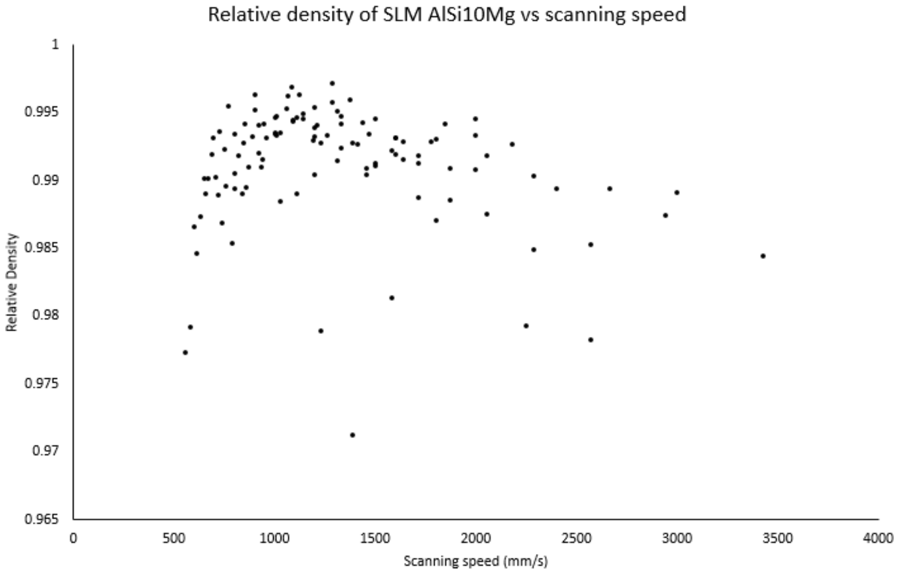

Figure 4.4 Relative densities of SLM AlSi10Mg samples obtained at various scanning speeds, from 500 mm/s to 3,500 mm/s.

When compared with the hatch spacing of the SLM process, the relative densities of SLM AlSi10Mg samples showed a more coherent trend. The mean value of relative density increased with hatch spacing from 0.07 mm to 0.1 mm. Relative densities higher than 99 % were obtained for hatch spacings between 0.09 mm and 0.19 mm. The mean relative density then decreased gradually as the hatch spacing continued to increase from 0.18 mm to 0.2 mm (Figure 4.5).

However, the spread of the data, as given by the minimum and maximum values at each hatch spacing, shows the inconsistency of the results. For instance, the difference between the maximum and minimum value at 0.08 mm hatch spacing is 2.2 % while that at 0.13 mm hatch spacing is only 0.26 %. Moreover, there are abrupt changes between hatch spacing of 0.13 mm and 0.14 mm, where the mean relative density dropped by 0.23 % and the variation of data increase by 0.93 %. At each hatch spacing, the energy input varies. The plot gives an indication that some hatch spacing values can yield near full density parts at a greater range of energy input. Hence, analysing the relative densities of SLM samples against hatch spacing yield an observable trend but it is not conclusive.

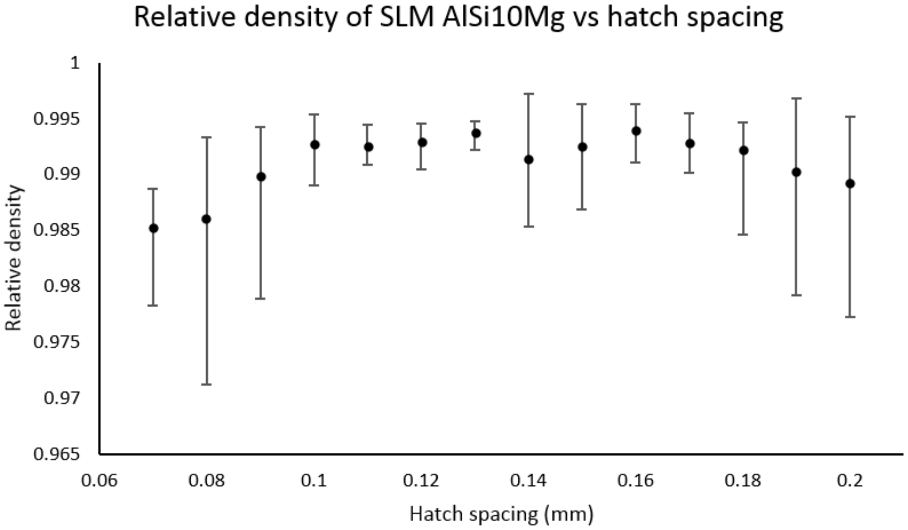

Figure 4.5 Relative densities of SLM AlSi10Mg samples (mean, minimum and maximum) obtained at different hatch spacings, from 0.07 mm to 0.2 mm.

Besides comparing the relative densities of samples against individual process parameters (laser power, scanning speed, hatch spacing or layer thickness), analysis can also be done with the VED of the SLM process. VED, given by $\frac{P}{v \cdot h \cdot t}$, has a unit of J/mm$^3$ and it is a useful indication of the amount of energy invested for the fabrication of a particular material with SLM.

Near full density samples were achieved at VED input of 30 J/mm$^3$ to 60 J/mm$^3$. When the VED is lowered to 25 J/mm$^3$, the densities decreased sharply to about 94 %. Hence, at VED of 25 J/mm$^3$ and below, the power supplied by the laser is no longer sufficient to melt the powder materials fully and create near full density structures for AlSi10Mg. When VED is increased to 65 J/mm$^3$, the densities were lowered to an average of 98.57 % and the variation became significantly larger. The lowering of relative density and the enlargement of variation in the figure shows that the SLM process for AlSi10Mg becomes less stable at VED of about 65 J/mm$^3$. Figure 4.6 shows the results of the density measurements against the input VED. The data points show the average values of the relative density and also the minimum and maximum values obtained at each VED point.

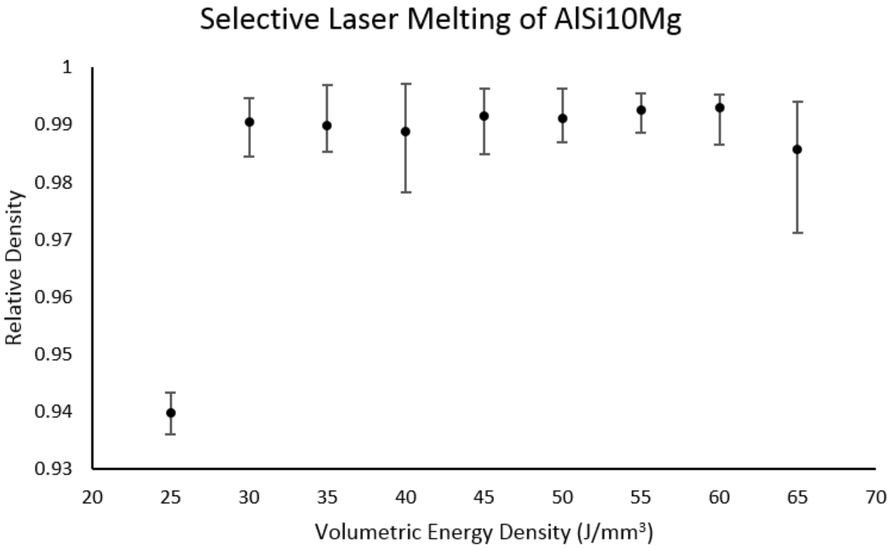

Figure 4.6 Variation of the relative density (mean, minimum and maximum) of SLM AlSi10Mg samples against input volumetric energy density, $\frac{P}{vht}$.

From the three analyses mentioned above, comparing relative density to VED has yielded a clear trend and relationship between process parameters and the relative densities achieved. Moreover, via the study conducted, a more energy efficient combination of process parameters has been found for achieving relative densities higher than 98 %. The lowest VED value for this was 30 J/mm$^3$. This result rebukes a recent study on the process energy threshold of 60 – 75 J/mm$^3$ [13] and it is also significantly smaller than that of 35.2 J/mm$^3$ reported in the earlier studies (Table 4.2). For future studies, the densities of SLM parts will be analysed against the hatch spacing and VED of the process.

**References:**

[1] GmbH, E., *Material Data Sheet: EOS Aluminium AlSi10Mg*, E. GmbH, Editor. 2014: Munich.

[2] Kearney, A.L., *Properties of Cast Aluminum Alloys, Properties and Selection: Nonferrous Alloys and Special-Purpose Materials*, in *ASM Handbook*. 1990, ASM International: Ohio, United States of America. p. 152–177.

[3] Vilaro, T., S. Abed, and W. Knapp. *Direct manufacturing of technical parts using selective laser melting: example of automotive application*. in *Proc. of 12th European Forum on Rapid Prototyping*. 2008.

[4] Buchbinder, D., et al., *High Power Selective Laser Melting (HP SLM) of Aluminum Parts.* Physics Procedia, 2011. **12**: p. 271-278.

[5] Kempen, K., et al., *Process optimization and microstructural analysis for selective laser melting of AlSi10Mg*, in *Solid Freeform Fabrication Symposium*. 2011, University of Texas at Austin: Austin, Texas, USA. p. 484-495.

[6] Manfredi, D., et al., *From Powders to Dense Metal Parts: Characterization of a Commercial AlSiMg Alloy Processed through Direct Metal Laser Sintering.* Materials, 2013. **6**(3): p. 856-869.

[7] Loh, L.E., *Selective laser melting of aluminium alloys : numerical modelling and material properties characterisation*, in *School of Mechanical and Aerospace Engineering*. 2014, Nanyang Technological University: Singapore.

[8] Cai, L., C. Mark, and W. Zhou, *Laser cladding of magnesium alloy Az91d with silicon carbide.* Surface Review and Letters, 2009. **16**(02): p. 215-221.

[9] El Mahallawy, N., et al., *Microstructure evolution and mechanical properties of Al/Al–12% Si multilayer processed by accumulative roll bonding (ARB).* Materials Science and Engineering: A, 2015. **647**: p. 127-135.

[10] Wang, H.L., et al. *Preparation of Al-based Metal Matrix Composites Reinforced by Cu Coated SiC Particles*. in *Key Engineering Materials*. 2004. Trans Tech Publ.

[11] Murray, J. and A. McAlister, *The Al-Si (aluminum-silicon) system.* Bulletin of alloy phase diagrams, 1984. **5**(1): p. 74-84.

[12] Snugovsky, L., et al., *Silicon segregation in aluminium casting alloy*. Materials science and technology, 2013. **16**(2), 125-128.

[13] Read, N., et al., *Selective laser melting of AlSi10Mg alloy: Process optimisation and mechanical properties development.* Materials & Design, 2015. **65**: p. 417-424.

# Chapter 5

# Selective Laser Melting of Nickel

*Selective Laser Melting of pure nickel, an important alloying metal known for its resistance to corrosion and performance at high temperatures, was examined. There had been no previous literature on the SLM of pure nickel where 3D parts were fabricated. Hence, this novel study aims to determine the feasibility of processing nickel with SLM and the optimal parameters for such a process. The energy input required to achieve relative densities higher than 98.0 % will also be examined.*

*X-ray diffraction was carried out to compare the phases in SLM nickel components and the corresponding powder. Light microscopy (LOM) and scanning electron microscopy (SEM) were also deployed to study the microstructure of these samples. The grains were clearly distinguishable under LOM but not so under SEM. Under LOM, imprints of the SLM process could be seen although the melt tracks were filled with small grains of different sizes varying from 15 µm to 100 µm. Electron backscattering diffraction (EBSD) was used to map the local crystal orientations of SLM nickel samples in both the XY plane and the XZ plane.*

*This study also examines the variation of relative density against process hatch spacings and the input volumetric energy density for* *the SLM of nickel. Relative density as high as 99.0 % was achieved. Analysis with volumetric energy density alone shows that the energy required to achieve relative density higher than 98.0 % is 120 J/mm$^3$. However, it is observed that at hatch spacing of 0.14 mm, the relative density of 98.5 % can be consistently achieved at a lower VED of 100 J/mm$^3$. This study shows that hatch spacing can uniquely affect the energy requirement for fabrication of near full density parts in SLM.*

## 5.1 Introduction

Nickel is a transition metal with atomic number 28, discovered in 1751 by Swedish mineralogist Axel Fredrik Cronstedt. Nickel has a face-centred cubic (FCC) crystal structure, a density of 8.89 g/cm$^3$ and a melting point of 1455 °C. It has excellent corrosion resistance and is susceptible to magnetization. It is an important material in our society in both elemental form and alloyed with other metals. Most of them are focused on corrosion-resistant and on heat-resistant applications. According to ASM International, nickel is most often used as an alloying element in steel, which takes up 66.5 % of the consumption of nickel in 1990, and nickel-base alloys only account for 13 % for the nickel usage [1].

Nickel based alloys are often applied in aircraft gas turbines, steam turbine power plants and metal processing for their heat-resistant properties. Such alloys include nickel-chromium based Inconel and Hastelloy which are oxidation- and corrosion-resistant and suitable for service in high heat and high-pressure environments. These are also known as nickel superalloys. In addition, nickel can alloy with titanium to form a shape memory alloy, Nitinol. Nitinol can undergo deformation at lower temperatures and return to its original shape when heated to its transformation temperature, which has a range of 20 °C to 50 °C. However, these useful alloys are difficult to machine or manufacture by conventional methods. Nickel superalloys are difficult to shape due to rapid work hardening while Nitinol has a very strict compositional requirement and the titanium that is needed is highly reactive.

Pure nickel is known for its corrosion resistance against alkali, making it a suitable coating material. Its magnetostrictive properties allow it to be used as transducers and it has been studied as an alternative to gold as a transducing platform for bio-sensing applications [2]. Nickel also makes for a cost-effective chemical catalyst. Since it is magnetic, nickel can be a magnetically separable catalyst [3].

Selective laser melting, as a powder-bed fusion additive manufacturing technique, provides an alternative manufacturing method for the processing of these metals. One of the pioneering work in powder bed based direct laser processing of nickel-based alloy is done by Das et al on Inconel 625, in which a relative density of 98.5 % was achieved [4]. In later works, near full density parts were also achieved with SLM for nickel-based alloys such as Inconel 718 (99.98 %) [5, 6], Hastelloy X (99.75 %) [7], Nimonic 263 (99.7 %) [8], MAR M-247 (98 %) [9] and CM247LC (99.12 %) [10]. SLM has also been proven capable of producing parts out of Nitinol powders and it been studied for its potential application as a smart material implant [11, 12].

However, there has been no previous publication on the SLM fabrication of pure nickel components. SLM of pure nickel powder was reported in a study concerning the linear energy density of the process and the universality of the “balling” phenomenon in SLM [13]. This novel work has been submitted for publication in Rapid Prototyping Journal and is currently under review.

## 5.2 Experimental Methods

Pure nickel samples were fabricated. Material crystallography was studied via XRD. In addition, samples were prepared for microscopy by polishing with diamond paste to 3 µm gradation and cleaning with active oxide polishing suspension. The samples were then etched with Marble’s reagent for 12 s before they were examined by optical microscopy and SEM. EBSD was used to determine the orientation of each crystal grain.

### 5.2.1 Synthesis

Spherical nickel powders were used in this experiment (Figure 5.1). The powders used had a size distribution corresponding to d(0.5) = 20 µm and d(0.9) = 45 µm. SLM machine used was the SLM 250 HL. It has a single mode, continuous-wave ytterbium fibre laser with Gaussian beam profile, standing spot diameter of 80 µm and a wavelength of 1.06 µm.

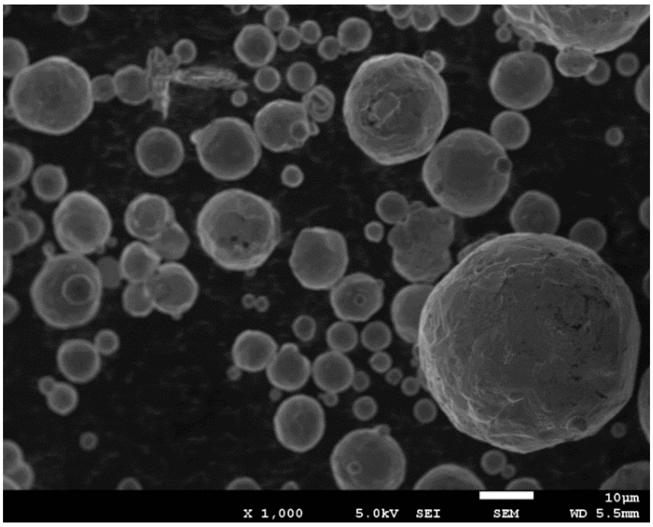

Figure 5.1 Spherical nickel powders used in the investigation with SLM.

In this study, the laser power was fixed at 360 W and the layer thickness was 50 µm. The hatch spacing was varied from 0.1 mm to 0.2 mm and the scanning speed ranged from 175 mm/s to 700 mm/s.

### 5.2.2 X-Ray Diffraction

XRD was carried out with Empyrean, PANalytical to analyse the crystal structure and phases in the powder feedstock and the SLM part. The analysis shows no change in the phase nor elemental composition between the SLM processed nickel and the nickel powder as they show the same main peaks (Figure 5.2). The 5 main peaks at 2θ of 44.53 °, 51.89 °, 76.44 °, 93.02 ° and 98.53 ° correspond to the crystallographic planes of {1 1 1}, {0 0 2}, {0 2 2}, {1 1 3} and {2 2 2} respectively. There is also a small observable peak at about 29 °. This may be caused by trace amounts of impurities.

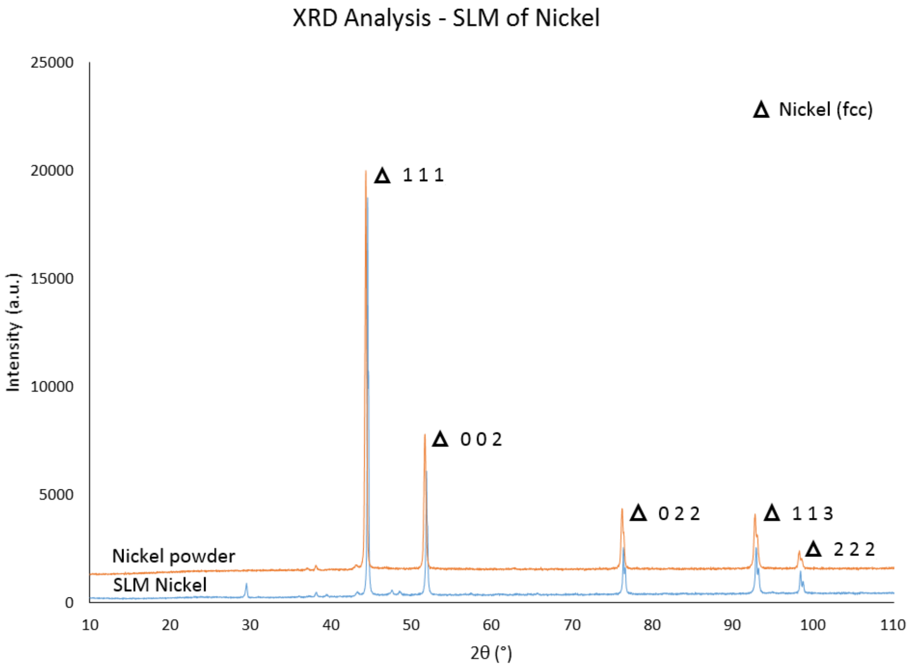

Figure 5.2 X-ray Diffraction analysis of nickel powder and SLM processed nickel sample.

### 5.2.3 Light Optical Microscopy

In lower magnifications, effects of the melt vectors on the microstructure of the SLM nickel parts can be seen in the XY plane. Crystal grains along a single melt vector have lengths of about 50 to 100 µm and widths of 20 to 50 µm, as shown in Figure 5.3 (a), and they are packed next to each other in the melt vector. However, in the XZ plane, traces of the melt vectors are not as apparent as in AlSi10Mg samples shown in Chapter 4 (Figure 4.2). In SLM nickel, the semi-ellipse cross sections are harder to identify as multiple crystals are formed within one melt pool. The grains are elongated in the *z*-direction, as shown in Figure 5.3 (b). Thus, it is difficult to discern the layer thickness of 50 µm. Nonetheless, some curved lines can be observed that indicate the curvature of melt pools. However, some of the grains can be seen to have continued from the preceding layer, indicating continued crystal growth, good melt penetration, and good interlayer bonding. The red boxes in (a) and (b) indicate the areas that will be shown subsequently in Figure 5.4.

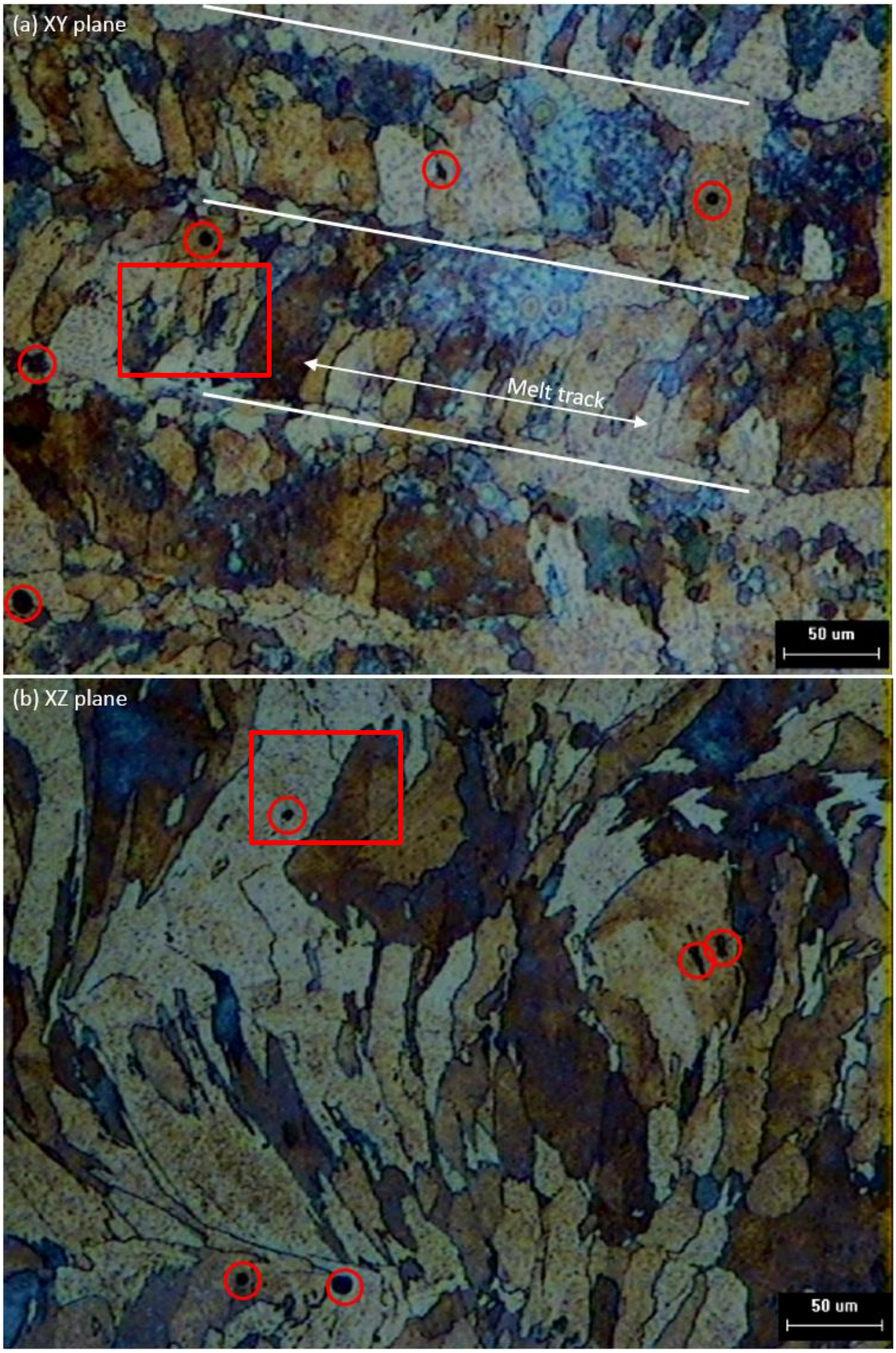
(a) XY plane
Melt track
50 um
(b) XZ plane
50 um

Figure 5.3 Optical microscopy images of SLM processed nickel at a lower magnification, showing XY planes (a) and XZ planes (b).

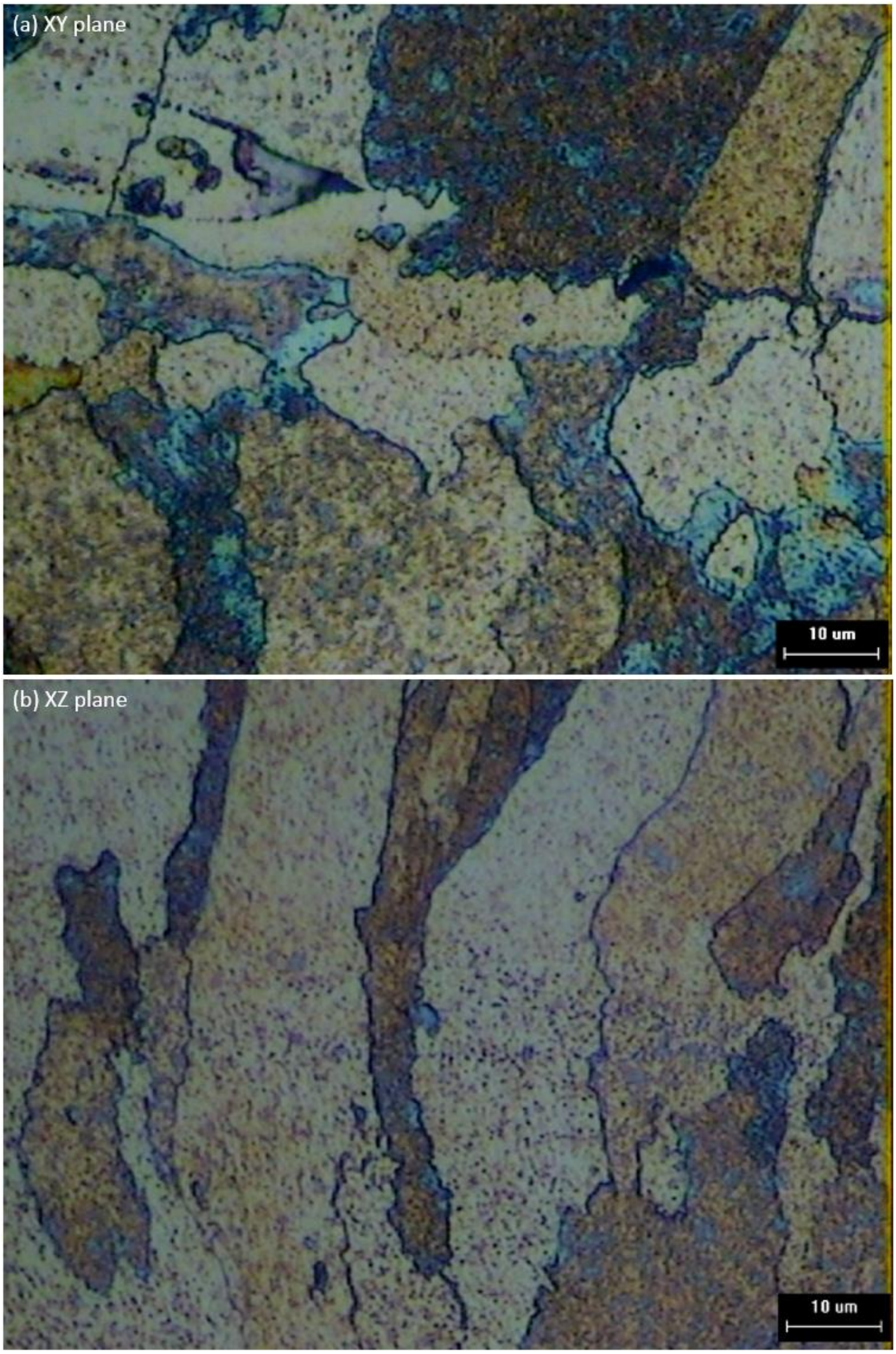
(a) XY plane
10 um
(b) XZ plane
10 um

Figure 5.4 LOM images of SLM nickel at a higher magnification. These areas observed corresponds to the areas indicated by the red boxes in Figure 5.3.

In addition, pores smaller than 10 µm in diameter can be observed. Pores, circled in red (Figure 5.3), can be found in two types of location: (1) within a crystal grain and (2) at the grain boundaries. Pores found within a crystal grain have a circular cross section, indicating a spherical pore. Pores at the grain boundaries are irregular in shape, conforming to the directions of the grain boundaries. More irregular pores are found at the boundaries of the melt tracks as more grain boundaries are present in smaller grains. These pores are randomly distributed and are possibly the results of trapped air during the rapid melting and solidification process during SLM and the void left behind by the contraction of crystal grains as they crystallize. These pores can lead to lower tensile strength, fatigue strength, and creep resistance of the product as they act as areas of stress concentration.

### 5.2.4 Scanning Electron Microscopy

SEM was carried out with the JOEL JSM 7600 FESEM microscope, operated at an acceleration voltage of 7 kV. Figure 5.5 shows the micrographs at a magnification of 100×. Pores between 5 µm to 10 µm in diameter, circled in red, are found randomly distributed in both planes. However, in contrast with the images from optical microscopy, the images from SEM show the different crystal orientations in different shades of grey, which make delineation of grain boundaries difficult. Unlike the previously mentioned AlSi10Mg, the material being studied here is a simple elemental metal, which does not have different phases. Instead, the main difference that can be observed will be the difference in crystal orientations. In this case, etching does not create a clear difference in the 3D structure of the observing plane and SEM images do not produce clear delineations.

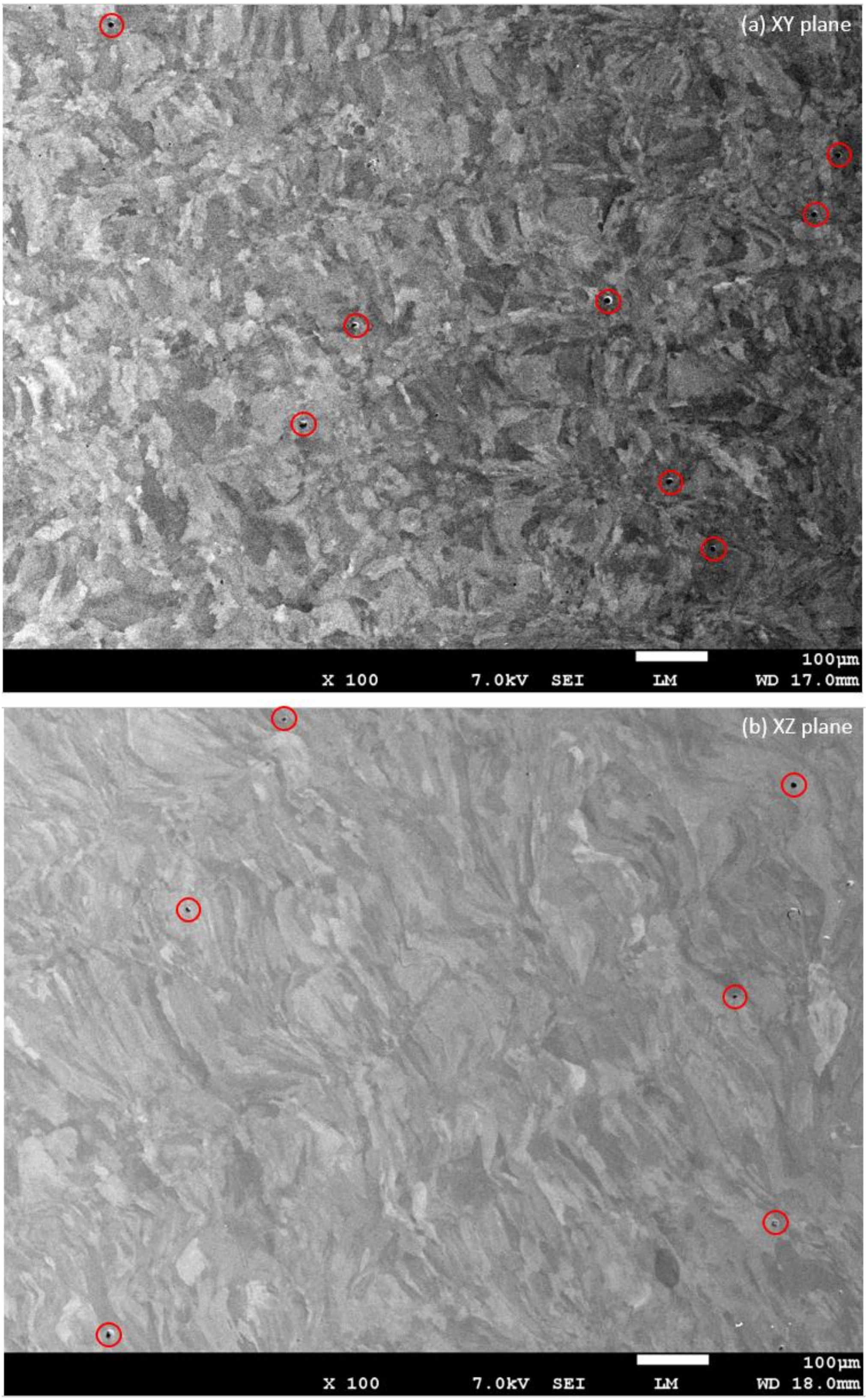
(a) XY plane
100µm
X 100
7.0kV
SEI
LM
WD 17.0mm
(b) XZ plane
100µm
X 100
7.0kV
SEI
LM
WD 18.0mm

Figure 5.5 Scanning electron microscopy of SLM nickel samples in the (a) XY plane and (b) XZ plane.

### 5.2.5 Electron Backscatter Diffraction

In order to examine the crystal orientation of the SLM fabricated parts, electron backscatter diffraction (EBSD) analysis was carried out alongside with SEM. EBSD measures the local crystal orientation of sub-micron spatial resolution. It can also be used to find the distribution of phases and crystal orientations in an area of observation. In Figure 5.6, the high angle grain boundaries (HAGBs, misorientation > 15 °) are shown in black and low angle grain boundaries (LAGBs, misorientation < 15 °) in grey. This EBSD analysis also reveals numerous crystal grains smaller than 10 µm.

From the misorientation angle distribution analysis, roughly 94 % of the grain boundaries are HAGBs. The observed difference in colouration of the grains in the light microscopy images is due to differences in crystal orientation. In the XY plane, most of the crystals are in the <0 0 1> and <1 0 1> orientation, as shown by a larger proportion of red and green coloured grains in the map. While in the XZ plane, the crystals are mostly in the <0 0 1> and <1 1 1> orientation. The EBSD mapping of both the XY and XZ planes show little indications of a single preferential grain growth orientation in SLM nickel.

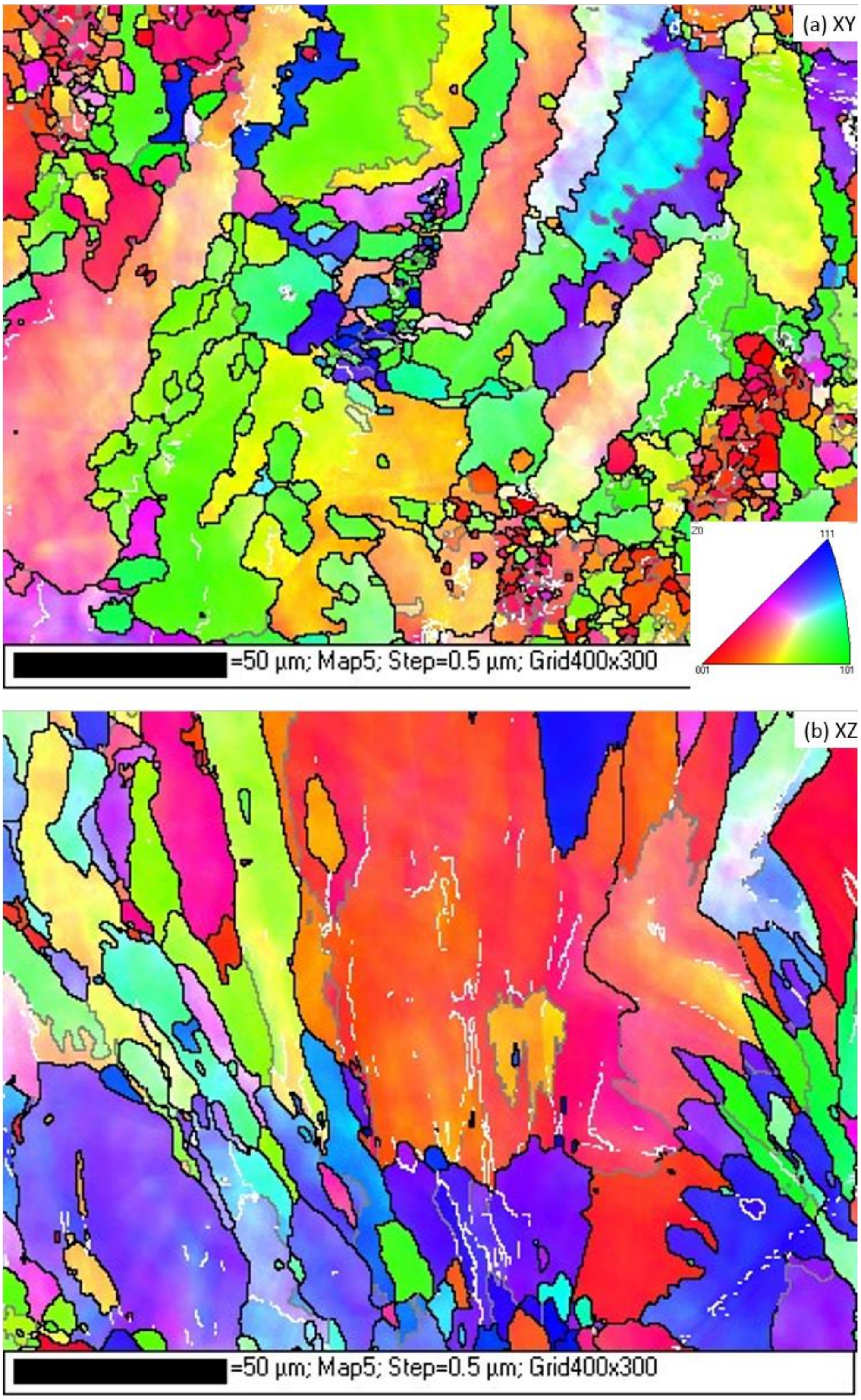
(a) XY
=50 µm; Map5; Step=0.5 µm; Grid400x300
Z0
111
001
101
(b) XZ
=50 µm; Map5; Step=0.5 µm; Grid400x300

Figure 5.6 EBSD analysis of SLM processed nickel, displaying the different crystal orientations: <0 0 1> in red, <1 0 1> in green and <1 1 1> in blue.

## 5.3 Principal Outcomes

In this study, 3D samples were successfully fabricated with pure nickel powder via the SLM process. These samples were then cleaned and dried for at least 48 hours before they were weighed with the Mettler Toledo XS204. The densities were derived according to Archimedes' principle. The full density of bulk nickel is 8.89 g/cm$^3$. As established in Chapter 4, the results are analysed against hatch spacing and input volumetric energy density (VED).

Throughout the experiments, laser power was maintained at 350 W while scanning speeds were varied from 175 mm/s to 700 mm/s and hatch spacing ranged from 0.1 mm to 0.2 mm. The resultant density of the SLM processed samples was analysed against both the hatch spacing and the input energy density of the process. Five samples were made for each combination of energy density, ranging from 100 J/mm$^3$ to 200 J/mm$^3$, and hatch spacing. The results of the experiments are shown in Figure 5.7.

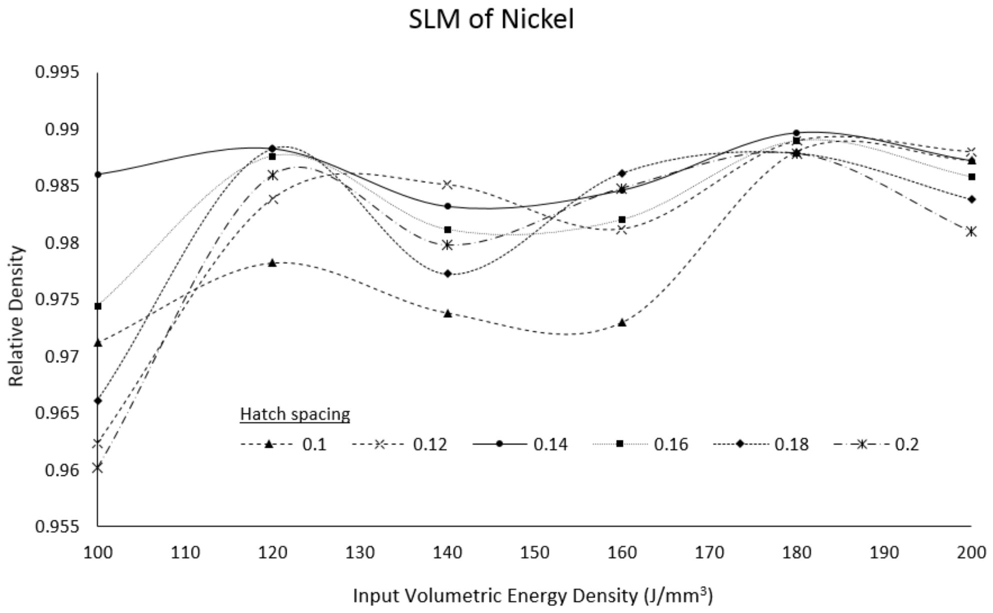

Figure 5.7 Relative density of SLM Nickel samples plotted against input volumetric energy density at different hatch spacings.

Without considering the differences in hatch spacing, the mean relative density achieved at 100 J/mm$^3$ is 97.0 % while the mean relative density reached 98.5 % at 120 J/mm$^3$. However, when the results are differentiated according to their hatch spacings, an optimal hatch spacing can be observed. At hatch spacing of 0.14 mm, SLM processing of nickel was still able to achieve densities of 98 % and above consistently even at a lower VED of 100 J/mm$^3$. Whereas for other hatch spacing values, the relative densities obtained at 100 J/mm$^3$ ranged between 96.0 % and 97.5 %.

From this work, nickel has been proven to be a viable material for processing with SLM. More research on the SLM can be done in order to achieve shorter processing time and determine the mechanical properties of SLM nickel such as tensile strength, compressive strength and creep resistance, which are important aspects to understand for further applications. Furthermore, results from this work provide data for the semi-empirical modelling of the SLM process.

**References:**

[1] Mankins, W.L. and S. Lamb, *Nickel and Nickel Alloys, Properties and Selection: Nonferrous Alloys and Special-Purpose Materials*, in *ASM Handbook*. 1990, ASM International: Ohio, United States of America. p. 428-445.

[2] Kallempudi, S.S. and Y. Gurbuz, *A nanostructured-nickel based interdigitated capacitive transducer for biosensor applications.* Sensors and Actuators B: Chemical, 2011. **160**(1): p. 891-898.

[3] Xiong, J., et al., *Porous hierarchical nickel nanostructures and their application as a magnetically separable catalyst.* Journal of Materials Chemistry, 2012. **22**(24): p. 11927.

[4] Das, S., et al. *Direct selective laser sintering and containerless hot isostatic pressing for high performance metal components*. in *Solid Freeform Fabrication Symposium*. 1997. University of Texas at Austin.

[5] Papadakis, L., et al., *A computational reduction model for appraising structural effects in selective laser melting manufacturing.* Virtual and Physical Prototyping, 2014. **9**(1): p. 17-25.

[6] Sanz, C. and V. García Navas, *Structural integrity of direct metal laser sintered parts subjected to thermal and finishing treatments.* Journal of Materials Processing Technology, 2013. **213**(12): p. 2126-2136.

[7] Wang, F., X.H. Wu, and D. Clark, *On direct laser deposited Hastelloy X: dimension, surface finish, microstructure and mechanical properties.* Materials Science and Technology, 2011. **27**(1): p. 344-356.

[8] Vilaro, T., et al., *Microstructural and mechanical approaches of the selective laser melting process applied to a nickel-base superalloy.* Materials Science and Engineering: A, 2012. **534**: p. 446-451.

[9] Hagedorn, Y., et al. *Processing of nickel based superalloy MAR M-247 by means of High Temperature–Selective Laser Melting (HT–SLM)*. in *High Value Manufacturing: Advanced Research in Virtual and Rapid Prototyping: Proceedings of the 6th International Conference on Advanced Research in Virtual and Rapid Prototyping, Leiria, Portugal, 1-5 October, 2013*. 2013. CRC Press.

[10] Carter, L.N., et al., *The influence of the laser scan strategy on grain structure and cracking behaviour in SLM powder-bed fabricated nickel superalloy.* Journal of Alloys and Compounds, 2014. **615**: p. 338-347.

[11] Bormann, T., et al., *Tailoring Selective Laser Melting Process Parameters for NiTi Implants.* Journal of Materials Engineering and Performance, 2012. **21**(12): p. 2519-2524.

[12] Habijan, T., et al., *The biocompatibility of dense and porous Nickel-Titanium produced by selective laser melting.* Mater Sci Eng C Mater Biol Appl, 2013. **33**(1): p. 419-26.

[13] Li, R., et al., *Balling behavior of stainless steel and nickel powder during selective laser melting process.* The International Journal of Advanced Manufacturing Technology, 2011. **59**(9-12): p. 1025-1035.

# Chapter 6

# Selective Laser Melting of Tin

*Selective Laser Melting of pure tin, a post-transition metal known for its low crystallization temperature and applications in soldering, was examined. Moreover, near full density 3D tin samples were successfully fabricated with SLM for the first time. Process parameters and energy input required for achieving such components were also examined.*

*X-ray diffraction was carried out to compare the phases in SLM tin components and the corresponding tin powder. Light microscopy (LOM) and scanning electron microscopy (SEM) were also deployed to study the microstructure of the SLM fabricated samples. The grains were clearly distinguishable under LOM and columnar structures were observed in the vertical (XZ) plane. However, imprints of the SLM process could not be seen, in contrast with previous observations in AlSi10Mg and pure nickel. Electron backscattering diffraction (EBSD) was used to map the crystal orientations of SLM tin samples in both the XY plane and the XZ plane. EBSD analyses and XRD results have shown that the SLM process favours the formation of particular crystal orientations in pure tin.*

*This study also examines the variation of relative density against process hatch spacings and the input volumetric energy density for the SLM of tin. The energy input required to fabricate parts with at least 98.0 % relative density was determined to be 5.0 J/mm*$^3$ *and relative density as high as 99.9 % was achieved in the study. Effects of hatch spacing on the density of SLM fabricated tin were also elucidated in the study.*

## 6.1 Introduction

Tin is a post-transition metal with atomic number 50. It has two phases: α-tin and β-tin. α-tin, also known as grey tin, is stable below 13.2 °C. It is brittle and has a face-centred cubic crystal structure, with a density of 5.765 g/cm$^3$. α-tin does not display any metallic properties as its atoms form covalent bonds and electrons cannot move freely as in metallic structures. On the other hand, β-tin is stable at and above room temperatures and displays metallic properties. It has a body-centred tetragonal crystal structure, a density of 7.298 g/cm$^3$ and a melting point of 231.9 °C.

In modern times, tin's low melting point made it a popular element in soft solders, which typically contain more than 60 % tin. In addition, tin is corrosion-resistant has low toxicity. Hence, it is also used to protect other metals via tin plating and tin-plated steel is often used for food packaging as tin cans. Moreover, tin is also commonly alloyed with copper to make pewter (85-99 % tin), bell metal (22 % tin) and bronze (12 % tin). Recent studies have also shown that pure tin, when coupled with conductive polymer, can provide high specific capacity and high cycling stability for Na+ cells [1, 2].

At the early stage of the development of laser-based powder bed fusion processes, tin has been chosen as a binding material for its relatively low crystallization temperature. The direct laser processing of Fe-Sn, Cu-Sn, and Ni-Sn powder mixtures had been examined [3-6]. These early results showed that the materials had only undergone sintering, producing parts that are highly porous. In a more recent study, bronze (Cu-10Sn) was produced with SLM and a relative density of 99.7 % was achieved with improved tensile strength (180 MPa to 420 MPa) and ductility (7 % to 17 %) compared to cast parts even though the phases in both SLM and cast parts are essentially the same [7]. The improvement in tensile performance was attributed to the smaller ductile regions in SLM processed parts which reduce dislocation movements.

In the study of direct selective laser sintering of pure tin, “balling” prevented good interlayer bonding and caused delamination [8]. This phenomenon is also commonly found in selective laser melting [9] and it occurs when the energy input of the process creates a large spherical melt pool. As the pool is surrounded by loose powders, there is little tensile traction to confine the melt pool to a layer-wise geometry as is the case in laser cladding [10]. To the best of the author’s knowledge, suitable combinations of parameters have not been found for processing of pure tin with SLM.

## 6.2 Experimental Methods

Pure tin samples, (8 × 8 × 8) $\text{mm}^3$, were fabricated. Material crystallography was studied via XRD. In addition, samples were prepared for microscopy by polishing with SiC sandpaper and diamond paste to 3 µm gradation and cleaning with active oxide polishing suspension. The samples were then etched with a solution of 2 % HCl and 98 % methanol for 120 s before they were examined by optical microscopy and SEM. EBSD was also used to determine the orientation of the grains.

### 6.2.1 Synthesis

Spherical tin powders were used in this experiment (Figure 6.1). The powders used were purchased from TLS Technik GmbH and had a mesh size of 325. The settled apparent density of 3.48 $\text{g/cm}^3$. Energy-dispersive X-ray spectroscopy showed that the powder material has a purity of 99.8 %.

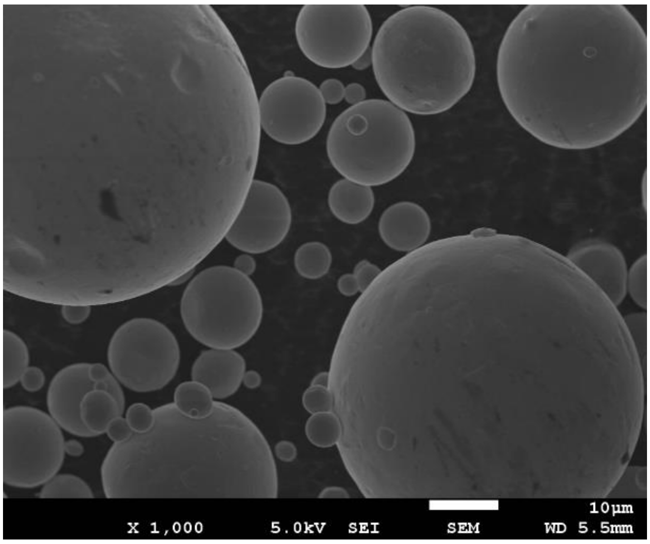

Figure 6.1 SEM micrograph of spherical Sn powders used for SLM.

SLM machine used was the SLM 250 HL, which has a single mode continuous-wave ytterbium fibre laser with Gaussian beam profile, standing spot diameter of 80 µm and a wavelength of 1.06 µm. The laser scanning speed was fixed at 3,000 mm/s. The layer thickness was 50 µm. The hatch spacing was varied from 0.10 mm to 0.18 mm and the laser power ranged from 60 W to 162 W.

### 6.2.2 X-Ray Diffraction

XRD was carried out with Empyrean, PANalytical. The analysis showed some changes in the phase composition between the SLM processed tin and the tin powder (Figure 6.2). The 4 main peaks of the powder material, at 2θ of 30.66 °, 32.04 °, 44.94 ° and 62.58 °, correspond to the crystallographic planes of {2 0 0}, {1 0 1}, {2 1 1} and {1 1 2} respectively. Whereas the 4 main peaks of the SLM processed tin are at 2θ of 44.94 °, 62.58 °, 79.59 ° and 95.26 °, corresponding to the crystallographic planes of {2 1 1}, {1 1 2}, {3 1 2} and {1 0 3} respectively. XRD analysis of the tin powder also suggests a significant but relatively small amount of amorphous structure in the powder material.

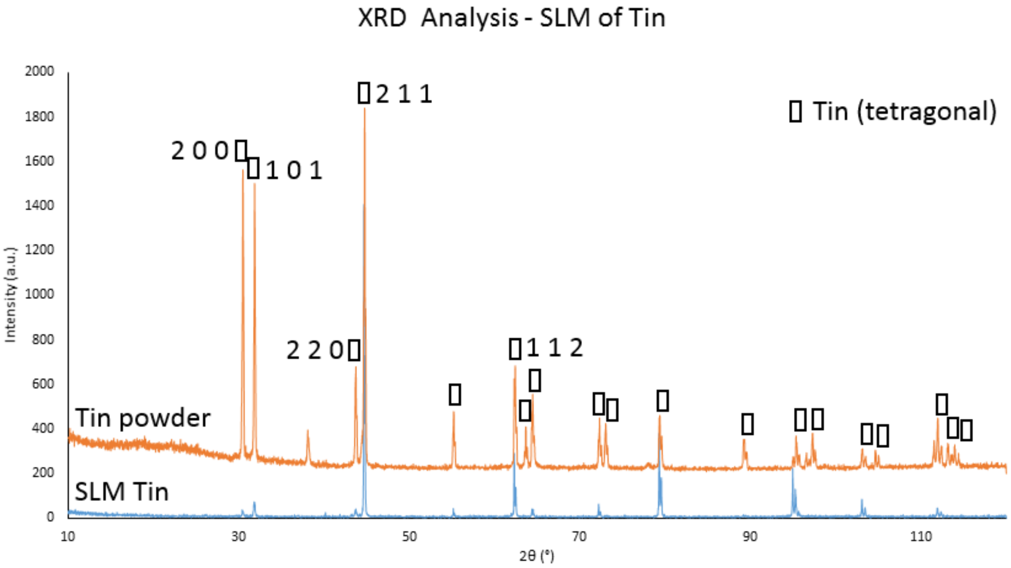

Figure 6.2 X-ray Diffraction analysis of tin powder and SLM processed tin powder. The analysis shows different relative peaks for the two materials.

XRD analysis suggests that the SLM process favours the formation of particular crystal orientations while significantly reducing others. For instance, the amount of {2 0 0} and {1 0 1} planes were drastically reduced when compared to the analysis of the powder material. The presence of preferential grain orientation is caused by the formation of columnar structure, resulting in the same crystal orientation in the materials that are melted and crystallized with the preceding layers. Moreover, there was no amorphous structure in the SLM processed samples.

### 6.2.3 Light Optical Microscopy

Light microscopy was carried out on SLM tin samples. The samples were polished and subsequently etched for 120 s in a solution of 2 ml hydrochloric acid and 98 ml methanol. Pores can be seen in Figure 6.3, which was taken at a lower magnification. The XY plane did not exhibit any characteristic microstructures seen in SLM processed parts such as those in AlSi10Mg or nickel. The grains seemed to have a random distribution in the XY plane. In the XZ plane, there were also little traces of the melt pool formed during the SLM process, which was evident in AlSi10Mg samples shown in Chapter 5. Instead, the cross section observation revealed elongated columnar structures. A fraction of these columnar structures stretched from the bottom to the top of the sample. Furthermore, there were also zig-zag patterns on the grains near the sides of the samples (Figure 6.4). Twinned grains and recrystallized grains could also be observed. These deformations were the results of working during the polishing process and tin is extremely susceptible to such phenomenon as it has a low hardness and a low crystallization temperature of 231.9 °C. Diagonal grains at the sides of powder bed based fusion parts has been studied by Antonysamy et al. [11]. However, in his study, the diagonal grains are the results of powder nucleation and have an upward slope from outside, which are in line with the temperature gradient during the fabrication process. In SLM processed tin, the diagonal grains were observed to have a downward slope from the outside instead.

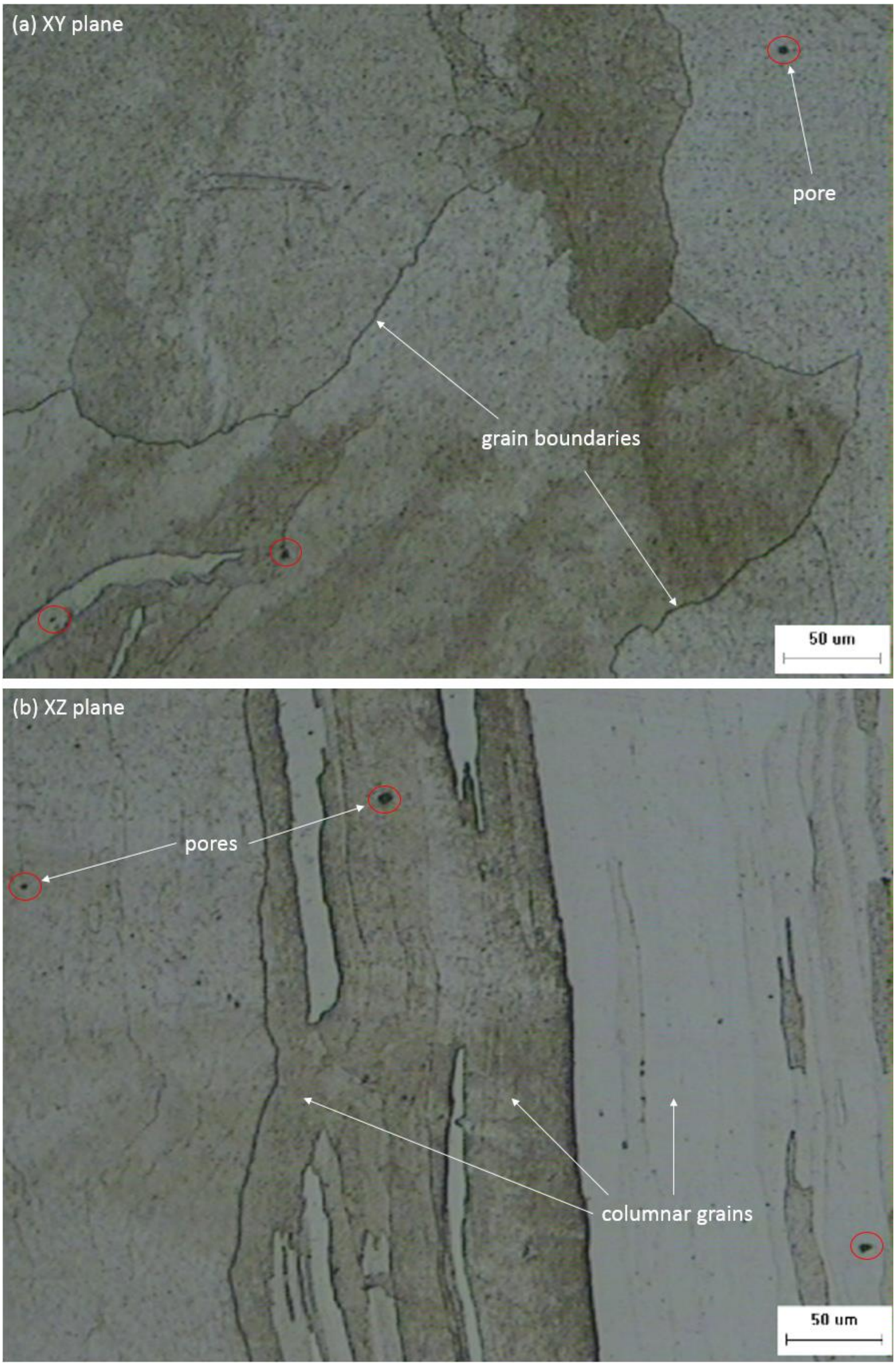
(a) XY plane
pore
grain boundaries
50 um
(b) XZ plane
pores
columnar grains
50 um

Figure 6.3 Optical microscopy images of SLM processed tin at a lower magnification, showing XY planes (a) and XZ planes (b), with pores circled in red.

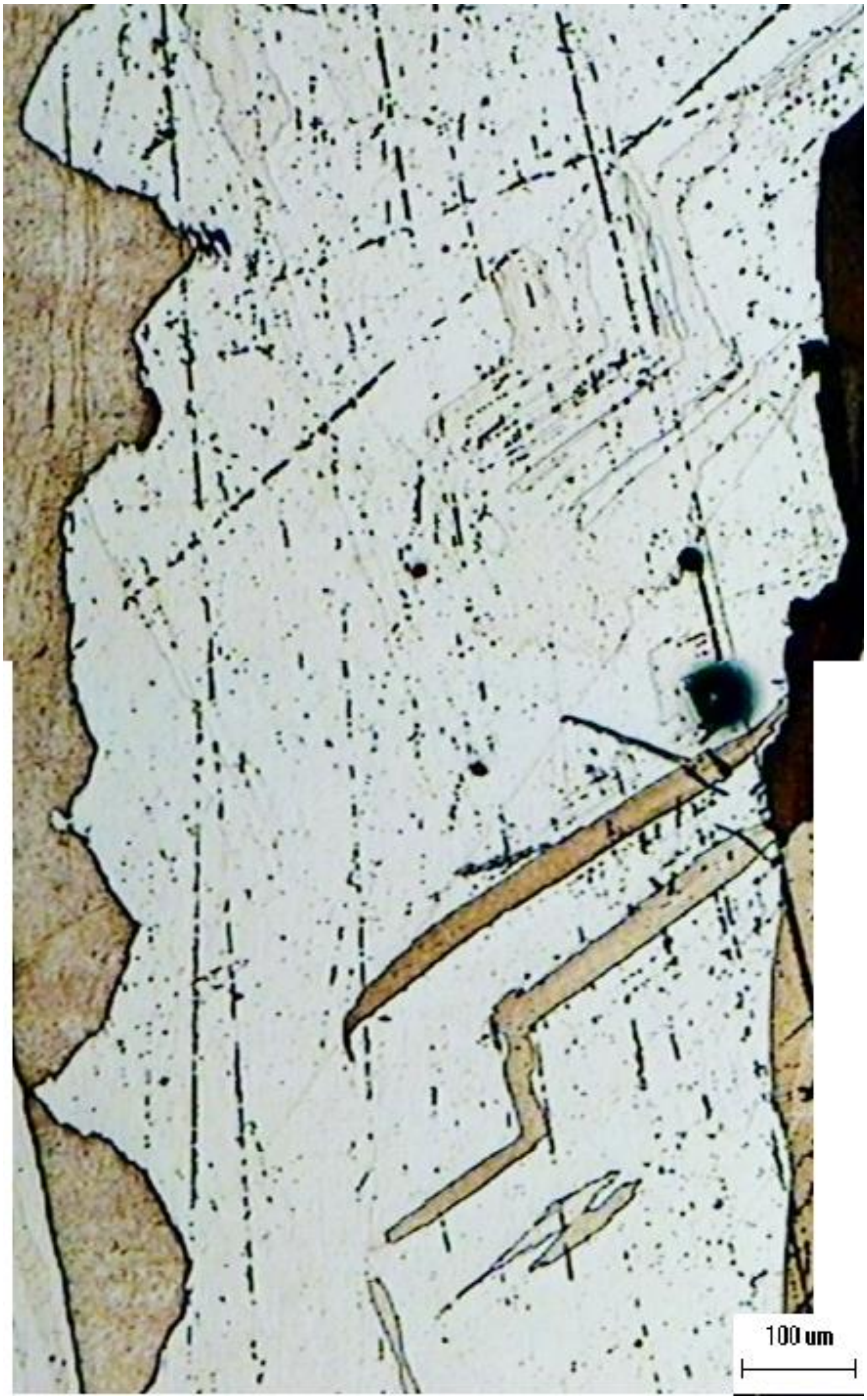

Figure 6.4 Optical microscopy: cross section (XZ plane) image of SLM processed tin near the edge, showing the zig-zag structure of the columnar crystal and twinned grains and recrystallized grains within original grain boundaries that result from working during polishing.

### 6.2.4 Scanning Electron Microscopy

SEM was carried out with the JOEL JSM 7600 FESEM microscope, operated at an acceleration voltage of 10 kV. Figure 6.5 shows the micrograph of the cross section (XZ plane) at a magnification of 500×. Pores between 2 to 5 µm in diameter are found. The images show a sharp contrast in the texture of the different grains in the vertical plane, due to the difference in crystal orientations.

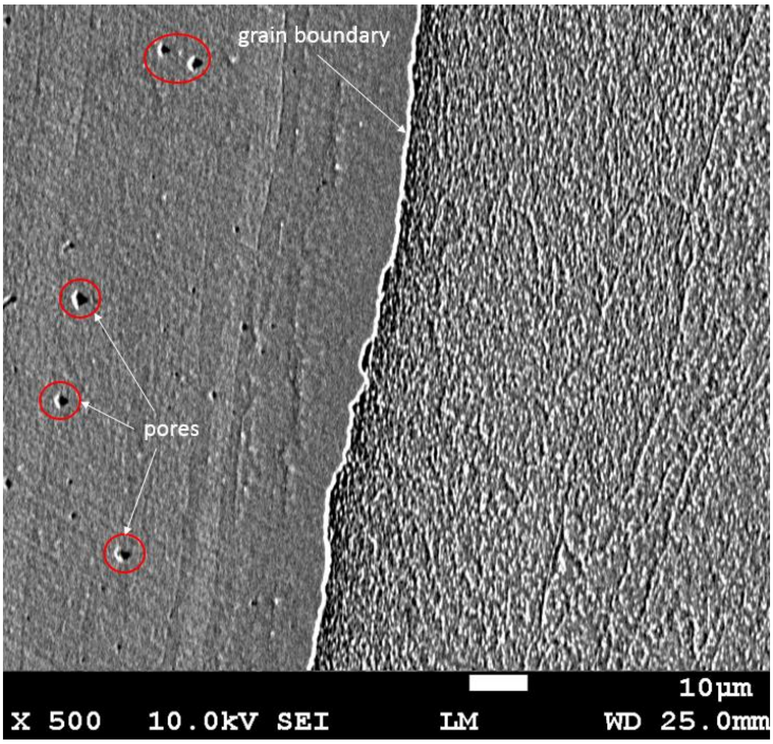

Figure 6.5 Scanning electron microscopy of a cross-section (XZ plane) SLM processed tin sample, showing the contrast in texture due to different crystal grain orientations.

### 6.2.5 Electron Backscatter Diffraction

Electron backscatter diffraction (EBSD) analysis was also carried out alongside with SEM to examine the local crystal orientation in the samples. In Figure 6.6, the high angle grain boundaries (HAGBs, misorientation > 15 °) are shown in black and low angle grain boundaries (LAGBs, misorientation < 15 °) in grey.

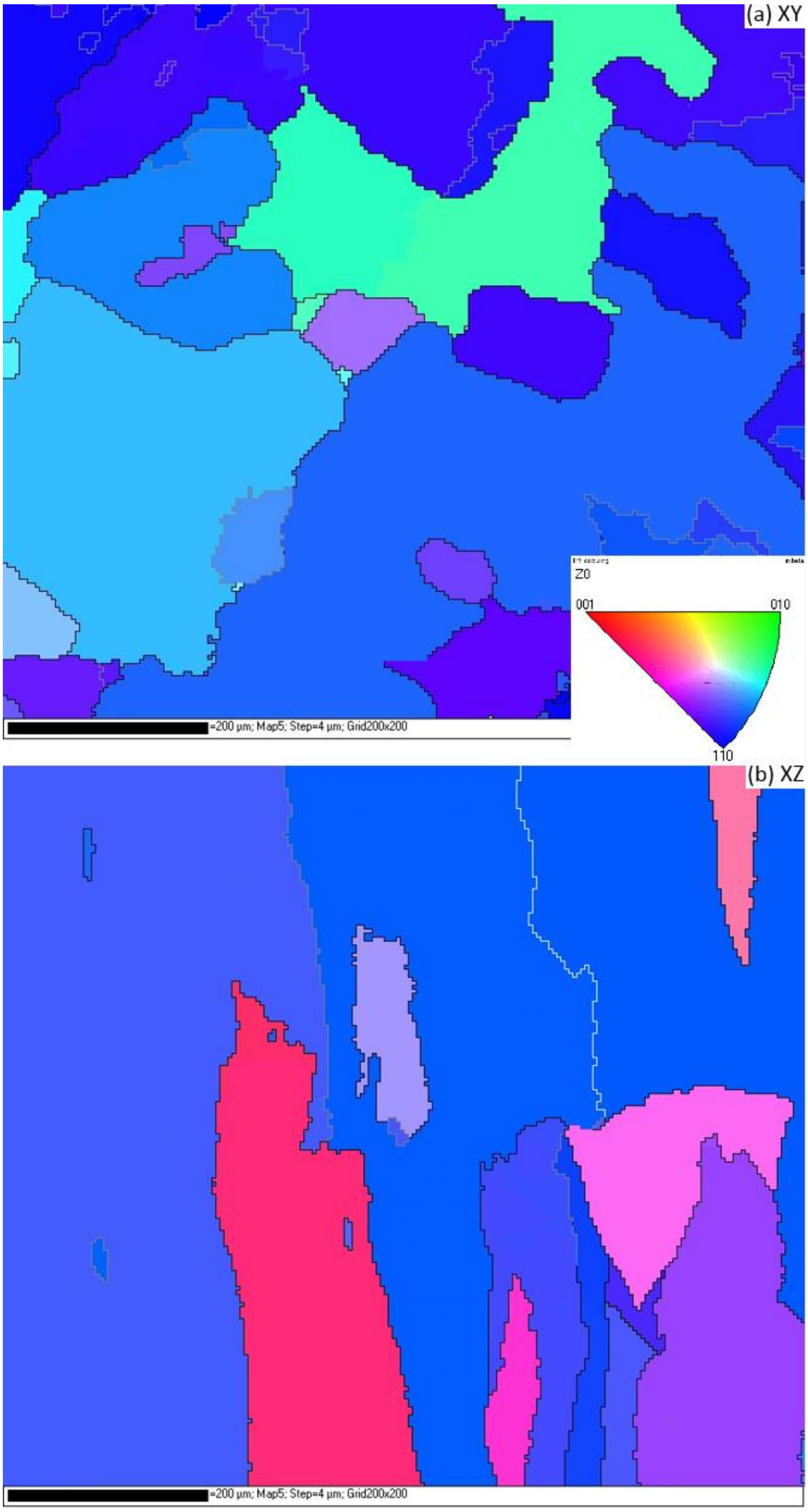
(a) XY
Z0
001
010
110
=200 µm; Map5; Step=4 µm; Grid200x200
(b) XZ
=200 µm; Map5; Step=4 µm; Grid200x200

Figure 6.6 EBSD analysis of SLM processed tin, displaying the different crystal orientations: <0 0 1> in red, <0 1 0> in green and <1 1 0> in blue.

EBSD analyses confirmed the columnar structures observed via LOM. Moreover, EBSD analyses have also shown that SLM processed tin has preferred grain orientation, which matches indications from the XRD analysis shown earlier. In both the XY plane and the XZ plane, most of the crystals were in the <1 1 0> orientation, as shown by a larger proportion of blue coloured grains in both maps.

## 6.3 Principle Outcomes

The study succeeded in fabricating 3D samples with pure tin powders via SLM. The densities of these samples were then examined for their densities through Archimedes' principle. Measurements of the samples' weights in the air and in water were taken with the Mettle Toledo XS204. The full density of bulk tin is 7.298 g/cm$^3$. The density is plotted against hatch spacing and the input VED (Figure 6.7).

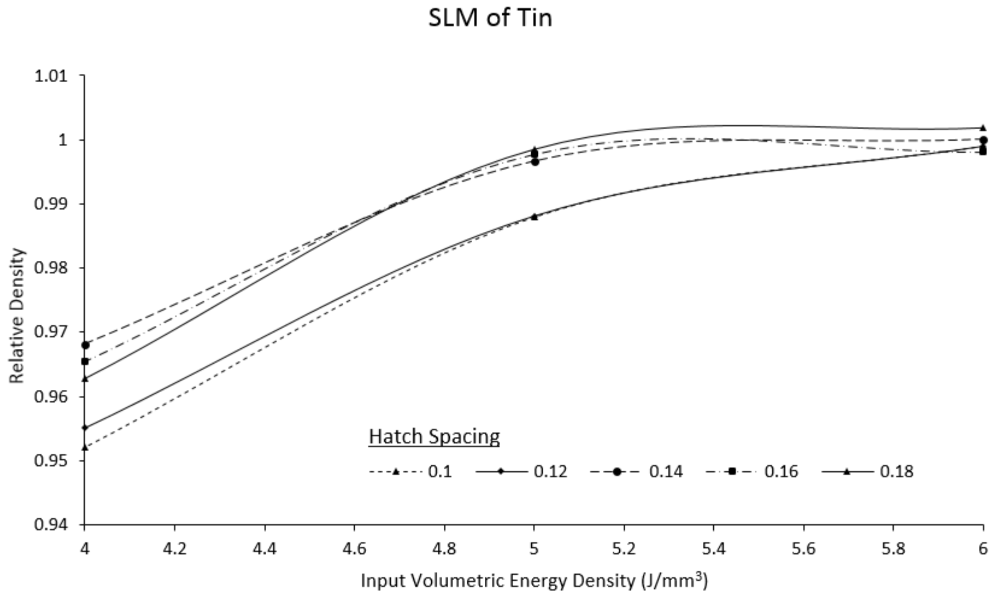

Figure 6.7 Relative density of SLM Tin samples plotted against input volumetric energy density at different hatch spacings.

Throughout the experiments, the laser scanning speed was maintained at 3,000 mm/s while the laser power was varied from 60 W to 162 W. Hatch spacing ranged from 0.10 mm to 0.18 mm. 5 samples were made for each combination of process parameters.

At VED of 4.0 J/mm$^3$, the mean relative density achieved was less than 97.0 %. The relative density improved significantly at VED of 5.0 J/mm$^3$ to an overall mean of 99.3 %. Moreover, at VED of 5.0 J/mm$^3$, hatch spacings of 0.10 mm and 0.12 mm gave a mean relative density of 98.8 % while hatch spacings from 0.14 mm to 0.18 mm produced a much better result, with a mean relative density of 99.7 %. A similar trend can be seen at VED of 4.0 J/mm$^3$. At 6.0 J/mm$^3$, near full density samples were achieved across all hatch spacing levels.

This study has shown that tin is a viable material for use with the SLM process and the process produced tin with columnar structures. Near full density samples were obtained and the crystal grains are anisotropic, with preferred grain orientations. Furthermore, given that the energy required for processing tin is low, this can pave the way for cost-effective AM of metals. Further research can be done to determine the cause of grain preference, mechanical properties of SLM processed tin and its applications. In addition, results from this work provide data for the semi-empirical modelling of the SLM process.

4

**References:**

[1] Komaba, S., et al., *Redox reaction of Sn-polyacrylate electrodes in aprotic Na cell.* Electrochemistry Communications, 2012. **21**: p. 65-68.

[2] Dai, K., et al., *Toward high specific capacity and high cycling stability of pure tin nanoparticles with conductive polymer binder for sodium ion batteries.* Journal of Power Sources, 2014. **263**: p. 276-279.

[3] Van der Schueren, B. and J.P. Kruth, *Powder deposition in selective metal powder sintering.* Rapid Prototyping Journal, 1995. **1**(3): p. 23-31.

[4] Kathuria, Y., *Metal rapid prototyping via a laser generating/selective sintering process.* Proceedings of the Institution of Mechanical Engineers, Part B: Journal of Engineering Manufacture, 2000. **214**(1): p. 1-8.

[5] Weiss, W. and D.L. Bourell. *Selective Laser Sintering to produce Ni-Sn intermetallics*. in *Solid Freeform Fabrication Symposium*. 1991. University of Texas at Austin.

[6] Walker, D.C., W.F. Caley, and M. Brochu, *Selective laser sintering of composite copper–tin powders.* Journal of Materials Research, 2014. **29**(17): p. 1997-2005.

[7] Scudino, S., et al., *Additive manufacturing of Cu–10Sn bronze.* Materials Letters, 2015. **156**: p. 202-204.

[8] Manriquez-Frayre, J.A. and D.L. Bourell. *Selective Laser Sintering of Binary Metallic Powder*. in *Solid Freeform Fabrication Symposium*. 1990. University of Texas at Austin.

[9] Yap, C.Y., et al., *Review of selective laser melting: Materials and applications.* Applied Physics Reviews, 2015. **2**(4): p. 041101.

[10] Agarwala, M., et al., *Direct selective laser sintering of metals.* Rapid Prototyping Journal, 1995. **1**(1): p. 26-36.

[11] Antonysamy, A.A., J. Meyer, and P.B. Prangnell, *Effect of build geometry on the β-grain structure and texture in additive manufacture of Ti6Al4V by selective electron beam melting.* Materials Characterization, 2013. **84**: p. 153-168.

# Chapter 7

# Discussion

*A semi-empirical model of the SLM process has been developed based on the theoretical energy requirement of the process and the process parameters that are required to achieve near full density components. It is observed that there exists a relationship between the energy requirement and the thermal conductivity of the material. This relationship has been elucidated with experimental data. The key results from the experiments elaborated in previous chapters are summarized. Plausible explanations for the results will also be discussed in this chapter, together with possible applications of the model and its limitations.*

*A reconnaissance study is also discussed in brief. This is a study on selective laser melting of high purity copper. It achieved a relative density of 82.8 % and the results indicate that a compensation factor higher than 2.5 was required if near full density parts were to be achieved at thermal conductivity of about 400 W/m·K.*

## 7.1 General Discussion

In Chapter 3, a semi-empirical model was developed to describe the relationship between the process parameters of the SLM process and the material properties. Discrepancies were found between the calculated energy requirements based on the model and the energy supplied in the SLM processes. Hence, a compensation factor, β, is added to the equation to account for the discrepancies:

$$\beta\left[v \cdot \frac{1}{2}\pi(t^2 + \frac{h^2}{4}) \cdot \frac{1}{2}\rho_{material} \cdot (\int c_s dT + L)\right] = \alpha_\lambda \cdot P \qquad (4)$$

Figure 3.3, a plot of compensation factor β against thermal conductivity, has shown that there is a huge gap in the information between thermal conductivity of 25 W/m·K and 150 W/m·K. Experiments were then carried out on AlSi10Mg, nickel and tin to obtain necessary data to fill in the gap. The approach can be illustrated by a simplified "Black Box" diagram as shown in Figure 7.1. In this black box approach, the process inputs include the SLM parameters (laser power, scanning speed, hatch spacing and layer thickness) and material properties (density, specific heat, latent heat, irradiation absorptance and thermal conductivity). The process outputs the density of the SLM samples and the calculated β based on (4).

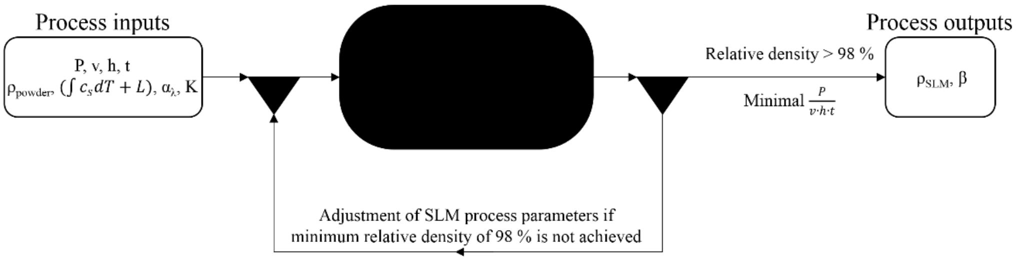
Process inputs
P, v, h, t
$\rho_{powder}$, $(\int c_s dT + L)$, $\alpha_\lambda$, K
Process outputs
Relative density > 98 %
Minimal $\frac{P}{v \cdot h \cdot t}$
$\rho_{SLM}$, β
Adjustment of SLM process parameters if minimum relative density of 98 % is not achieved

Figure 7.1 A "Black Box approach" summary of the semi-empirical modelling process.

Experiments detailed in Chapters 4, 5 and 6 have provided the parameters for an energy-efficient SLM process in achieving relative densities higher than 98.0 %. These parameters are summarized in Table 7.1. In addition, an updated plot of β vs thermal conductivity with data from current studies is shown in Figure 7.1. Data from the experiments on SLM of nickel and tin (Chapters 5 and 6) were added to the graph and information from the study on SLM of AlSi10Mg (Chapter 4) was used to replace earlier data.

Table 7.1 SLM process parameters with the lowest energy density required to achieve 98% relative density for AlSi10Mg, nickel, and tin.

| Material | Process parameters | | | | Relative Density (%) |
|---|---|---|---|---|---|
| | P (W) | v (mm/s) | h (mm) | t (mm) | |
| AlSi10Mg | 360 | 1200 | 0.20 | 0.05 | 98.9 |
| Nickel | 350 | 500 | 0.14 | 0.05 | 98.5 |
| Tin | 135 | 3000 | 0.18 | 0.05 | 98.5 |

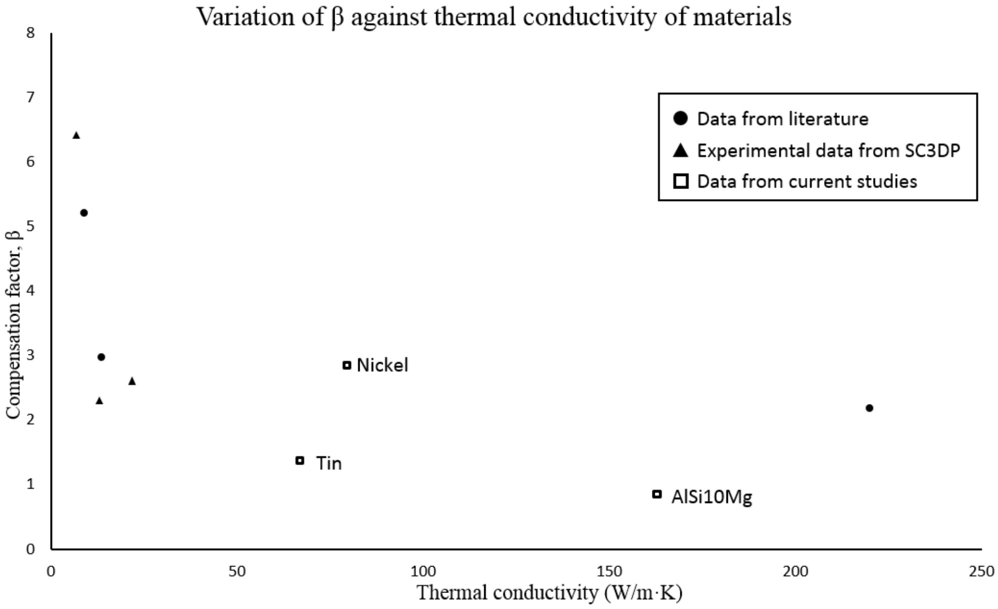

Figure 7.1 Updated plot of compensation factor against thermal conductivity with results from the experiments on tin, nickel and AlSi10Mg.

### 7.1.1 Compensation Factor β and Thermal Conductivity

β indicates the ratio of the energy requirement of the SLM process over the calculated value. A β value higher than 1 indicates that the calculated value underestimated the energy requirement and a β value lower than 1 suggests an over-estimation. In Figure 7.1, all but one of the data point give a β value between 1 and 10, showing that the model gives an underestimation of the energy requirement, albeit within the same order of magnitude. At thermal conductivity values up to 25 W/m·K, β decreases drastically from 6.4 (material: Ti6Al4V) to 2.6 (material: CP Ti). However, the drop becomes more gradual between 25 W/m·K and 163.2 W/m·K, except the data point corresponding to nickel. After that, the β value started to increase.

Such a trend between the β value and thermal conductivity shows how thermal conductivity of the material affects the SLM process. At very low thermal conductivity, heat energy generated by the exposure of laser on to a small pocket of metal powders is transferred at a much lower rate to the surrounding powders. Given the rapid heating and cooling that occurs during the process, only a small volume of powders is heated to the melting temperature. This results in a steep temperature gradient with a small melt pool, which means more energy input is required, or higher β value measured. Moreover, as parts of the melt pool can be much higher than that of the melting temperature and the presence of resultant surface tension gradient, severe Marangoni convection can occur. Strong Marangoni convection that flows radially inward would lead to high tendencies of “balling” [1, 2], a detrimental phenomenon where beads of metal are formed on the melt track and cause the SLM process to be disrupted [3].

At higher thermal conductivities, heat is transferred to surroundings at a much higher rate. However, the melt pool could also be small as much of the heat is lost to the surrounding and only a small volume of powders were able to reach the melting temperature. Hence, heat loss to the surroundings due to rapid heat transfer becomes much more significant at higher thermal conductivity values, which causes higher heat loss. These two competing factors may be a plausible explanation to the initial decrease in energy requirement as more powders are heated in the short time frame with increasing thermal conductivity and the subsequent increase as more heat is lost to the surrounding with better thermal conductivity.

However, the plot for nickel at thermal conductivity value of 80 W/m·K is significantly higher than the adjacent data points, for tin and AlSi10Mg. The need for more heat energy for the processing of nickel can be caused by its significantly higher melting temperature. Nickel has a melting temperature of 1724 K, compared to 505 K for tin and 925K for AlSi10Mg. As such, the heat loss during the SLM process is much higher for nickel, when compared to tin and AlSi10Mg, leading to a higher energy input.

### 7.1.2 Applications

An understanding of the effects of thermal conductivity to the energy requirement of the SLM process will enable researchers to predict the appropriate SLM process parameters for new materials. The model allows for the estimation of energy requirement once the material properties are known. Hence, parameter optimization studies can be shortened.

Currently, the alloys used for SLM such as AlSi10Mg, 316L stainless steel, Inconel 718 and Ti6Al4V, are materials already available in the market. Existing alloys that have good weldability have shown that they can also be processed by SLM. However, there is a need to develop novel alloys that are specifically optimized for such a laser-based AM process. AM material development has been identified as one of the key areas of for advancement of AM [4]. Knowing the relationship of various material properties, including thermal conductivity, will aid in the development of novel alloys for the laser based AM of metallic materials.

### 7.1.3 Limitations of the Model

The semi-empirical model developed in this study also has its limitations. Firstly, data from this model has used a relative density of 98.0 % as the benchmark. In many industrial applications, higher relative densities (99.5 %) are required. Moreover, material properties such as fatigue, toughness and ductility are extremely defect-sensitive. As shown by the results in Chapters 4, 5 and 6, the minimal energy requirement to attain 99.5 % relative density is plausibly higher. However, using 99.5 % as the benchmark presents its set of difficulties. The parameter optimization studies would take much more time and the data from existing literature would be limited.

Furthermore, the semi-empirical model is based on data from SLM of metals and alloys. Hence, such trends may not be applicable to ceramics, polymers or composite materials. Moreover, there is no information for materials with thermal conductivities higher than 220 W/m·K. Hence, the results of this study are applicable only to metallic materials with thermal conductivities between 6.8 W/m·K and 220 W/m·K.

## 7.2 Reconnaissance work not included in main chapters

A few other materials have also been tested with SLM. However, the results from these experiments were not reported in this thesis as near full density parts could not be achieved. Hence, these results could not contribute directly to the semi-empirical model. This section details one of such studies, which was the SLM processing of pure copper.

In this study, CU1332 powder, from Industrial Powder, consists of 99.85 % copper was used. CU1332 powders were spherical in shape. Sieve analysis showed 99.4% and 0.6% of the powder have the size of 325 Mesh (44 µm) and 200 Mesh (74 µm). The study was carried out in 2 stages. In order to prevent “balling”, single melt track experiment was first carried out to determine the combination of laser power and scanning speed that can produce continuous melt tracks for a powder bed with a thickness of 30 µm. In the horizontal axis, the laser scanning speed varies from 50 mm/s to 550 mm/s while in the vertical axis, the laser power varies from 120 W to 360 W (Figure 7.2).

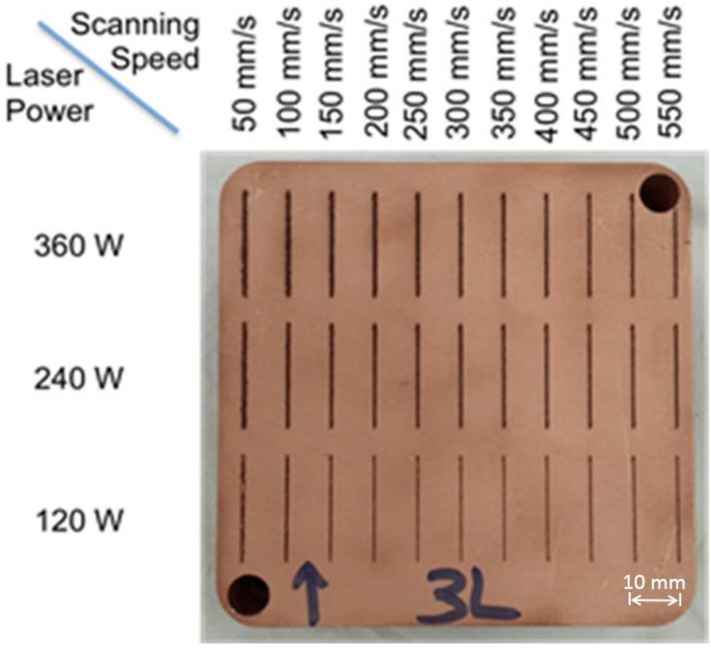
Scanning Speed
Laser Power
50 mm/s
100 mm/s
150 mm/s
200 mm/s
250 mm/s
300 mm/s
350 mm/s
400 mm/s
450 mm/s
500 mm/s
550 mm/s
360 W
240 W
120 W
3L
10 mm

Figure 7.2 Single melt track test for copper CU1332.

Under the optical microscope, the tracks with a laser power of 120 W could not be detected and those with a laser power of 240 W were barely observable. Only the single tracks created with a laser power of 360 W were clear and distinct. The single-track scan of the laser with a power of 360 W and scanning speed of 100 mm/s shows better continuity with less extent of “balling” behaviour compared to the melt track obtained at 50 mm/s. At scanning speeds beyond

150 mm/s, the melt tracks are discontinuous with gaps along the melt tracks as illustrated by the tracing shown in Figure 7.3.

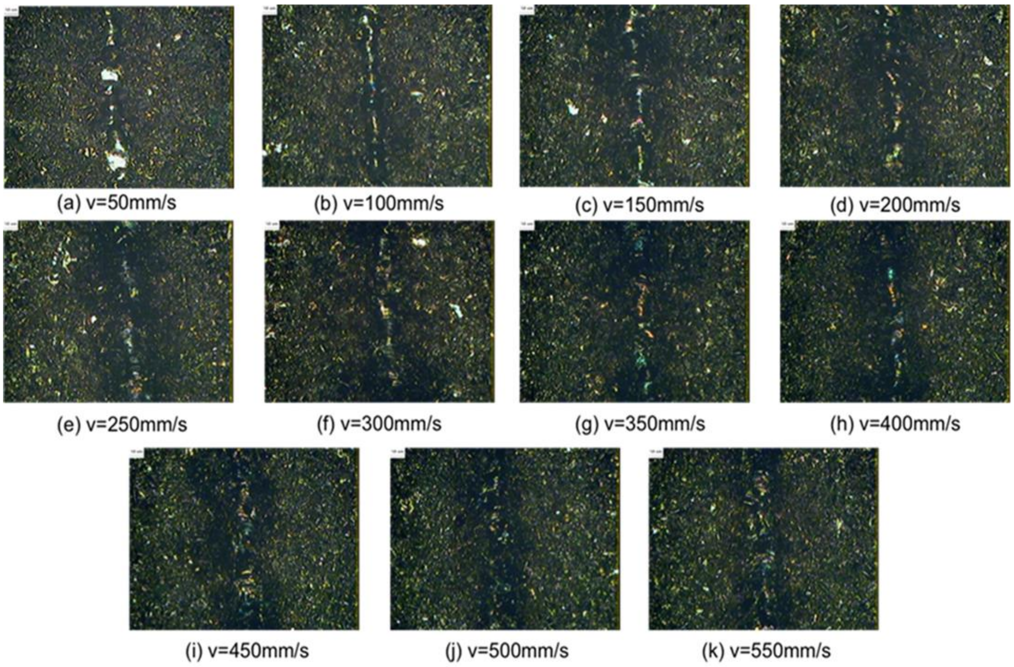
(a) v=50mm/s (b) v=100mm/s (c) v=150mm/s (d) v=200mm/s
(e) v=250mm/s (f) v=300mm/s (g) v=350mm/s (h) v=400mm/s
(i) v=450mm/s (j) v=500mm/s (k) v=550mm/s

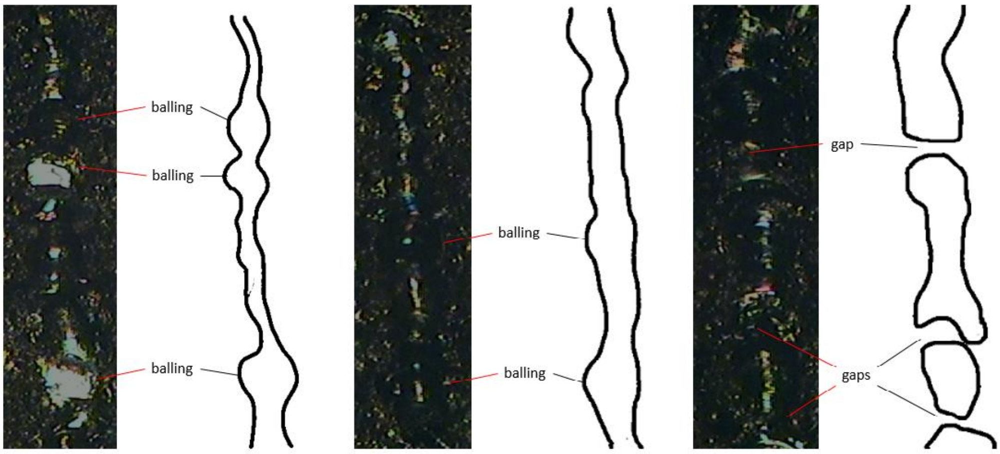

(a) v=50mm/s (b) v=100mm/s (c) v=150mm/s

Figure 7.3 Microscopy images of single melt tracks created at a laser power of 360 W, with enlarged images and tracing of the tracks at scanning speeds of 50 mm/s, 100mm/s and 150mm/s.

Based on the results from the first stage, the SLM 3D samples for the second stage were tested with a laser power of 360 W and a range of lower scanning speed, from 20 mm/s to 120 mm/s. In this experiment, the hatch spacing, $h$, is varied in the vertical axis, from 0.05 mm to 0.09 mm (Figure 7.4). For the first few layers, the CU1332 powders melted and bound well with the previous layer. “Balling” behaviour was minimal as expected. However as more layers were formed, “balling” behaviour became more severe and visible. As the results, the surface of the CU1332 parts was very rough. Fabrication of parts A1, A2, A3, and B1 was discontinued at an early stage because severe “balling” behaviour was observed. For the rest of the CU1332 parts, the surface was irregular and rough. The blocks were then removed from the substrate plate via electrical discharge machining and tested for their density. The highest relative density achieved was only 82.8 %, far below the 98 % required for the thesis. The results of the study are summarized in Table 7.2.

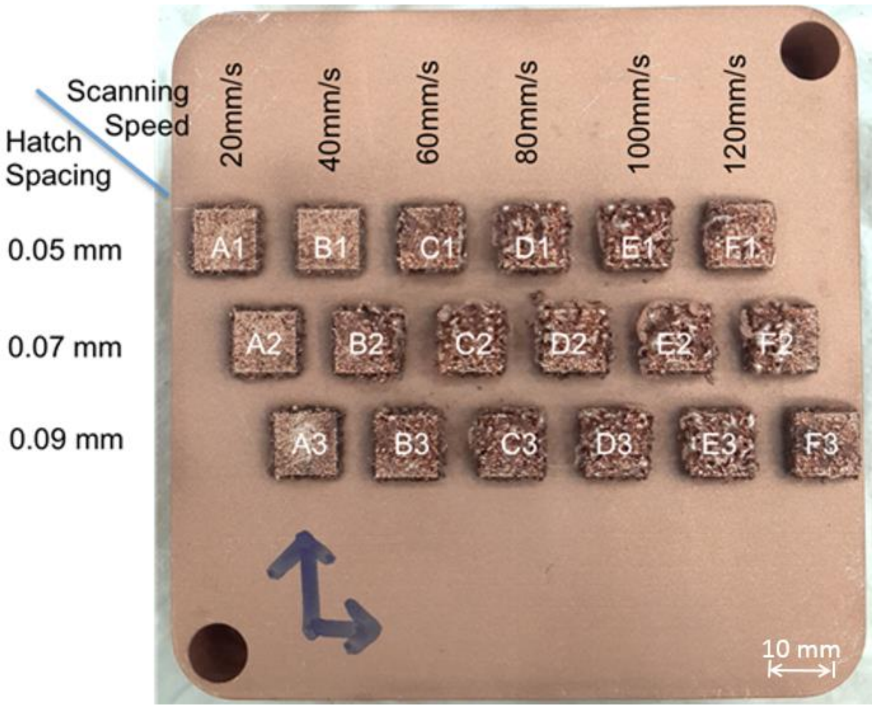
Scanning Speed
Hatch Spacing
20mm/s
40mm/s
60mm/s
80mm/s
100mm/s
120mm/s
0.05 mm
0.07 mm
0.09 mm
A1
B1
C1
D1
E1
F1
A2
B2
C2
D2
E2
F2
A3
B3
C3
D3
E3
F3
10 mm

Figure 7.4 Experiment on selective laser melting of copper powder CU1332.

Table 7.2 Relative densities of SLM of copper powder, CU1332.

| v (mm/s) | 20 | 40 | 60 | 80 | 100 | 120 |
|---|---|---|---|---|---|---|
| h (mm) | Relative Density (%) | | | | | |
| 0.05 | 80.2 | 78.9 | 75.9 | 74.9 | 75.6 | 76.2 |

| | | | | | | |
|---|---|---|---|---|---|---|
| 0.07 | 79.2 | 74.5 | 74.4 | 76.7 | 76.1 | 82.8 |
| 0.09 | 78.4 | 76.0 | 77.0 | 75.0 | 74.4 | 74.4 |

In this study, porous copper components with relative density up to 82.8 % were obtained. The study has also shown that SLM processing of high purity copper powder has to be carried out at high laser power values and low scanning speeds. At this combination, a higher laser energy density can be achieved and a good flow and binding of CU1332 particles can be attained. If the parameters for SLM of copper, that achieved 82.8 % relative density, were included in the semi-empirical model, it would expand the range up to 400 W/m·K and results would indicate that a compensation factor higher than 2.5 is required, as shown in Figure 7.5. However, such a porous component cannot be considered as near full density and hence the data from this experiment do not qualify for inclusion in the semi-empirical model.

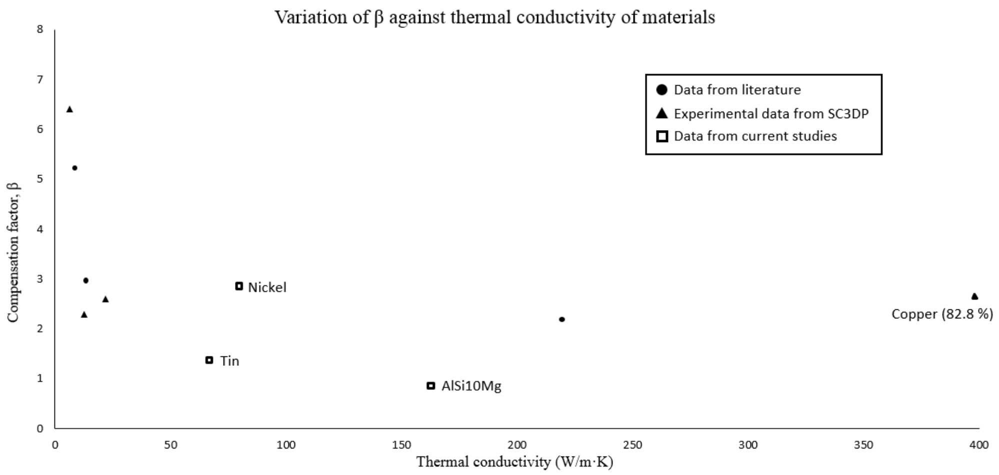

Figure 7.5 Plot of compensation factor against thermal conductivity with data from the experiments on copper powder CU1332.

**References:**

[1] Niu, H. and I. Chang, *Instability of scan tracks of selective laser sintering of high speed steel powder.* Scripta Materialia, 1999. **41**(11): p. 1229-1234.

[2] Gu, D., et al., *Densification behavior, microstructure evolution, and wear performance of selective laser melting processed commercially pure titanium.* Acta Materialia, 2012. **60**(9): p. 3849-3860.

[3] Yap, C.Y., et al., *Review of selective laser melting: Materials and applications.* Applied Physics Reviews, 2015. **2**(4): p. 041101.

[4] Wertz, P.K. *Penn State releases roadmap for advancement of additive manufacturing materials*. 2016 March 15, 2016 [cited 2016; Available from: http://news.psu.edu/story/397498/2016/03/15/research/penn-state-releases-roadmap-advancement-additive-manufacturing.

# Chapter 8

# Conclusion and Future Work

*This Ph.D. project has developed a semi-empirical model of the SLM process based on conservation of energy. Data for the development of the model was extracted from various scientific literature and experiments. It was found that the energy requirement of the SLM process varies with the thermal conductivity of the materials, in addition to the heat capacity and melting/liquidus temperature of the metals and alloys.*

*Through the course of this work, optimized process parameters were also developed for pure nickel and pure tin, which had not been successfully processed with SLM prior. Near full density samples were achieved for these metals and their microstructures have also been examined.*

*There are several suggestions for future work. Improvements to the model can be made with the inclusion of more conductive materials such as silver, brass and other alloys. The benchmark for relative density can also be shifted to 99.5 % when closed loop process control for SLM is available for improved consistency of these AM machines and numerical simulations can be used to elucidate effects of thermal conductivity to the SLM process.*

## 8.1 Findings and Conclusion

In accordance with the objectives mentioned in Chapter 1, a semi-empirical model of the SLM process has been developed. The relationship between the energy requirement of the process and the thermal conductivity of the material has been elucidated both with experimental data and information from the related literature. The novel model allows for good estimation of the energy requirements of the SLM process for new materials. In addition, SLM process parameters for nickel and tin were also established through this work and the resultant microstructures of these materials were examined. There had been no prior success in the SLM processing of nickel and tin. The main findings of the thesis are summarized, as follows:

(1) A model for the SLM process, which includes the profile of the melt pool, material-dependent heat capacity, laser-material coupling, and SLM process parameters, has been developed. The semi-empirical relationship between the energy requirement of the process and the thermal conductivity of the material has been elucidated by data from literature and experiments on AlSi10Mg, nickel, and tin. Discussions have been made on the development of the model, the methodologies adopted for the experiments and the principles of various techniques for the study of microstructures.

(2) Experiments have been carried out on the SLM of an aluminium alloy, AlSi10Mg. This material has been reported in a number of scientific articles. However, they provide different processing parameters. This study was conducted to explore the process envelope and determine the combination of parameters that produces near-full density samples with the lowest energy requirement. This study shows the typical microstructures of the SLM processed alloys and also establishes how parametric studies can be analysed for further experiments.

(3) Studies were conducted on the SLM processing of nickel and tin. To the best of the author's knowledge, these two materials had not been successfully fabricated with SLM prior. Experimental results showed that near-full density were obtained for both nickel (99.0 %) and tin (99.9 %). Their microstructures were also examined and characterized.

The limitations of the proposed semi-empirical model have also been discussed in Chapter 7. As the data used is based on metallic materials, the model may not be applicable to ceramics and polymers. Moreover, the thesis only provides data from thermal conductivity values from 6.8 W/m·K to 220 W/m·K.

## 8.2 Recommendations for Future Work

Based on the limitations of the model and the analyses in the previous chapters, a few recommendations for future studies are suggested, as follows:

(1) Currently, there are only 9 data points in the graph with an outlier in the data from the experiment on nickel. Moreover, the data points beyond the thermal conductivity of 25 W/m·K are spread far apart. For the semi-empirical model to be better established, more information is required to fill in these gaps, especially for thermal conductivity values from 100 W/m·K to 150 W/m·K. This would require SLM process optimization experiments on other conductive metallic materials such as brass (110 – 130 W/m·K), molybdenum (142 W/m·K), aluminium (247 W/m·K), gold (318 W/m·K), silver (428 W/m·K), and other alloys. Additional data point would also allow the optimal range of thermal conductivities to be identified. This knowledge will be useful in the development of new materials for laser-based AM systems.

(2) The current model is based on a relative density of 98.0 %. Although this benchmark is acceptable for most industries and comparable to that

achieved via the casting process, minimizing porosity continues to be a pursuit in the manufacturing of metallic components. Properties such as ductility, fracture toughness, and fatigue life are defect-sensitive and reduced porosity can significantly improve the functionality and lifespan of the AM component. In SLM, relative densities of 99.5 % and above has been reported for materials such as Marage 300 steel [1], H20 tool steel [2], 316L stainless steel [3], Ti6Al4V [4] and AlSi10Mg [5]. However, such results are difficult to emulate and repeat as SLM is a dynamic process and current SLM systems lack closed-loop process controls for better consistency and reliability [6]. With improved SLM systems, experiments can be conducted for a higher benchmark such as 99.5 %. In this case, a general upward shift of the plots is expected on the graph, as more energy is required to achieve a higher relative density.

(3) Numerical simulation can be done to elucidate the mechanism which links the heat energy requirement of the SLM process and the thermal conductivity. The study can be conducted by examining the size of the melt pool at various thermal conductivity values of material. The laser power and scanning speed chosen should correspond to the optimized process parameter of the said material. As the thermal conductivity varies, the cross section area of the melt pool is expected to change. Simulations can be done with software such as ANSYS or COMSOL.

(4) In the future, tests can be done for SLM processed nickel and tin so that the tensile strength, compressive strength, fatigue properties and other mechanical properties can be determined. In addition, magnetostrictive properties of SLM processed nickel should also be tested for potential applications in complex geometry transducers. With these tests, the relationship between the SLM manufacturing process, resultant microstructure and properties can be determined for these metals.

**References:**

[1] Casavola, C., S.L. Campanelli, and C. Pappalettere, *Preliminary investigation on distribution of residual stress generated by the selective laser melting process*. The Journal of Strain Analysis for Engineering Design, 2009. **44**(1): p. 93-104.

[2] Milovanovic, J., M. Stojkovic, and M. Trajanovic, *Rapid tooling of tyre tread ring mould using direct metal laser sintering*. Journal of Scientific & Industrial Research, 2009. **68**(12): p. 1038-1042.

[3] Yasa, E., J. Deckers, and J.-P. Kruth, *The investigation of the influence of laser re-melting on density, surface quality and microstructure of selective laser melting parts*. Rapid Prototyping Journal, 2011. **17**(5): p. 312-327.

[4] Vandenbroucke, B. and J.P. Kruth, *Selective laser melting of biocompatible metals for rapid manufacturing of medical parts*. Rapid Prototyping Journal, 2007. **13**(4): p. 196-203.

[5] Buchbinder, D., et al., *High Power Selective Laser Melting (HP SLM) of Aluminum Parts*. Physics Procedia, 2011. **12**: p. 271-278.

[6] Frazier, W.E. *Direct digital manufacturing of metallic components: vision and roadmap*. in *21st Annual International Solid Freeform Fabrication Symposium*. 2010.

# List of Publications

Throughout the course of research, several papers were published, as follows:

Journal Papers:

(1) C. Y. Yap, Chua, C. K., Dong, Z. L., Liu, Z. H., Zhang, D. Q., Loh, L. E., & Sing, S. L. Review of selective laser melting: Materials and applications. Applied Physics Reviews, 2015. 2(4): p. 041101

(2) C.Y. Yap, C.K. Chua, and Z.L. Dong, An effective analytical model of selective laser melting. Virtual and Physical Prototyping, 2016: p. 1-6.

(3) C.Y. Yap, H.Y.K. Tan, Z.L. Du, C.K. Chua, and Z.L. Dong, Selective Laser Melting of Nickel Powder, Rapid Prototyping Journal (accepted)

Conference Papers:

(1) C. Y. Yap, C. K. Chua, Z. Dong, Z. H. Liu & D. Q. Zhang Single track and single layer melting of silica by Selective Laser Melting. in High Value Manufacturing: Advanced Research in Virtual and Rapid Prototyping: Proceedings of the 6th International Conference on Advanced Research in Virtual and Rapid Prototyping, Leiria, Portugal, 1-5 October, 2013. 2013. CRC Press.

(2) W. Y. Yeong, C. Y. Yap, M. Mapar, C. K. Chua. State-of-the-art review on selective laser melting of ceramics. in High Value Manufacturing: Advanced Research in Virtual and Rapid Prototyping: Proceedings of the 6th International Conference on Advanced Research in Virtual and Rapid Prototyping, Leiria, Portugal, 1-5 October, 2013. 2013. CRC Press.

(3) C. Y. Yap, C. K. Chua, Z. Dong, Z. H. Liu & D. Q. Zhang State-of-the-Art Review on Selective Laser Melting of Non-Ferrous Metals. in 1st International Conference on Progress in Additive Manufacturing. 26-28 May 2014. Singapore. Research Publishing.

(4) C. Y. Yap, C. K. Chua, & Z. Dong Preliminary investigation on selective laser melting of pure tin. in 2nd Conference on Progress in Additive Manufacturing. 16-19 May 2016. Singapore. Research Publishing.

(5) C. Y. Yap, C. K. Chua, & Z. Dong Selective laser melting of pure tin: microstructure study. in Solid Freeform Fabrication Symposium. 8-11 August 2016. Austin, Texas, United States of America.